University of Alberta

Electron Energy-Loss Spectroscopy of Nanostructures

by

Feng Wang

©

A thesis submitted to the Faculty of Graduate Studies and Research
in partial fulfillment of the requirements for the degree of

Doctor of Philosophy

Department of Physics

Edmonton, Alberta

Spring, 2007

Library and Archives Canada

Published Heritage Branch

395 Wellington Street
Ottawa ON K1A 0N4
Canada

Bibliothèque et Archives Canada

Direction du Patrimoine de l'édition

395, rue Wellington
Ottawa ON K1A 0N4
Canada

Your file Votre référence
ISBN: 978-0-494-29763-6
Our file Notre référence
ISBN: 978-0-494-29763-6

NOTICE:
The author has granted a non-exclusive license allowing Library and Archives Canada to reproduce, publish, archive, preserve, conserve, communicate to the public by telecommunication or on the Internet, loan, distribute and sell theses worldwide, for commercial or non-commercial purposes, in microform, paper, electronic and/or any other formats.

The author retains copyright ownership and moral rights in this thesis. Neither the thesis nor substantial extracts from it may be printed or otherwise reproduced without the author's permission.

AVIS:
L'auteur a accordé une licence non exclusive permettant à la Bibliothèque et Archives Canada de reproduire, publier, archiver, sauvegarder, conserver, transmettre au public par télécommunication ou par l'Internet, prêter, distribuer et vendre des thèses partout dans le monde, à des fins commerciales ou autres, sur support microforme, papier, électronique et/ou autres formats.

L'auteur conserve la propriété du droit d'auteur et des droits moraux qui protège cette thèse. Ni la thèse ni des extraits substantiels de celle-ci ne doivent être imprimés ou autrement reproduits sans son autorisation.

In compliance with the Canadian Privacy Act some supporting forms may have been removed from this thesis.

While these forms may be included in the document page count, their removal does not represent any loss of content from the thesis.

Conformément à la loi canadienne sur la protection de la vie privée, quelques formulaires secondaires ont été enlevés de cette thèse.

Bien que ces formulaires aient inclus dans la pagination, il n'y aura aucun contenu manquant.

Canada

Abstract

In studies of nanostructural materials, electron energy-loss spectroscopy (EELS) shows its specific advantage of high spatial resolution in chemical analysis, by a spectrometer in a transmission electron microscope (TEM). Energy loss near-edge structure (ELNES) in ionization edges can provide information on the local valence (or bonding) state and coordination of the excited atom. In this study, the spectral features of ELNES were interpreted using a real-space multiple scattering (RSMS) approach. The appearance of a "postpeak" (a broad post-edge peak above L-edge) or prepeak is shown to be a characteristic of transition metals in an oxidized state, by the experiments and RSMS calculations. These peaks provide a convenient and sensitive test in checking interfacial oxidation of metallic nanoparticles embedded in a matrix.

Novel processes were developed in nanofabrication, including *in-situ* fabrication of iron nanoparticles by electron-induced decomposition of iron fluorides, fabrication of stable iron nanoparticles embedded in a silica matrix through multilayer route, and synthesis of regular arrays of silicon oxide nanowires from a patterned reagent. ELNES methods developed here were used to monitor the evolution of the phase state of iron during electron beam irradiation of iron fluorides in a TEM, check the oxidation state of iron nanoparticles embedded in a silica matrix and encapsulated at the end of nanowires. The results provide an explanation of the magnetic properties of the iron nanoparticles that were characterized using Lorentz microscopy, the magneto-optical Kerr effect and a physical-properties measurement system. The growth mechanism of silicon oxide nanowires is also discussed in relation to the microstructural and electronic analysis in TEM.

Dedicated to my wife, Keju and daughter, Kelly

Acknowledgements

First and foremost, I would like to thank my supervisors, Prof. Ray Egerton and Dr. Marek Malac, for mentoring me all the way in the EELS field, and hand-on-hand instruction on experimental setup and advanced TEM techniques. And also I hope thank my cosupervisors, Profs. Mark Freeman and Zhenghe Xu for advices on Physics and Chemical engineering, leading me into the nanoscience research. The completeness of this thesis research should be firstly attributed to their patience, encouragement and support throughout my graduate studies.

I am grateful to Prof. Al Meldrum for his stimulating discussions and his kindness in offering his labs; to Dr. Yimei Zhu for inviting me to Brookhaven National Laboratory and Dr. Marvin Schofield for help with TEM setup in BNL; to Prof. Jonathan Veinot for his insight comments on my work in chemistry side; to Dr. Sergio Moreno for discussions on EELS calculations.

Great thanks belong to the technical support from Don Mullin, Greg Popowich, Tony Walford, Daniel Salamon and their friendliness; Greg's hand-on-hand help with TEM and vacuum systems is highly appreciated.

I hope to thank Dr. Xiaobin Zhu and Zhigang Liu for help with MOKE setup, Nicole Macdonald, Cindy Blois for help with X-section TEM samples.

Thanks should be addressed to group members Peng Li, Hui Qian and Robert McLeod, for their help and discussions, and especially to Peng Li for his EBL work.

I am obliged to Lynn Chandler, Sarah Derr, Profs. Richard Sydora, Jan Jung, Richard Marchand for setting up my research program, and their administrative help.

I am deeply indebted to my parents for their love and all-the-way support. I also want to thank my parents-in-law for looking after our daughter. I would say, to our lovely daughter Kelly, your birth brought luck and fun to the family, and you grew up with this thesis research.

Last, but not least my special thanks go to my beloved wife Keju Bao, for her support, understanding, for everything.

Table of contents

Chapter 1 Introduction and background **1**
1.1 Introduction 1
1.2 Experimental techniques 4
1. 2.1 Electron energy-loss spectroscopy 4
1.2.1a Magnetic prism 4
1.2.1b Two TEM modes 5
1.2.1c Energy resolution of EELS 6
1.2.1 d Comparison of EELS with other techniques in studies of nanostructures 7
1.2.2 Ultra high vacuum (UHV) 8
1.3 Basic theory of ELNES 10
1.3.1 ELNES: a site-specified and symmetry-projected DOS 11
1.3.2 Dipole approximation 14
1.3.2a Dipole approximation 14
1.3.2b Non-dipole transition 15
1.3.3 Limitations in energy and spatial resolution 15
1.3.3a Energy broadening 15
1.3.3b Delocalization of inelastic scattering 18
1.3.4 Orientation dependence 19
1.3.5 *ab initio* calculations 20
1.3.5a Real-space multiple scattering calculation 20
1.3.5b FEFF program 21
1.3.5c Prepeak and postpeak in iron nanoparticles 22
1.3.6 3d occupancy and white lines of iron 23
1.4 Outline of the thesis 23
References 26
Chapter 2 Energy-loss near-edge fine structures of iron nanoparticles **29**
2.1 Introduction 29
2.2. Experiment 30

2.3 Results and discussion 32
2.3.1 Decomposition of FeF_2 32
2.3.2 White lines 35
2.3.3 Origin of the postpeak 38
2.3.4 Collective behaviour 41
2.4 Conclusions 42
References 43
Chapter 3 Interpretation of the postpeak in iron fluorides and oxides 46
3.1 Introduction 46
3.2 Experimental Methods 47
3.3 Results 50
3.4 Discussion 56
3.5 Conclusions 59
References 60
Chapter 4 Multilayer route to iron nanoparticle formation in an insulating matrix 62
4.1 Introduction 62
4.2 Experiment 63
4.3 Results and discussion 66
4.3.1 Microstructure and oxidation analysis 66
4.3.2 Magnetic properties 71
4.3.3 Morphology and air resistance of iron nanoparticles 74
References 78
Chapter 5 Alternative methods of identifying the oxidation of metallic nanoparticles embedded in a matrix 81
5.1 Introduction 81
5.2 Experimental methods 82
5.3 Results 84
5.3.1 Imaging 84
5.3.2 White line ratio 85
5.3.3 Prepeak 86
5.3.4 Postpeak 89

5.4 Discussion 90
References 92
Chapter 6 Controlled growth of silicon oxide nanowires from a patterned reagent 95
References 101
Chapter 7 An ELNES study of silicon oxide nanowires grown from a patterned reagent 104
7.1 Introduction 104
7.2 Experiments 105
7.3 Results and discussion 106
References 111
Chapter 8 General discussion and conclusion 113
References 116
Appendix A Procedures for *in-situ* annealing in UHV system 118
Appendix B Growth process of iron nanoparticles in a silica matrix: a real time study by in-situ transmission electron microscopy 119
B.1 Introduction 119
B.2 Experiments 120
B.3 Results 122
References 127
Appendix C Local oxidation of single iron nanoparticles in a SiO_2 matrix 128
C.1 STEM-EELS of a single iron nanoparticle 128
C.2 HRTEM of a single iron nanoparticle 129
Appendix D Magnetite nanoparticles 131
D.1 Experiments: 131
D.2 Results 132
D.3 Remarks and conclusion 133
References 134
Appendix E Exclusion of plural scattering 135
Appendix F Terminology 137

List of tables

Chapter 1

Table 1-1 a comparison of EELS with other spectroscopic techniques, in the probe, the spatial and energy resolutions, and the sample requirement.

Chapter 3

Table 3-1 Radii and occupancy of the first five shells around an iron atom in α-Fe, FeF_2 and α-Fe_2O_3.

Chapter 4

Table 4-1 Composition, particle diameter, coercivity and saturation of the samples.

Appendix

Table A-1 Temperature vs current (rough data from annealing experiments)

Table D-1 Synthesis temperature, particle size and magnetization for four different magnetite samples.

List of figures

Chapter 1

Figure 1-1 The dispersion and focusing of electrons in a magnetic prism, (a) in the bend plane of spectrometer and (b) in a plane normal to the bend plane.

Figure1-2 Simplified optics for two TEM modes in recording EELS: imaging and diffraction modes.

Figure 1-3 Photo of the UHV system used for sample preparation in this thesis work.

Figure 1-4 Schematic view of the UHV pumping system.

Figure 1-5 Geometry of an inelastic scattering process.

Figure 1-6 Core-level widths of K and L edges versus threshold energy.

Figure 1-7 Comparison of the final-state lifetime broadening for Al-L edge, obtained from experiments and calculations.

Figure 1-8 Schematic illustration for the multiple scattering of the outgoing wave reflected off from the surrounding atoms.

Figure 1-9 A sequential cluster calculation for F-K of FeF_2.

Figure1-10 Schematic diagram of the atomic energy levels and the level occupancies for the metallic iron.

Chapter 2

Figure 2-1 Illustration of the experimental setup for deposition of FeF_2 film.

Figure 2-2 (a) BF image with SAD pattern of FeF_2 before irradiation and corresponding profile of the SAD pattern; (b) BF image with SAD pattern of FeF_2 after irradiation and corresponding profile of the SAD pattern.

Figure 2-3 BF images and corresponding SAD patterns for iron nanoparticles of different sizes.

Figure 2-4 (a) Typical O K-, F K- and Fe L23- edges recorded at the start of electron exposure, and after a dose of 400 C/cm^2 and 4500 C/cm^2 at site (d); (b) Dose dependence of the F K-edge and Fe L-edges.

Figure 2-5 (a) Typical curve-fitting result; (b) Dependence of the white line ratio on the electron dose and on the size of the iron nanoparticles.

Figure 2-6 Experimental results for oxidization of iron films.

Figure 2-7 Bright-field image and Lorentz images in underfocus, focus and overfocus modes for the nanoparticles shown in Figure 2-3 (a).

Chapter 3

Figure 3-1 Unit cells for α-Fe, FeF_2 and α-Fe_2O_3 reproduced from Crystal Kit software.

Figure 3-2 Dose dependence of the Fe L_{23} and F K-edges.

Figure 3-3 Experimental ELNES of iron and iron oxides.

Figure 3-4 Multiple-scattering calculation of the cross-sections for Fe L edges of (a) α-Fe, (b) FeF_2 and (c) α-Fe_2O_3.

Figure 3-5 Calculated results of the L_3 cross-sections of (a) α-Fe, (b) FeF_2 and (c) α-Fe_2O_3 for scattering clusters of different sizes.

Figure 3-6 Calculated results of the backscattering amplitudes F_{eff} for iron, fluorine and oxygen in α-Fe, FeF_2 and α-Fe_2O_3.

Figure 3-7 Calculated results of the Co L_3 cross-sections of Co, CoF_2 and CoO for cluster sizes of 81, 83 and 81 atoms respectively.

Chapter 4

Figure 4-1 Plan-view TEM images and SAED patterns of iron nanoparticles embedded in a silicon dioxide matrix.

Figure 4-2 Size distribution of iron nanoparticles.

Figure 4-3 Energy-loss near-edge structure of Fe L_{23} edges of iron nanoparticles.

Figure 4-4 Dependence of (a) white-line ratio and (b) oxidation-layer thickness on the diameter of iron nanoparticles.

Figure 4-5 Normalized magnetization hysteresis measured by MOKE for iron nanoparticles in different samples.

Figure 4-6 Dependence of the coercivity H_c on particle size (a) and volume-filling factor (b).

Figure 4-7 (a) Cross-sectional bright-field image for Fe 15 after annealing. (b) Plan-view TEM image for as-grown Fe15 sample.

Figure 4-8 (a) Comparison of the white lines of Fe15 as initially fabricated and after exposure to air for three months. (b) In-plane magnetization of samples Fe07, Fe10, Fe15 and Fe150, after 14-month storage in laboratory air.

Chapter 5

Figure 5-1(a) Bright-field TEM image of iron nanoparticles embedded in a silica matrix; (b) High-angle annular dark field (HAADF) image ofa single iron nanoparticle.

Figure 5-2 A variation of the white line ratio (WLR) as a function of particle diameter. Measurement errors in the particle diameter and WLR are also shown.

Figure 5-3 (a) Calculations of the O K-edges for SiO_2 (of 62-atom cluster), Fe_2O_3 (of 5- and 116-atom clusters) and FeO (of 7- and 81- atom clusters), and (b) Experimental oxygen K-edges for the six Fe-SiO_2 nanocomposite films

Figure 5-4 (a) Calculated iron L_{23} edges for Fe, FeO and Fe_2O_3, for cluster sizes of 65, 57 and 75 atoms respectively. The postpeak positions are marked by arrows. (b) Experimental iron L-edges for the six Fe-SiO_2 nanocomposite films

Figure 5-5 L_{23} edges of transition metal oxides, reproduced from EELS Atlas.

Chapter 6

Figure 6-1 Bright-field TEM images for (a) arrays of iron nanoparticles after lithographic patterning, of 50 nm diameter and 1 um spacing, and (b) arrays of nanowires grown from the patterned nanodots.

Figure 6-2 Bright-field TEM image of a bundle of individual nanowires projecting from the substrate.

Figure 6-3 Dependence of the diameter of the nanowires on that of the encapsulated Fe particles.

Figure 6-4 Proposed growth process of nanowires.

Chapter 7

Figure 7-1 (a) Bright-field TEM image for individual NWs protruding from substrate and (b) experimental Si L_{23} edges for silicon oxide NWs with substrate and away from substrate, compared with a Si L_{23} edge calculated for SiO_2 (α-quartz).

Figure 7-2 (a) A comparison of oxygen K-edge near-edge structure of NWs, silica and α-quartz; (b) RSMS calculation on the O-K edge of α-quartz, on the clusters of increasing size.

Figure 7-3 Experimental Fe-L_{23} edges and a computer fit of selected individual nanowires.

Figure 7-4 Core-shell structures at the tips of the NWs.

Chapter 8

Figure 8-1 Analytical compatibilities in a TEM (equipped with a field emission gun).

Appendix

Figure B-1 Morphology and phase identification of iron nanoparticle before and after annealing.

Figure B-2 Bright field TEM images taken during annealing by smart control.

Figure B-3 Bright field TEM images for the iron nanoparticles taken at a rotaton of 0° and 30°.

Figure B-4 (a) Hologram and (b) 16x phase amplified contour map of magnetic field for a single nanoparticle obtained in the annealing by smart control.

Figure C-1 STEM-EELS results on a single iron nanoparticle of 10 nm in diameter. (a) ELNES of Fe-L_{23} on the edge and center of the particle. (b) HAADF image of a collection of iron nanoparticle particles.

Figure C-2 (a) Crystal lattice of a single iron nanoparticle and (b) HRTEM image and a FFT of the marked square area for one nanoparticle.

Figure D-1 Bring-field TEM images for four samples, synthesized at different temperatures and electron diffraction patterns.

Figure D-2 Room-temperature magnetization of four magnetite samples, synthesized at different temperatures.

Figure E-1 Dependence of collision probability P_n (n=0, 1, 2, 3) on thickness parameter t/λ_i. The thickness for FeF_2 specimens is around t/λ_i =0.10, as labeled by the shadowed slice.

Figure E-2 Low loss spectrum for a FeF_2 film.

List of Abbreviations

AES	Auger electron spectroscopy
BF	bright field
CFEG	cold field emission gun
CL	cathodoluminescence
DOS	density of states
EBL	electron-beam lithography
EDX	energy dispersion spectroscopy of x-ray
EELS	electron energy-loss spectroscopy
ELNES	energy loss near-edge structures
EXAFS	extended x-ray absorption fine structures
EXELFS	extended energy loss fine structures
FFT	fast Fourier transform
FMS	full multiple scattering
FWHM	full width of half magnitude
HAADF	high-angle annular dark-field
HRTEM	high-resolution transmission electron microscopy
HSQ	hydrogen silsesquioxane
IL	intermediate lens
IP	ion pump
LDOS	local density of states
LL	load lock
LM	Lorentz microscopy
MBE	molecular beam epitaxy
MOKE	magneto-optical Kerr effect
NWs	nanowires
OA	objective aperture
OL	objective lens
PL	photoluminescence
PPMS	physical properties measurement system

RGA	residual gas analyzer
RSMS	real-space multiple scattering
SAA	selected area aperture
SAED	selected-area electron diffraction
SCF	self-consistent field
SEA	spectrum entrance aperture
SFEG	Schottky field emission gun
SLS	solid liquid solid
SO	spectrometer object
STEM	scanning transmission electron microscope
TEM	transmission electron microscope
TM	transition metals
TMP	turbo molecular pump
TSM	Ti sublimation pump
UHV	ultra high vacuum
UPS	ultraviolet photoelectron spectroscopy
VLS	vapor liquid solid
VS	view screen
WLR	white line ratio
XANES	x-ray absorption near-edge structures
XPS	x-ray photoelectron spectroscopy
XAS	x-ray absorption
ZLP	zero loss peak

List of symbols

a, b, c	lattice parameters of crystal structure
a_0	Bohr radius
d	localization diameter
D	diameter of spherical nanoparticle
D_{4h}	tetrahedral symmetry
$d\sigma/dE$	differential cross section
e	electron charge
E	energy loss
E_0	incident beam energy
E_f	final state energy
E_F	fermi energy
F_{eff}	effective scattering amplitude
$\hbar$	Planck's constant
H_c	coercivity
i, j	index number
I_0	intensity of the incident beam
k	wave number
$\boldsymbol{K_0}$	initial wave vector
$\boldsymbol{K_f}$	final wave vector
K_s	surface anisotropy
K,L,M	edges arising from the transition from the 1st, 2nd, 3rd shells
l, m	the angular momentum and magnetic quantum numbers
L23	L23 edges
m_e	electron mass
M	magnetization
M_s	saturation magnetization (1.714×10^6 A/m for iron)
$M(E)$	atomic matrix
$N(E)$	density of final states
$\boldsymbol{q}$	change of the wave vector during scattering
$\boldsymbol{r}$	coordinate for incident electron
$\boldsymbol{r_j}$	coordinate for target atom electrons
v	speed of electrons
$V(\boldsymbol{r})$	interaction potential of electrons
Z	atomic number
α	convergence semiangle
β	divergence (collection) semi-angle
ε_0	dielectric constant of free space
γ	relativity constant
λ	electron wavelength
$\lambda_i(E)$	energy-dependent inelastic mean free path
μ_0	permeability of free space ($4\pi \times 10^{-7} N/A^2$)
$\mu(E)$	transition rate from initial to final states (or called cross-section)
θ	scattering angle

$\sigma(E)$	absorption cross-section
ψ_0	wave function of the initial state
ψ_n	wave function of the final state
Δ	energy window
Ω	solid angle
$\Gamma_i(E)$	initial-state lifetime (or called core-hole) broadening
$\Gamma_f(E)$	final-state lifetime (or called excitation) broadening
$\|i\rangle$, $\|j\rangle$	initial and final state of the target atom in the Dirac representation

Chapter 1 Introduction and background

1.1 Introduction

Electron energy-loss spectroscopy (EELS) offers the possibility of chemical analysis at nearly atomic length scale by measuring electron excitation in materials, in the context of a modern transmission electron microscope (TEM).[1] EELS shows its advantage in low-concentration and light-element analysis,[2, 3] and is also applicable to electron-sensitive materials, as studied in biological sciences.[4] One most information-wealthy and interpretation-challenging aspect of EELS is the *energy loss near-edge structure (ELNES)*, the intense fluctuations within 50 eV of core-loss edge onset. Simultaneous analysis of atomic structure and chemical state of materials can be performed in a scanning TEM (STEM).[5, 6] ELNES resolves the valence or bonding state of atoms within a small electron probe.[7, 8] Such kind of applications have been well shown by recent work involving some challenging nanostructural materials, including individual nanotubes,[9] interfaces in structural materials,[10] dislocations in GaN semiconductors[11] and nanoparticulate system.[12]

In interpretation of ELNES features, the so-called "*fingerprinting*" is a direct and easy approach. It involves looking for common features of an edge in unknown samples and comparing them to the same edge of known compounds. EELS ATLAS, a complete collection of "fingerprints" for most of elements across the whole periodic table, should be the best reference in this purpose.[13] Beyond "fingerprinting" technique, a theoretical calculation with sufficient predictive power is useful in interpreting ELNES features, especially for complex materials of unknown structure. Recent advances in instrumentation have significantly improved the energy and spatial resolution, to levels of 0.1 eV and 0.1 nm.[14] Experimental spectra of such high-energy resolution can be compared with *ab-initio* calculations, improving the reliability of the spectral interpretation. However, when measuring at such high spatial resolution, the signal-to-noise ratio can be low, as a result of a limited exposure time and electron dose to avoid specimen drift and radiation damage. Developing new "fingerprints" of high sensitivity to

changes in electronic structure is therefore imperative, especially for ELNES at higher energy losses. Calculations by the real space multiple-scattering (RSMS) method, on clusters of sequentially increasing size, allows spectral changes to be directly correlated to structural and electronic properties of materials.[15] ELNES spectral interpretation using the RSMS approach, and thereby developing new "fingerprints" for studies of nanostructures is one of the main subjects in this thesis research.

The *white-line ratio* (WLR), a measure of the 3d-orbital occupancy, is widely used to evaluate the valence state of transition metals (TMs).[1,16,17,18] As I will show in this thesis, white-line ratios can be obtained by using a standard fitting program and used for phase identification of iron nanoparticles. A postpeak in the 3d transition metal L-shell ELNES appears upon oxidization of TMs, as demonstrated in the experiments in this thesis and by reference to data in the EELS Atlas.[1] Also, a characteristic pre-edge peak (prepeak) appears in the O-K edge when oxygen atoms are chemically bonded to 3d transition metals.[18,19,20] RSMS calculations using clusters of increasing size establish that the postpeak originates from photoelectron backscattering by the nearest-neighbor oxygen atoms, and that the prepeak comes from the hybridization of oxygen 2p states with 3d transition-metal orbital. Therefore their appearance provides a clear indication of the presence of oxygen in the near vicinity of TM atoms. Calculation shows that the peaks are sensitive indicators: even a slight amount of oxidation results in a detectable postpeak in the TM L-edges and prepeak in the oxygen K-edge. Therefore they have practical advantages for identifying local electronic structure, for example in an interface. This is demonstrated in the thesis by detecting the oxidation of iron nanoparticles embedded in a SiO_2 matrix or encapsulated at the end of nanowires.

Metallic nanoparticles have been extensively studied due to the richness of their physical properties and the wide range of potential applications, such as in high-density data storage, magneto-optical sensors and catalysts. One potential problem common to nanoparticles is oxidation arising from their large surface area to volume ratio; they are easily degraded by exposure to the air. Nanoparticles embedded in an insulating matrix, the so-called nanocomposites, seem to offer a solution. It has been shown that iron nanoparticles well protected from oxidation can be made by implanting iron into optically transparent SiO_2 matrix.[21] Nevertheless, a problem of the ion implantation is size control;

a wide size distribution of the ion-implanted materials renders them less amenable to practical applications. As we will show in this thesis, well-protected, isolated bcc-iron nanoparticles embedded in silicon dioxide can be prepared by e-beam evaporation and post-annealing of multilayers in an ultra-high vacuum (UHV). The method allows us to control of the size of Fe nanoparticles and to protect the nanoparticles from oxidation in air. In particular, nanocomposite films are compatible with patterning techniques, such as e-beam lithography (EBL), which can be used for further particle-size and ordering control. Such an approach is promising in fabricating desired arrays of discrete metallic nanoparticles with size well below 10 nm. Meanwhile, these iron nanoparticles can be used for synthesis of nanotubes and nanowires from well-controlled sites; this is demonstrated by the growth of arrays of silicon oxide nanowires from patterned reagents, as shown in this thesis.

For such metallic nanoparticles, microstructural analysis is critical for understanding their physical properties. For example, atoms at a surface or interface, often oxidized or bonded to the matrix material, can have a greatly different phase state than atoms distant from the interface. Electron and x-ray diffraction are ideal for identifying the crystallographic structure of materials but provide only average properties, making it difficult to detect local changes. High-resolution TEM and scanning TEM (STEM) show the crystal structure on an atomic level, but the chemical state of species at the nanoparticle-matrix interface can be difficult to deduce. Therefore it is important to develop convenient methods for characterizing the properties of the particle-matrix interfacial layer, such as its oxidation state, as an aid to interpret physical properties.

Nanofabrication and nanoanalysis are always complementary to each other, and this is also the case for the present study. In this study, processes were developed to fabricate iron nanoparticles and silicon oxide nanowires (NWs). Detailed microstructural and electronic analysis of the fabricated iron nanoparticles and silicon oxide NWs were conducted by TEM imaging and EELS techniques. The results provide an insight to the magnetic properties of the iron nanoparticles, and lead to a discussion of the growth mechanism of silicon oxide NWs.

Ultra high vacuum (UHV) and electron energy-loss spectroscopy (EELS) are two main techniques used in this study and thus introduced in section 1.2. Interpretation of energy-loss near-edge structure (ELNES) and its application in characterizing the nanostructures are central to this thesis research, so the theoretical background, recent developments, calculation of ELNES are summarized in section 1.3. Finally an outline of the thesis, as well as the main issues dealt with in each chapter, is given in a fourth section of Chapter 1.

1.2 Experimental techniques

Experimental work is at the core of this thesis research. It ranges from various sample preparation techniques, using electron-beam and thermal evaporation in an ultra-high vacuum (UHV) system, to advanced characterization, by electron microscopy, spectroscopy and by magnetization measurements. Of the various experimental techniques, EELS and UHV were extensively used in this study and thus their instrumentation and methods are outlined in this section.

1. 2.1 Electron energy-loss spectroscopy

An electron, when passing through materials, can be scattered elastically by nucleus, or scattered inelastically by the atomic electrons; the former is used for TEM imaging and diffraction, and the latter for energy loss spectroscopy (EELS) that provides rich chemical information.[1] Some instrumental aspects of EELS relevant to this thesis research are outlined in this section.

1.2.1a Magnetic prism

A Magnetic prism is the basic component of a spectrometer system. Figure 1-1 (a)(b) shows the schematic diagram of the spectrometer optics, typically for a Gatan spectrometer installed beneath the camera system of a TEM. Similar to other electromagnets, the magnetic prism applies a perpendicular force to the incoming electrons by magnetic field B produced from the polepieces, fulfilling three roles.[1]

- *Bending* the beam through an angle (90^o in general).
- *Dispersing* the electron beam according to their kinetic energy (after certain energy loss), since the radius $R = v(\gamma m_0/eB)$.

- *Focusing* the electrons of a given energy loss to a point, both in the plane of the spectrometer Fig.1-1 (a) and in the perpendicular plane (b).

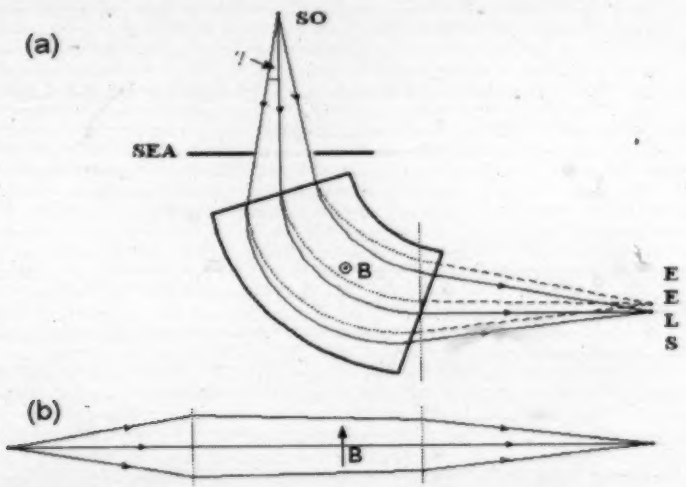

Figure 1-1 The dispersion and focusing of electrons in a magnetic prism (a) in the bend plane of spectrometer and (b) in a plane normal to the bend plane. (From Ref. 1)

1.2.1b Two TEM modes

In normal TEM operations, the crossover formed by the projector lens acts as the object point of the spectrometer (SO); the optics is illustrated in Figure 1-2. SO contains an image or diffraction pattern, depending on the TEM modes.

Image mode (diffraction-coupled spectrometer): a magnified image of the specimen is present on the viewing screen and the *spectrometer object* (*SO*) plane (or called projector-lens crossover) contains a diffraction pattern (DP), shown in the left of Figure 1-2.

- Collection semi-angle β is determined by the objective aperture (OA): $\beta=0.5d/f$, d is the objective-aperture diameter and f the focal length of the objective lens; if no OA inserted, β is typically 100-150 mrad.
- The area of analysis is normally selected by the spectrometer entrance aperture (SEA), and the lateral displacement due to chromatic aberration has to be considered; therefore imaging mode is not good for quantitative analysis.

Diffraction mode (image-coupled spectrometer): A diffraction pattern is formed on the viewing screen, while the projector crossover contains an image of the illuminated area of the specimen, shown in the right of Fig. 1-2.

- The collection angle is usually determined by the selected area aperture (SAA): $\beta=0.5D/[L(V'/V)]$. In which the D is the SEA diameter and L is the cameral length, V' and V are the distances from the projector lens to the screen and to the SEA plane, respectively. This mode is good for quantitative chemical analysis at small sample areas.
- Diffraction mode has advantage of high spatial resolution or strong signal: the illumination region (in the specimen plane) can be in nano scale, being selected by the selected area aperture (SAA); or the electron beam can be spread to many micrometers in decreasing the radiation damage and meanwhile obtaining strong enough signal for chemical analysis. The core-loss EELS spectra reported in this thesis were recorded mostly in the diffraction mode.

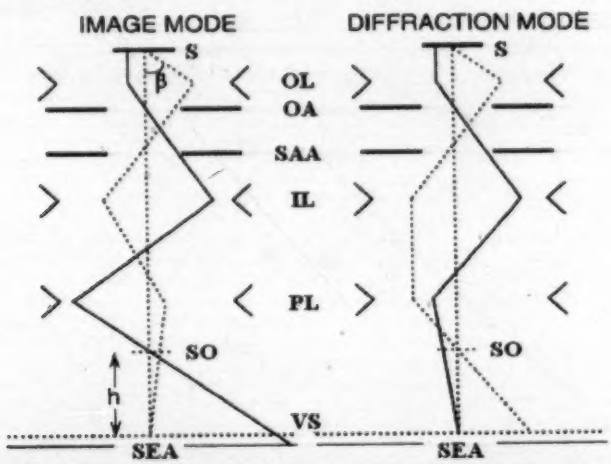

Figure1-2 Simplified optics for two TEM modes in recording EELS: imaging (left) and diffraction (right) modes. S represents specimen, OL objective lens, OA, objective aperture, SAA selected area aperture, IL intermediate lens, PL projection lens, VS viewing screen, SO spectrum object, and SEA spectrum entrance aperture. (from Figure 2.16, in Ref. 1)

1.2.1c Energy resolution of EELS

In the literature, the energy resolution is generally defined as the full-width at half maximum of the zero-loss peak. There are mainly four (instrumental) factors affecting

the practical energy resolution in EELS: (a) the energy spread of the electron source, (b) the non-isochromaticity of the spectrometer, (c) the point spread (blurring) of the detector, and (d) instabilities in the TEM high voltage, the spectrometer energy dispersion and the stray magnetic field*.[22]

Usually, the energy spread of the electron source is the main limitation to the energy resolution, and is of the order of 1 eV for a thermionic source, and possibly as low as 0.23 eV for a cold field-emission gun.[23] Electron monochromators can push the resolution down below 0.2 eV.[23,24] It should be made clear that, besides those factors above, there are more broadening effects to the high-energy loss (or core-loss) spectrum, including:

- Initial life-time broadening determined by the uncertainty relations.
- Final-state broadening arising from the limited mean free path of the photoelectron.
- Degradation due to TEM chromatic aberration†

Those factors will be discussed in Section 3 in dealing with ELNES.

1.2.1 d Comparison of EELS with other techniques in studies of nanostructures

Electron energy-loss spectroscopy (EELS) shows advantage of much higher spatial resolution in studies of the chemical and electronic structures of materials, in comparison with other spectroscopic techniques. The main reason is that fast electrons‡ (being charged particles) can be well controlled by electro-magnetic interactions (i.e. through the electrostatic or magnetic lenses). A combination of imaging and chemical analysis at nearly atomic level is possible in an advanced TEM.

A comparison of EELS with other techniques is given in Table *1-1*. The spatial and energy resolutions eventually depend on the probe and detector used in the techniques. EELS, Auger electron spectroscopy (AES), energy dispersive spectroscopy of X-ray (EDX) and cathodoluminescence (CL) all use electrons as probes, giving higher spatial resolution. CL, X-ray absorption spectroscopy (XAS), photoluminescence (PL), X-ray photoelectron spectroscopy (XPS) and ultraviolet photoelectron spectroscopy

* So moving of a metallic chair should be avoided during spectrum recording.

† It can be minimized by selecting low eV/ch and increasing the high voltage, and by focusing the spectrum using the feature of interest.

(UPS) use photons as detectors, giving higher energy resolution. Thin specimens (below 100 nm) are required in recording EEL spectrum in a transmission mode. Bulk samples can be used in other techniques, which, however, are in surface modes.

On the other hand, EELS (as well as AES and XAS), as an absorption spectroscopy, differs from the emission spectroscopy in that it probes the unoccupied density of states and the latter probes the occupied density of states.

Table 1-1: a comparison of EELS with other spectroscopic techniques, in the probe, the spatial and energy resolutions, and the sample requirement.

techniques	probe	energy resolution	sample	spatial resolution
EELS	electrons (100K-1MeV)	1 eV (LaB_6) 0.7 eV (SFEG) 0.3 eV (CFEG)	thin film	1 nm
AES	electrons (1-30 KeV)	~1 eV	bulk	100 nm
EDX	electrons (100 K-1 MeV)	100 eV	thin film[§]	100 nm
CL	electrons (1-30 KeV)	1 meV	bulk	100 nm
XAS	photons (100-5 K eV)	1 meV	bulk[**]	1 mm
PL	photons (adjustable)	1 meV	bulk	1 μm
XPS	photons (2 KeV)	200 meV	bulk	1 mm
UPS	photons (20 eV)	100 meV	bulk	1 mm

1.2.2 Ultra high vacuum (UHV)

High quality samples used in this work were prepared in an ultra high vacuum (UHV). A photo was taken for the whole system, and the main components were labeled, as shown in Figure 1-3. Some important components are out of view, such as control panels for deposition and power supplies and turbo molecular pumps.

The UHV system has *seven* parts basically:

Chambers: load lock (LL), RAPID (a transfer station connecting all other chambers), molecular beam epitaxy (MBE), and pulsed laser deposition (PLD, not used in this thesis work)

Sources: three e-gun sources and one thermal source

Pumps: scroll pumps, ion pumps (IP), turbo molecular pumps (TMP) and Ti-sublimation pumps (TSP)

Control panels: for pumps, deposition and baking

Monitoring system: residual gas analyzer (RGA), and various vacuum gauges

[‡] A high voltage (100 K-1MeV) applied to achieve a big mean free path.
[§] Also bulk sample can be used for EDX in a scanning electron microscope (SEM).

Power supplies: for electron beam and thermal evaporation

Annealing system: composed of control panel and resistive wires (in MBE)

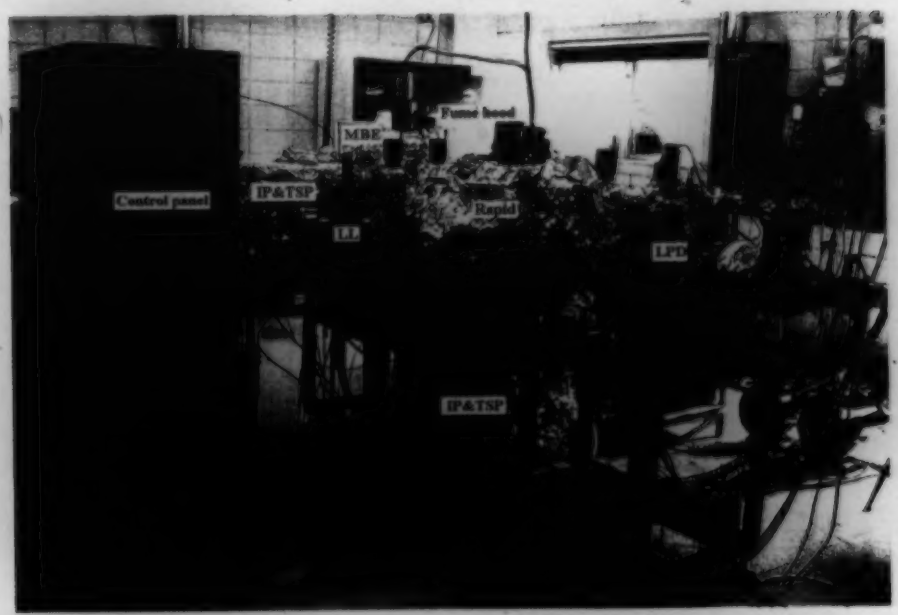

Figure 1-3 Photo of the UHV system used for sample preparation in this thesis work (courtesy of Dr. A. Meldrum)

A schematic representation of pumping stages for chambers is shown in Figure 1-4. In order to reach the UHV regime in the RAPID and MBE chambers, different pumping stages are necessary. The pre-vacuum is obtained using a pumping stage made of a turbo molecular pump (TMP) and a scroll pump; the chambers can reach a pressure of about 10^{-8} Torr in a couple of hours. Then an ion pump (IP) coupled with a Ti-sublimation pump (TSP) (both for RAPID and MBE) is used to reach a pressure of about 10^{-9} Torr. To reach even high levels of vacuum, a bake-out is needed, using the halogen bulbs and resistive tapes; the whole chamber is heated up to a temperature of about 120-200°C for 3 days (or more if necessary) in order to accelerate the desorption of water vapor and other gases from all inner walls of the chambers. After that the system is cooled down and the pressure can finally reach $1x10^{-10}$ Torr or even lower. One can see the time-consuming nature of the whole procedure and the necessity to reduce the exposure to air; ideally, the Rapid and MBE chambers should be kept at an UHV regime

all the time. For this purpose, it is important to use a fast load-lock (LL) chamber, to introduce and extract samples without breaking the vacuum.

In a typical sample preparation, the sample is firstly introduced into LL chamber and the chamber is pumped down to 10^{-8} Torr by TMP and scroll pumps, then the sample is baked at about 150°C overnight and then transferred to the RAPID chamber after cooling down to about 100°C. During the transfer, the pressure in the Rapid may rise to 10^{-9} Torr, and it needs about one hour to pump down to the 10^{-10} Torr range using the IP and TSP. At this point, the sample can be transferred to the MBE chamber, where film deposition and annealing (if necessary) are done. One can refer to the well-written manual for film deposition in the lab; the general procedure for an in-situ annealing in MBE is given in Appendix 1.

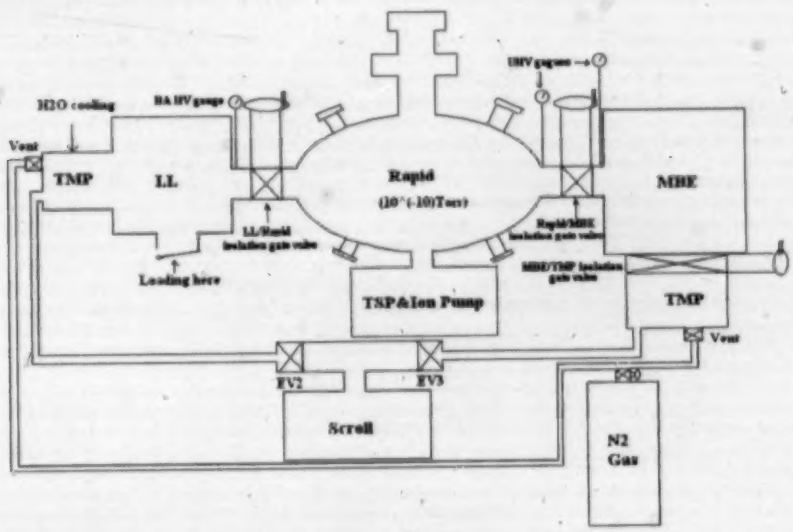

Figure 1-4 Schematic view of the UHV pumping system.

1.3 Basic theory of ELNES

Electron energy-loss near-edge structures (ELNES) are the electron-beam counterparts of x-ray absorption near-edge structure (XANES). Both ELNES and EXANES measure the probability of excitation of a core electron to unoccupied states. The concepts for XANES that have been developed for many years, are also applicable to ELNES. The information that can be obtained by ELNES is almost identical to that of XANES, but

ELNES in a transmission electron microscope (TEM) offers the advantage of higher spatial resolution.

1.3.1 ELNES: a site-specified and symmetry-projected DOS

When an electron beam passes through a sample, the incident electrons can be scattered by certain sample atoms (called target), resulting in an energy and momentum transfer from the incident electron to the target atoms. This is an inelastic scattering process. Figure 1-5 illustrates the scattering geometry for an electron with initial energy E_0 and momentum $\hbar\mathbf{k}_0$, and a final energy of E_1 and momentum $\hbar\mathbf{k}_1$. When passing through the sample, the electron is scattered through an angle θ, losing an energy $E = E_1 - E_0$ and momentum $\hbar\mathbf{q} = \hbar(\mathbf{k}_0 - \mathbf{k}_1)$. The target atom in an initial state of wavefunction Ψ_0 makes a transition to a final state of wavefunction Ψ_n. To understand the scattering process, the quantum mechanical nature of the target must be taken into account. Since the energy of interaction between the incident electron and the target atom is much smaller than the kinetic energy of the incident electron (i.e. typically 200 keV), the differential cross-section (in terms of solid angle Ω) for the transition can be calculated within the first Born approximation:[††]

$$\frac{d\sigma_n(q,E)}{d\Omega} = \left(\frac{m}{2\pi\hbar^2}\right)^2 \frac{k_1}{k_0} \left| \int V(r)\Psi_0\Psi_n \exp(iq\cdot r)d\tau \right|^2 \delta(E + E_i - E_f) \qquad (1.1)$$

here *V(r)* is the interaction potential between the incident electron (coordinate ***r***) and the target atom electrons (coordinate $\boldsymbol{r}_j$), including the Coulomb attraction by the nucleus and the sum of Coulomb repulsion of each atomic electron:

$$V(r) = -\frac{1}{4\pi\varepsilon_0}\left[\frac{Ze^2}{r} - \sum_{j=1}^{Z}\frac{e^2}{|\mathbf{r}-\mathbf{r}_j|}\right] \qquad (1.2)$$

The integral of the first term (nuclear contribution) is zero because of the orthogonality of the initial- and final-state wavefunctions; only electron-electron interaction contributes to an inelastic scattering process shown in the second term. [1]

[††] Under the assumption that the incoming plane wave (of the fast electron) is not substantially altered by the potential.

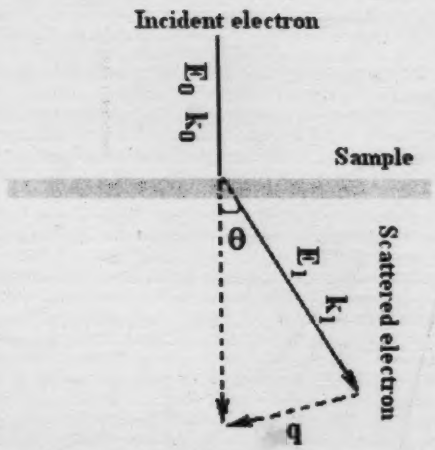

Figure 1-5 Geometry of an inelastic scattering process

The integral of the second term in Eq. (1.2) over ***r*** in Eq. (1.1) can be solved by the Bethe approximation:[25]

$$\int \frac{\exp(i\mathbf{q}\cdot\mathbf{r})}{|\mathbf{r}-\mathbf{r}_j|}d\mathbf{r} = \frac{4\pi}{q^2}\exp(i\mathbf{q}\cdot\mathbf{r}_j) \tag{1.3}$$

Consequently the differential cross section can be written as:

$$\frac{d\sigma_n(E,q)}{d\Omega} = \left(\frac{m_e^{\,2}}{2\pi\varepsilon_0\hbar^2}\right)^2\left(\frac{k_1}{k_0}\right)|<\Psi_n|\sum_j \exp(i\mathbf{q}\cdot\mathbf{r}_j)|\Psi_0>|^2\ \delta(E+E_i-E_f) \tag{1.4}$$

in which $|\Psi_0>$ and $|\Psi_n>$ are the initial and final state of the target atom in the Dirac representation. To correlate the cross-section to the spectrum intensity as discussed below, the angular and energy dependence of the scattering of the interaction represented by a double-differential cross-section must be calculated:

$$\frac{d^2\sigma(E,q)}{d\Omega dE} = \frac{4\gamma^2}{a_0^2 q^4}\left(\frac{k_1}{k_0}\right)\frac{d}{dE}\sum_n[|<\Psi_n(E)|\sum_j \exp(i\mathbf{q}\cdot\mathbf{r}_j)|\Psi_0(E)>|^2\delta(E+E_i-E_f) \tag{1.5}$$

here γ and a_0 are the relativity constant and Bohr radius respectively.

The core state, $|\Psi_0>$, are localized. We can define a basis $|\Psi_{i,L}(E)>$, in which *i*, *L(l, m)* are indexes for the site, angular momentum, and assume $|\Psi_{i,L}(E)>$ is complete with respect to the core state: [26]

$$\sum_{all\,i,L,E_n} |\psi_{i,L}(E_n)><\psi_{i,L}(E_n)| = 1 \tag{1.6}$$

Substitution of Eq. (1.6) into Eq. (1.5) gives

$$\frac{d^2\sigma(E,q)}{d\Omega dE} = \frac{4\gamma^2}{a_0^2 q^4}\left(\frac{k_1}{k_0}\right)\frac{d}{dE}\sum_n\sum_{i,L}|<\Psi_n(E)|\psi_{i,L}(E_n)>$$

$$\times <\psi_{i,L}(E_n)|\sum_j \exp(i\mathbf{q}\cdot\mathbf{r_j})|\Psi_0(E)>|^2\ \delta(E+E_i-E_f) \qquad (1.7)$$

The expression is nonzero only when $E_n \equiv E+E_c$ (where $E_c = E_f - E_i$ is the binding energy). And so the second term in Eq. (1.7) is taken out of the summation to have

$$\frac{d^2\sigma(E,q)}{d\Omega dE} = \frac{4\gamma^2}{a_0^2 q^4}\left(\frac{k_1}{k_0}\right)\sum_{i,L}|<\psi_{i,L}(E_{E+E_c})|\sum_j \exp(i\mathbf{q}\cdot\mathbf{r_j})|\Psi_0>|^2$$

$$\times\frac{d}{dE}\sum_n|<\Psi_n|\psi_{i,L}(E_n)>|^2\ \delta(E+E_i-E_f) \qquad (1.8)$$

The cross-section can be defined in terms of specific i, L (a specific site, angular-momentum), resulting in

$$\frac{d^2\sigma(E,q)}{d\Omega dE}_{i,L} = \frac{4\gamma^2}{a_0^2 q^4}\left(\frac{k_1}{k_0}\right)|<\psi_{i,L}(E+E_c)|\sum_j \exp(i\mathbf{q}\cdot\mathbf{r_j})|\Psi_0>|^2$$

$$\times\frac{d}{dE}\sum_n|<\Psi_n|\psi_{i,L}(E_n)>|^2\ \delta(E+E_i-E_f) \qquad (1.9)$$

Now Eq. (1.9) contains two terms , one of which is generally termed the atomic transition matrix

$$M(E) = <\psi_{i,L}(E+E_c)|\sum_j \exp(i\mathbf{q}\cdot\mathbf{r_j})|\Psi_0> \qquad (1.10)$$

The atomic transition atomic matrix in Eq. (1.10) can be further simplified by making the *one-electron approximation*: excitation of an inner-shell electron is assumed to have no effect on the other electrons of the atom, namely

$$<\psi_f(E+E_c)|\sum_j \exp(i\mathbf{q}\cdot\mathbf{r_j})|\Psi_0> = \sum_j <\psi_f(E+E_c)|\exp(i\mathbf{q}\cdot\mathbf{r_j})|\Psi_0> \qquad (1.11)$$

The second term in the right side of Eq. (1.9) corresponds to the density of states, explicitly:

$$N(E) = \frac{d}{dE}\sum_n|<\Psi_n|\psi_{i,L}(E_n)>|^2\ \delta(E+E_i-E_f)) \qquad (1.12)$$

Consequently Eq. (1.8) can be simply rewritten as

$$\frac{d^2\sigma}{d\Omega dE} = \frac{4\gamma^2}{a_0^2 q^2}|M|^2\ N(E) \qquad (1.13)$$

where the labels *i*, *L* have been omitted for clarity. M (E) is a slowly varying function of energy loss, to a first order approximation, and *N(E)* (actually a matrix including the excited electron's interaction with the surrounding atoms) determines the near-edge fine structures. Remembering that the atomic electron takes a transition from core-level state, highly localized on the excited atom, to an empty state above the Fermi level, we can say that *N(E)* is the unoccupied *local* (or *site- specified*) *density of states (LDOS).*

For a thin specimen in which plural scattering is negligible, the inner-shell contribution to the energy-loss spectrum (recorded with a collection semiangle β) is the single-scattering intensity $J_k^1(\beta, E)$, given by

$$J_k^1(\beta, E) = NI_0 d\sigma / dE \tag{1.14}$$

Here N is the number of atoms per unit specimen area contributing to the ionization edge and I_0 is the integrated zero-loss intensity.

1.3.2 Dipole approximation

1.3.2a Dipole approximation

For small q ($q \ll 1/r_c$, where r_c is the radius of the initial state),[1] the exponential in Eq. (1.11) can be expanded as:

$$\exp(i\mathbf{q}\cdot\mathbf{r}_j) = 1 + i(\mathbf{q}\cdot\mathbf{r}_j) - \frac{q^2}{2}(\mathbf{q}\cdot\mathbf{r}_j)^2 + \cdots \tag{1.15}$$

The first term does not contribute to the cross-section because the initial and final state wave functions are orthogonal. And if $(\mathbf{q}\cdot\mathbf{r}_j)$ is small, such as $(\mathbf{q}\cdot\mathbf{r}_j) \ll 1$, only the second term gives an appreciable contribution to the cross-section, representing a dipole transition, i.e. $\Delta l = \pm 1$; other high-order (multipole) terms can be neglected. So, dipole approximation is generally used in the atomic matrix in Eq. (1.11)

$$\langle \psi_f(E+E_c) | \exp(i\mathbf{q}\cdot\mathbf{r}_j) | \Psi_0 \rangle = i\mathbf{q} \langle \psi_f(E+E_c) | \mathbf{r}_j | \Psi_0 \rangle \tag{1.16}$$

A complete correspondence between the ELNES and XAS (x-ray absorption spectrum) is expected for small $\boldsymbol{q}$; Eq. (1.13) can be rewritten as[27]

$$\frac{d^2\sigma}{d\Omega dE} = \frac{4\gamma^2}{a_0^2 q^2}[|M_{l+1}|^2 N_{l+1}(E) + |M_{l-1}|^2 N_{l-1}(E)] \tag{1.17}$$

in which $M_{l\pm1} = <\Psi_{f_{l\pm1}} | \mathbf{r} | \Psi_{i_l} >$. In the dipole approximation, the observed DOS is a *symmetry-projected* density of states, for example, the modulation in K-edge intensity reflects mainly the density of 2p final states.

1.3.2b Non-dipole transition

If $\boldsymbol{q}$ is not small, higher-order terms, such as the third term in Eq. (1.15) can no longer be ignored. They give rise to monopole ($\Delta l = 0$) and quadrupole ($\Delta l = \pm 2$) transitions.[27] For example, a small peak located at about 1.5 eV below the band edge was recently observed in the Li-K edge of Li_2O, which is attributed to a monopole transition, i.e. from Li 1*s* to an exciton of *s* symmetry.[28]

1.3.3 Limitations in energy and spatial resolution

1.3.3a Energy broadening

The broadening of ELNES features has three origins: the core-hole lifetime (or called initial state, Γ_i), the lifetime of the excited state (or called final state, Γ_f), and the instrumentation broadening (ΔE).

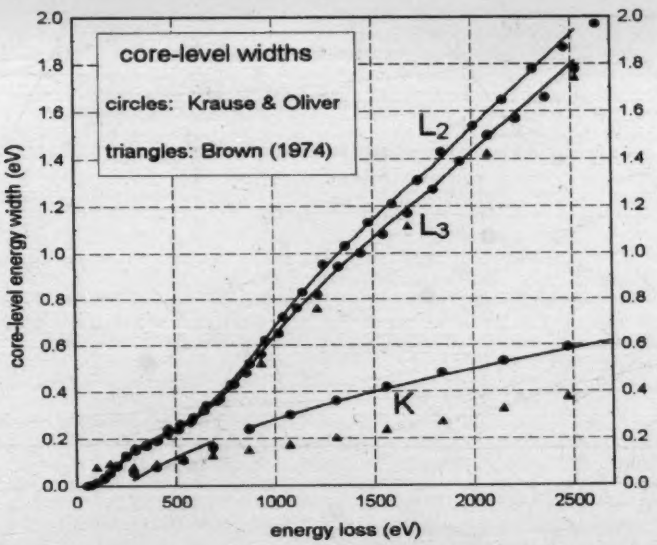

Figure 1-6 Core-level widths of K and L edges versus threshold energy.

Instrumentation broadening ΔE is generally mentioned in describing the energy resolution of a TEM and defined as the FWHM of the zero-loss peak (ZLP). It has been improved rapidly in recent years, for example by using a field-emission gun and/or a

monochromator. For a TEM equipped with a field emission gun, ΔE~0.6-0.7 eV; the resolution can be pushed down to 0.1 eV, for a system equipped with a monochromator. *Initial-state lifetime broadening* The core level has a natural energy width determined by the uncertainty relation: $\Gamma_i \tau_h = \hbar$, where τ_h is the core hole lifetime, determined by the speed of the de-excitation mechanism. For example, Fe-L_3 is slightly sharper than L_2 because of the rapid decay of the excited states through the *Coster-Kronig transition* in the latter: Fe-L_2 ionization can be rapidly compensated by an electron from the L_3 shell filling the hole and ejecting an Auger electron from the d shell. A conduction-band electron could also fill the L_2 core hole, but the L_3 core hole can only be filled from the conduction band. The value of Γ_i is low and depends mainly on the threshold energy of the edge. Figure 1-6 shows the natural width of the K and L edges as a function of threshold energy, from Ref. 24

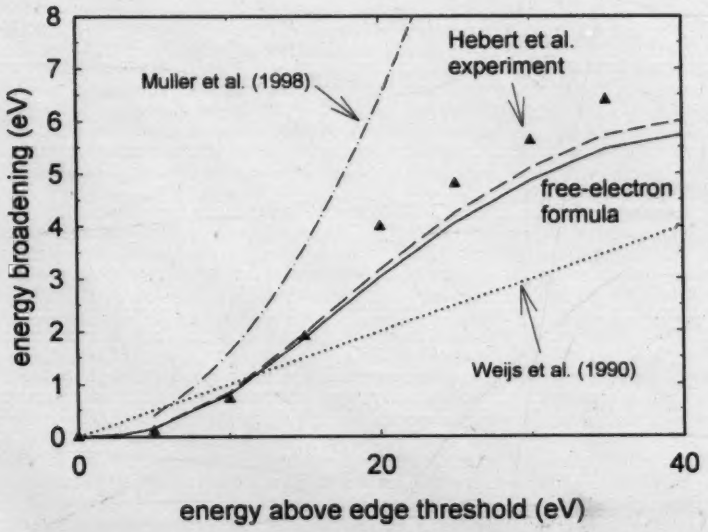

Figure 1-7 Comparison of the final-state lifetime broadening for Al-L edge, obtained from experiments or calculations (from Ref. 24). The solid line is calculated using free electron mass, and the dashed line using effective electron mass.

Final-state broadening arises from the limited mean free path λ_i (typically a few nanometers) of the excited electrons. At the threshold, Γ_f is zero because of the infinite λ_i (or excited state lifetime), and increases with increasing energy, resulting in

broadening in the extended-energy region, such as in EXELFS. Different methods have been employed to obtain the final-state broadening, giving different energy dependence of $\Gamma_f(E)$, as shown above in Figure 1-7. For example, Weijs et al. used an empirical linear relation ($\Gamma_f(E)=0.1E$);[29] Muller et al. used a theoretical formula obtained from random phase approximation (RPA);[26] and Egerton proposed that the $\Gamma_f(E)$ can be determined by a free electron approximation.[24] The result fits the Herbert's experimental data rather well.[30] In simple terms, after transition to an outer-shell level, an excited electron is left with a kinetic energy $E_{kin} = E - E_b$ (E is energy loss and E_b the edge-threshold energy). If taken to be a free particle, the ejected electron moves with a speed of $v = 2E_k / m_0$ and then is scattered inelastically by the surrounding atoms, with a *mean free path* λ_i (a function of kinetic energy). So the $\Gamma_f(E)$ can be estimated from the Heisenberg uncertainty relation:

$$\Gamma_f(E) \sim \hbar / \tau_f \sim (2E_k / m_0)^{1/2} (\hbar / \lambda_i) \qquad (1.18)$$

We can see $\Gamma_f(E)$ increases with excitation energy, so the features well above the threshold are very broad; a monochromator can enhance the visibility of the near-threshold peaks, but has little effect on far-above-threshold peaks.

Monochromators can improve the energy resolution to below 0.2 eV, and in the case of a low-loss spectrum (E<50eV) they provide a great advantage in bandgap measurements.[22] The monochromators have, however, drawbacks, such as the low beam current (due to the brightness conservation). For ELNES, a high beam current is preferred due to the small scattering cross-section, and actually, the broadenings that are intrinsic to the core-loss often dominate the fine structure. Therefore a cold field-emission electron gun seems to be a preferable solution for reducing the instrumentation broadening.[23] An alternative way to improve the energy resolution of the ELNES is spectral processing using the various deconvolution methods. As routine measures, Fourier-log or Fourier-ratio procedures are used to remove the plural scattering.[1] More recently, maximum-likelihood deconvolution has been successfully employed to sharpen ELNES features; energy resolution can be pushed down to 0.2-0.3eV.[31]

1.3.3b Delocalization of inelastic scattering

Inelastic scattering has a fundamental-physics delocalization coming from the wave nature of the electrons, even recorded using an ideal instrument. An estimation of the energy dependence of the localization diameter (containing 50% of the scattered electrons) was derived (starting from Rayleigh criterion) by[32]

$$d \sim 0.8\lambda(E_0 / E)^{3/4} \qquad (1.19)$$

in which, λ and E_0 are the incident electron wavelength and energy respectively (determined by the accelerating voltage), E is the threshold energy. Immediately we can see the spatial resolution can be relatively poor for the low-loss spectra, the wave nature of the electron imposes a spatial localization limit of the order of 1 nm at energy loss below 100 eV.

The delocalization of the inelastic scattering (called nonlocality by the authors) was well illustrated in the spectrum imaging recently in a SiC system.[33] Atomic-resolution can be obtained using the high angle annular dark field (HAADF) imaging technique in a STEM mode, so that the Si and C columns (of 0.1 nm distance) were distinguishable, while integral EELS spectrum intensity of carbon K-edge detected by the probe on carbon column is much lower that on the silicon column, this actually comes from the fact that electrons can carry information about regions of the specimen that are located some (small) distance from their classical trajectories. With this in mind, one cannot simply connect a signal at a given probe position and the location of the atoms giving rise to that signal. This might be a concern for the next generation of the TEM with resolution down to sub-Å.

Delocalization of inelastic scattering, is a fundamental physical limit to the spatial resolution in nanostructual analysis by EELS, but the effect can be minor in analysis by ELNES (implied by Eq. (1.19)), in comparison to other factors such as beam spreading due to elastic scattering, radiation damage, lens aberration (chromatic and spherical), diffraction limits (due to apertures), and statistics of data recording (electron probe and specimen drift).[24]

1.3.4 Orientation dependence

Eq. (1.14) clearly shows the origin of the orientation dependence: it is the projection of the matrix element onto the scattering vector, and thus the choice of the scattering vector $\boldsymbol{q}$ selects oriented matrix elements. In an anisotropic crystal, the final state $|f\rangle$ has a definite directionality. The direction of $\boldsymbol{q}$ is determined by the scattering angle, variation of the matrix element may therefore be studied by recording spectra both as a function of scattering angle and crystal orientation. The orientation of the angular parts of the wave functions will reflect the local fields and thus the crystal structure of an anisotropic crystal.[34, 35]

As an example, let's assume $\boldsymbol{q}$ parallel the z direction of the xyz coordination of the sample, and substitute the Eq. (1.6) and (1.14) into Eq. (1.9), to have

$$\frac{d^2\sigma(E,q)}{d\Omega dE}_{|i,l,m} = \frac{4\gamma^2}{a_0^2 q^4}\left(\frac{k_1}{k_0}\right) q^2 \left|<\psi_{i,l,m}(E_{E+E_c}) \sum_{i,m,l} |\Psi_{i,m,l}(E_{E+E_c})><\Psi_{i,m,l}(E_{E+E_c})| \frac{\hat{z}}{R} |\Psi_0>\right|^2$$

$$\times \frac{d}{dE}\sum_n |<\Psi_n|\psi_{i,l,m}(E_n)>|^2 \, \delta(E+E_i-E_f) \qquad (1.20)$$

For simplicity, let's only consider K-edges, i.e. transitions from s to p states. Since the operator $\hat{z}/R$ applied to an initial s state creates a p_z state, and other terms are zero. Now we have three remaining terms containing (p_x, p_y, p_z). Here Cartesian coordination is used to replace the magnetic quantum numbers *(l, m)*. Finally, only the term containing p_z final states remains (since $<\Psi_{i,p_x}|\Psi_{i,p_z}>, <\Psi_{i,p_y}|\Psi_{i,p_z}> = 0$), namely

$$\frac{d^2\sigma(E,q)}{d\Omega dE}_{|i,p_z} = \frac{4\gamma^2}{a_0^2 q^4}\left(\frac{k_1}{k_0}\right) q^2 / R \left|<\psi_{i,p_z}(E_{E+E_c})|\Psi_{0,p_z}>\right|^2$$

$$\times \frac{d}{dE}\sum_n |<\Psi_n|\psi_{i,p_z}(E_n)>|^2 \, \delta(E+E_i-E_f) \qquad (1.21)$$

So Eq. (1.16) tells that we have a p_z-projected final states (p_z-*DOS*)

$$N_{p_z}(E) = \frac{d}{dE}\sum_n |<\Psi_n|\psi_{i,p_z}(E_n)>|^2 \, \delta(E+E_i-E_f)) \qquad (1.22)$$

In an experiment, ELNES reflects the partial density of final states projected onto the direction of $\boldsymbol{q}$. This means that we can change the direction of $\boldsymbol{q}$ (either by tilting the specimen relative to the beam, or by changing the scattering angle), to select a certain projected final states of an anisotropic crystal.

ELNES, with its unique high-spatial resolution, has been used to study the anisotropic properties of graphite and hexagonal boron nitride,[34] superconductors, such as MgB_2,[36,37] semiconductors, such as GaN[38] and nanostructures, such as ZnO nanobelts.[39]

One practical question in momentum-resolved ELNES is the momentum resolution; high momentum resolution is desirable, for example, in the study of momentum-dependence of band-structure in crystalline samples. The momentum resolution can be increased, such as by raising the specimen above eucentric plane, a geometry proposed by Midgley,[40] but at the expense of spatial resolution according to the Heisenberg uncertainty relation or the Rayleigh criterion for resolution.

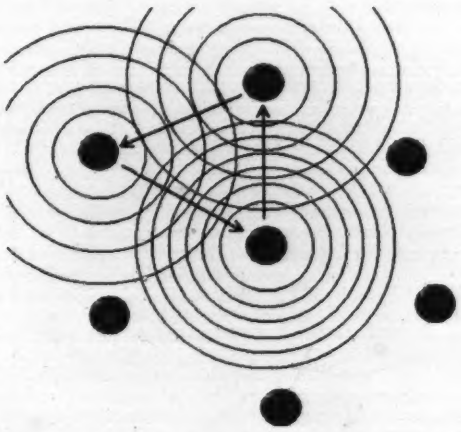

Figure 1-8 Schematic illustration for the multiple scattering of the outgoing wave reflected off from the surrounding atoms.

1.3.5 *ab initio* calculations

1.3.5a Real-space multiple scattering calculation

Multiple scattering calculation was originally developed for near-edge structure interpretation in X-ray absorption spectroscopy (XANES), and is also applicable to the ELNES since the theory of ELNES and XANES are exactly analogous. As illustrated in Figure 1-8, an excited electron (photoelectron in the case of x-ray excitation) is emitted from the central atom in a cluster, as a spherical wave. This wave is reflected off from surrounding atoms, and interferes with the outgoing wave, constructively or destructively depending on the phase difference, to yield an interference pattern that maps the

unoccupied density of states. Since it is based on a real-space cluster of atoms and there is no symmetry requirement for the calculation, the effects of dopant atoms on ELNES can be simply investigated by substituting atom types within the cluster. Most important, by doing a calculation on sequential clusters of defined size, the structural origins of particular features in the spectrum may be determined. Multiple scattering calculation therefore allows spectral changes to be directly interpreted in terms of structural changes.

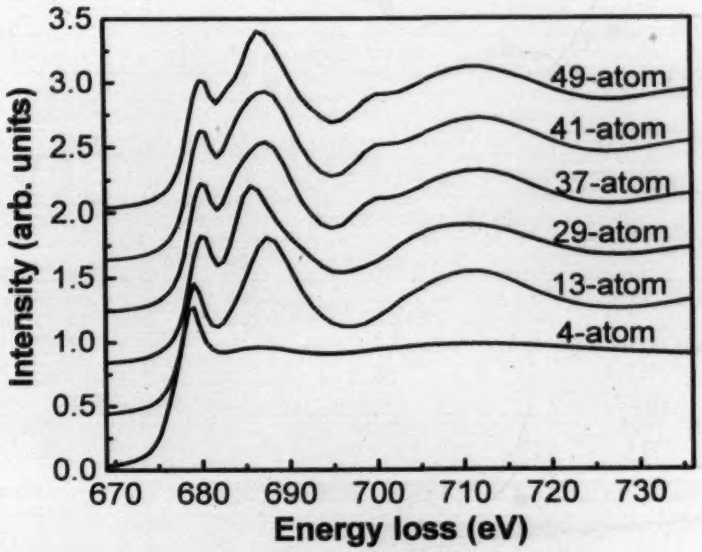

Figure 1-9 A sequential cluster calculations for F-K of FeF_2.

1.3.5b FEFF program

FEFF8 is a set of codes implemented in an *ab initio* program that is based on a self-consistent real-space multiple scattering calculations (RSMS) carried out on a finite cluster of atoms.[15] It is a real-space Green's function method, in which the sum over final states (in Eq. 1.4) is carried out implicitly in terms of the photoelectron Green's function or propagator ***G***. The *Hedin-Lundqvist (HL) self-energy*, an extension from ground state *density function theory* to excited state, is generally used to account for the many body effects and inelastic losses in solids. The general theoretical discussion and practical aspects on ELNES calculations using FEFF8 was recently reviewed by Moreno et al..[41]

RSMS (in FEFF8) is an excited-state electronic structure calculation based on the *final-state rule*, in which the final states are calculated in the presence of an appropriately

screened core-hole, and the many-body effects and inelastic losses are represented by a complex energy-dependent "self-energy" ΣE. The real part of ΣE leads to systemic shifts of edge threshold, and the imaginary part leads to the broadening of the spectrum ($\lambda(E) \sim k/(|Im\Sigma E| + \Gamma/2$, where Γ is the inverse of core-hole lifetime).[42] Hedin-Lundqvist (H-L) self-energy is based on uniform *electron-gas theory* and was first introduced into the x-ray absorption theory by Lee and Beni.[43] A complex potential is constructed to account for the electron-electron interaction including exchange and correlation effects, and added to the electrostatic potential to calculate the complex phase shifts. (H-L) self-energy is used in FEFF calculations for solids.

One example of using the code (FEFF 8.20), in a sequential cluster calculation of F-K in FeF_2, is shown in Figure 1-9. The spectral features can be correlated to their structural origins directly by these sequential calculations.

1.3.5c Prepeak and postpeak in iron nanoparticles

According to the *multiple scattering calculation* (in *Chapters 3 and 5*), a prepeak in O-K or F-K in transition metal oxides or fluorides appears immediately with a small cluster: central atoms (F or O) plus the first shell of the TM atoms, such as the F-K in FeF_2 in Figure 1-9; we also found that a prominent postpeak occurs at about 40 eV beyond the iron L_3 edge, coming from the backscattering of 1st shell oxygen atoms (discussed in *Chapter 3*). Through multiple scattering, we can correlate the prepeak in O-K or postpeak in TM-L edges to the TM metal oxides explicitly. Therefore we can use the technique to check the oxidation of the TMs, besides the traditional methods, such as x-ray or electron diffraction patterns. For example, to check the interface oxidation of Fe nanoparticles in SiO_2 matrix, one can check the postpeak in Fe-L, or the prepeak in O-K edge by focusing the electron beam on the edge of the nanoparticles (by using a STEM-EELS technique). Especially, both peaks are very localized and sensitive to the oxidation of the TM metals, according to the multiple scattering calculations. The application of the two techniques in the case of the iron nanoparticles embedded in SiO_2 matrix can be found in *Chapter 5*.

1.3.6 3d occupancy and white lines of iron

Fabrication and characterization of the iron nanoparticles is one of the main subjects of the thesis. Iron has atomic number Z=26, with the electronic configuration $3d^7 4s^1$, as shown in Figure 1-10. Transitions between 2p to 3d are allowed by the dipole selection rule ($\Delta l = \pm 1$). If the spin orbit effect is accounted, the 2p energy level is split into $2p_{1/2}$ ($j = 1/2$) and $2p_{3/2}$($j = 3/2$), and the 3d level is split into $3d_{3/2}$($j = 3/2$), $3d_{5/3}$($j = 5/2$). According to the dipole rule $\Delta j = 0, \pm 1$, we have the possible transitions: from $2p_{3/2}$ to $3d_{3/2}$ and $3d_{5/3}$ corresponding to L3 edge, and from $2p_{1/2}$ to $3d_{3/2}$ corresponding to L2 edge. Also there is a non-dipole transition 2s to 3d corresponding to the L1 edge, which is very weak and not observable mostly. There is yet another dipole-allowed transition: 2p to 4s, however the transition rate is 100 time lower than for the transition from 2p to 3d, resulting from the fact that the spatial overlap between 2p and 4s orbitals is very small, as the 2p orbital has a node at the center as opposed to the 4s orbital which has a maximum.

Therefore, the L_2 and L_3 edges correspond to excitations of 2p electrons to bound 3d states near the Fermi level (white lines), and to continuum states above the Fermi level. The energy separation of the L_2 and L_3 components arises from spin-orbit splitting. The intensity ratio for bulk metals is found to deviate from the statistical value WLR = 2, based on the relative occupancy of the initial-state levels. Much work has been done to relate the variation in *white-line intensity ratios* to the occupancies of 3d levels and to local magnetic moment.[17,44,45,46] Pease et al. demonstrated that there is linear relationship between WLR and the local magnetic moment for various transition metals and their oxides.[17] We have used a standard fitting procedure to measure the ratios of white-line intensity and white line widths in a well-defined way, as discussed in *Chapter 2*.

1.4 Outline of the thesis

The experimental observation and interpretation of the ELNES by multiple scattering calculations is the main subject, by which new methods were developed for ELNES characterization. Nanofabrication, such as fabrication of iron nanoparticles, silicon oxide nanowires is another important part in my thesis research; the electronic and geometrical

structures of those nanostructures were studied using the developed ELNES techniques. Six chapters (*Chapter 2, 3, 4, 5, 6 and 7*) within this thesis discuss the individual aspects of this work. Each of the above six chapters corresponds either to a journal publication or to a manuscript submitted for publication. General discussion and conclusion is given in *Chapter 8*. Below are the main issues dealt with in each chapter.

Chapter 2: Energy-loss near edge fine structures of iron nanoparticles. F. Wang, M. Malac and R.F. Egerton. Micron 37 (2006) 316-23.

- In-situ fabrication of iron nanoparticles by electron-beam-induced decomposition of iron fluorides
- Quantification of the white line ratio
- Dynamic monitor of the valence state of iron during irradiation
- Microstructure and magnetic properties of the iron nanoparticles of different sizes

Chapter 3: Interpretation of the postpeak in iron fluorides and oxides. F. Wang, R.F. Egerton and M. Malac. Ultramicroscopy 106 (2006) 925-932.

- Experimental observations of the postpeak in iron oxides and fluorides
- Multiple scattering calculations on iron L-edges in reproducing the postpeaks
- Interpretation of the postpeak, in terms of strong backscattering from the oxygen or fluorine atoms
- Discussion on its application in identifying the oxidation state of transition metals

Chapter 4: Multilayer route to iron nanoparticle formation in an insulating matrix. F. Wang, M. Malac, R. F. Egerton, A. Meldrum, X. Zhu, Z. Liu, N. Macdonald, P. Li and M.R. Freeman. J. Appl. Phys. (accepted)

- Fabrication of iron nanoparticles embedded in SiO_2 matrix through the multilayer-and-annealing route
- Oxidation state of iron nanoparticles by ELNES techniques
- Magnetization properties of the iron nanoparticles by MOKE measurement

Chapter 5: Alternative methods of identifying the oxidation of metallic nanoparticles embedded in a matrix. F. Wang, M. Malac, R.F. Egerton. Micron (in press)

- Correlating the prepeak in O-K and pospteak above L-edge to transition metal in an oxidation state, by multiple scattering calculation
- Application of the white line ratio, prepeak and postpeak techniques in identifying the oxidation state of iron nanoparticles embedded in the SiO_2 matrix
- Discussion on the advantages of the combined techniques in identifying the valence state of metallic nanoparticles in a matrix, and the compatibility with a STEM-EELS at high spatial resolution

Chapter 6: Controlled growth of silicon oxide nanowires from a patterned reagent. F. Wang, M. Malac, R.F. Egerton, A. Meldrum, P. Li, M.R. Freeman and J.G.C. Veinot. J. Phys. Chem. (accepted).

- The process of growing silicon oxide nanowires from patterned reagent.
- Microstrctures, morphology of silicon oxide nanowires, studied in an analytical TEM.
- Nanowire growth mechanism, a discussion.

Chapter 7: An ELNES study of SiO_2 nanowires grown from a patterned reagent. F. Wang, M. Malac, R.F. Egerton, P. Li, A. Meldrum and M.R. Freeman. Microscopy and Microanalysis 12 supplement 2 (2006) 1172 CD.

- Multiple scattering calculations on the oxygen K-edge in SiOx
- Oxidation state of the catalyst iron nanoparticles entrapped in the nanowire tips
- Study of the phase state of silicon by multiple scattering calçulation

Chapter 8: General discussion and conclusion

Appendix

A: Procedures for in-situ annealing in UHV system

B: Growth process of iron nanoparticles in a silica matrix: a real time study by in-situ transmission electron microscopy

C: Local oxidation of single iron nanoparticles in a SiO_2 matrix

D: Magnetite nanoparticles

E: Exclusion of plural scattering

F: Terminology

References

[1] R.F. Egerton, Electron Energy-Loss Spectroscopy in the Electron Microscope, 2nd edition, Plenum Press, New York (1996).

[2] Y. Zhu, R.F. Egerton and M. Malac, Ultramicroscopy **87** (2001) 135.

[3] M Malac, PhD thesis, University of Alberta (2000).

[4] R.D. Leapman, editor, Towards Atomic Resolution Analysis, Ultramicroscopy 78 (1999) 1-4.

[5] N.D. Browning, M.F. Chisholm, S.J. Pennycook, Nature 336 (1993) 143.

[6] M. Varela, A.R. Lupini, H.M. Christen, A.Y. Borisevich, N. Dellby, O.J. Krivanek, P.D. Nellist, S.D. Findlay, M.P. Oxley, L.J. Allen, and S.J. Pennycook, Phys. Rev. Lett. **92** (2004) 095502.

[7] D.A. Muller, Y. Tzou, R. Raj, J. Silcox, Nature 366 (1993) 725.

[8] P.E. Batson, Nature 366 (1993) 727.

[9] T. Suenaga et al., Science **290** (2000) 2280

[10] A. Ziegler et al, Science **306** (2004) 1768.

[11] I. Arslan et al, Phys Rev Lett. **94** (2005) 25504.

[12] J. Bradley et al, Science **307** (2005) 244.

[13] C.C. Ahn, O.L. Krivanek, R.P. Brugner, M.M Disko, and P.R. Swann, EELS Atlas. ASU HREM facility and Gatan Inc. (1983).

[14] N.D. Browning, I. Arslan, R. Erni, J.C. Idrobo, Z. Ziegler, J. Bradley, Z. Dai, E.A. Stach, and A. Bleloch, Journal of Physics: conference series 26 (2006) 59.

[15] A.L. Ankudinov, B. Ravel, J.J. Rehr, and S.D. Conradson, Phys. Rev. B **58** (1998) 7565.

[16] Z.L.Wang, J. Bentley, and N.D.Evans. Micron **31** (2000) 355-362.

[17] D.M. Pease, A. Fasihuddin, M. Daniel, and J.I.Budnick. Ultramicroscopy **88** (2001) 1-16.

[18] C. Colliex, T. Manoubi, and C. Ortiz. Phys. Rev. B **44** (1991) 11402.

[19] F.M.F. de Groot, M. Grioni, J.C. Fuggle, J. Ghijsen, G.A. Sawatzky, and H. Petersen. Phys. Rev. B **40** (1989) 5715.

[20] Z.Y. Wu, S. Gota, M.Pollak, M. Gautier-Soyer, C.R. Ratoli. Phys. Rev. B **55** (1997) 2570.

[21] K.S. Buchanan. PhD Thesis: Ultrafast Magnetic Relaxation in Nanocomposite Materials. University of Alberta (2004).

[22] K. Kimoto, G. Kothleitner, W. Grogger, Y. Matsui, and F. Hofer. Micron **36** (2005) 185.

[23] K. Kimoto, K. Khizuka, T. Asaka, T. Nagai, and Y. Matsui. Micron **36** (2005) 465.

[24] R.F. Egerton. Microsc Microanal **12** (supp 2) (2006)102-103.

[25] M. Inokuti, Rev. Mod. Phys. 43 (1971) 297.

[26] D. Muller, D. singh, and J. Silcox, Phys. Rev. B **57** (1998) 8181.

[27] J.M. Auerhammer, and P. Rez. Phys. Rev. B **40** (1989) 2024.

[28] N. Jiang, and J.C. Spence. Phys. Rev. B **70** (2004) 014112.

[29] P.J.W. Weijs, M.T. Czyzzyk, J.F. van Acker, W. Speier, G. vander Laan, K.H.J. Buschow, G. Wiech, and C.J. Fuggle, Phys. Rev. B **41** (1990) 11899.

[30] C. Hebert. Micron **38** (2007) 12.

[31] A. Gloter, A. Douiri, M. Tence, and C. Colliex. Ultramicroscopy **96** (2003)385-400.

[32] R.F. Egerton, H. Qian, and M. Malac. Micron **37** (2006) 310.

[33] M.P. Oxley, E.C. Cosgriff, and L.J. Allen. Phys. Rev. Lett. **94** (2005) 203906.

[34] R.D. Leapman, P.L. Fejes, and J. Silcox. Phys. Rev. B **28** (1983) 2361.

[35] P. Schattschneider, C. Hebert, and B, Jouffrey. Ultramicroscopy **86** (2001) 343.

[36] Y. Zhu, A.R. Moodenbaugh, G. Schneider, G.W.Davenport, T. Vogt, Q. Li, G.Gu, D.A. Fischer, and J. Tafto. Phys. Rev. Lett., **88** (2002) 247002.

[37] N. Jiang, B. Jiang, J.C.H Spence, R.C.Yu, S.C. Li, and C.Q. Jin. Phys. Rev. B **66** (2002) 172502.

[38] M.S. Moreno, S. Lazar, H.W. Zandbergen, and R.F. Egerton. Phys. Rev. B **73** (2006) 73308.

[39] Y. Ding, and Z.L. Wang. J. Electron Microscopy 54 (2005) 287.

[40] P.A. Midgley. Ultramicroscopy **76** (1999) 91.

[41] M.S. Moreno, K. Jorissen, and J.J. Rehr. Micron **38** (2007) 1.

[42] J.J. Rehr and R.C. Albers Rev. Mod. Phys. 72 (2000) 621.

[43] P.A. Lee and G. Beni, Phys. Rev. B 15 (1977) 2862.

[44] T.I. Morrison, M.B.Brodsky, N.J. Zaluzec, and LR. Sill. Phys Rev. B **32** (1985)3107.

[45] J. Graetz, C.C. Ahn, H. Ouyang, P. Rez, and B. Fultz. Phys. Rev. B **69** (2004) 235103.

[46] J. Yuan, E. Gu, M. Gester, J.A.C. Bland, and L.M. Brown. J. Appl. Phys. 75 (1996) 6501.

Chapter 2 Energy-loss near-edge fine structures of iron nanoparticles

(Feng Wang, Marek Malac, and Ray F Egerton, Micron 37 (2006) 316)

2.1 Introduction

Monolayers of single-domain magnetic nanoparticles have been proposed as ultra-high-density magnetic recording media (Sun et.al., 2000). Each nanoparticle behaves as a single magnetic dipole, its orientation fluctuating in accordance with the size, temperature and magnetic anisotropy of the particle. A collection of single-domain interacting magnetic nanoparticles provides a model system for studying cooperative physical phenomena (Poddar et.al., 2002). The possible enhancement of local magnetic moment in nanoparticles, due to their limited size, is still a matter of open debate (Kodama, 1999). Nanoparticles, including iron, can occur in multiple crystal phases, resulting in large differences in the magnetic moment and crystalline anisotropy (Yushizaki et.al, 1990 and Biedermann et.al., 2001). Furthermore, the magnetic moment of a nanoparticle depends strongly on interaction and chemical reaction with the matrix or substrate (Yuan et.al., 1996).

Transmission electron microscopy (TEM) allows us to study many aspects of a complex system in the same instrument. Electron diffraction and electron energy-loss spectroscopy (EELS) permit determination of the crystal phase and local magnetic moment, while TEM imaging allows us to measure the size of the nanoparticles within the same microscopic area. Lorentz microscopy (LM) reveals magnetic contrast, indicative of collective behaviour.

2.2. Experiment

We fabricated iron nanoparticles (supported on 4-nm thick carbon film) by in-situ electron-induced decomposition of an iron fluoride (FeF_2) thin film. The initial FeF_2 films were deposited by thermal evaporation using the micrometallurgy technique (Egerton and Bennett, 1996), which provides films with a thickness gradient across the substrate, as illustrated in Figure 2-1. The films were deposited at 1×10^{-4} Pa or less at deposition rates approximately 1 Å/s. To reduce the presence of water in the film, the evaporation source was preheated for 3 hours at about 200°C, resulting in the removal of any iron hydrates $FeF_2 \cdot 4H_2O$ and $FeF_2 \cdot 8H_2O$ (Streblechenko and Scheinfein, 1998). The deposition rate and thickness were monitored *in-situ* by a quartz-crystal monitor; although the FeF_2 thickness was later verified by EELS measurements. Immediately after deposition, samples were transferred to the TEM, limiting their exposure to air to less than 10 minutes.

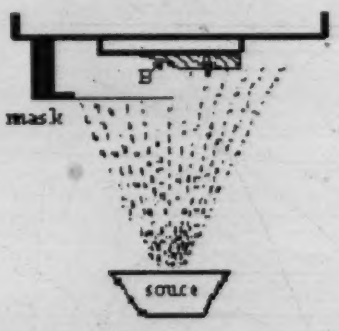

Figure 2-1 Illustration of the experimental setup for deposition of FeF_2 film: *Region (A)* is a region with uniform FeF_2 film; *Region (B)* is a transition region, in which the film thickness decreases gradually with distance from the masking edge.

The FeF_2 film was decomposed by 200 keV electron-beam irradiation with a current density j = 10 A/cm^2, the irradiated area being more than 1 micrometer in diameter. The size and overlap of the resulting iron nanoparticles, supported by the carbon substrate, depend on the thickness of the initial FeF_2 film. The evolution of the exposure process was studied by real-time TEM imaging and by electron energy-loss

spectroscopy (EELS), using a Gatan 666 spectrometer (Egerton et.al., 1993). The energy-loss spectra were collected in TEM diffraction mode (image-coupled spectrometer) with a collection semi-angle of 3.0 mrad. The dose rate j (about 10 Acm^{-2}) was determined from a TEM screen reading, calibrated using a Faraday cup and a Keithley 610 C pico-amperemeter. The samples were held at T = 400 K during irradiation in order to provide an adequate fluorine removal rate and to avoid buildup of carbonaceous contamination on the sample (Malac et.al., 2002).

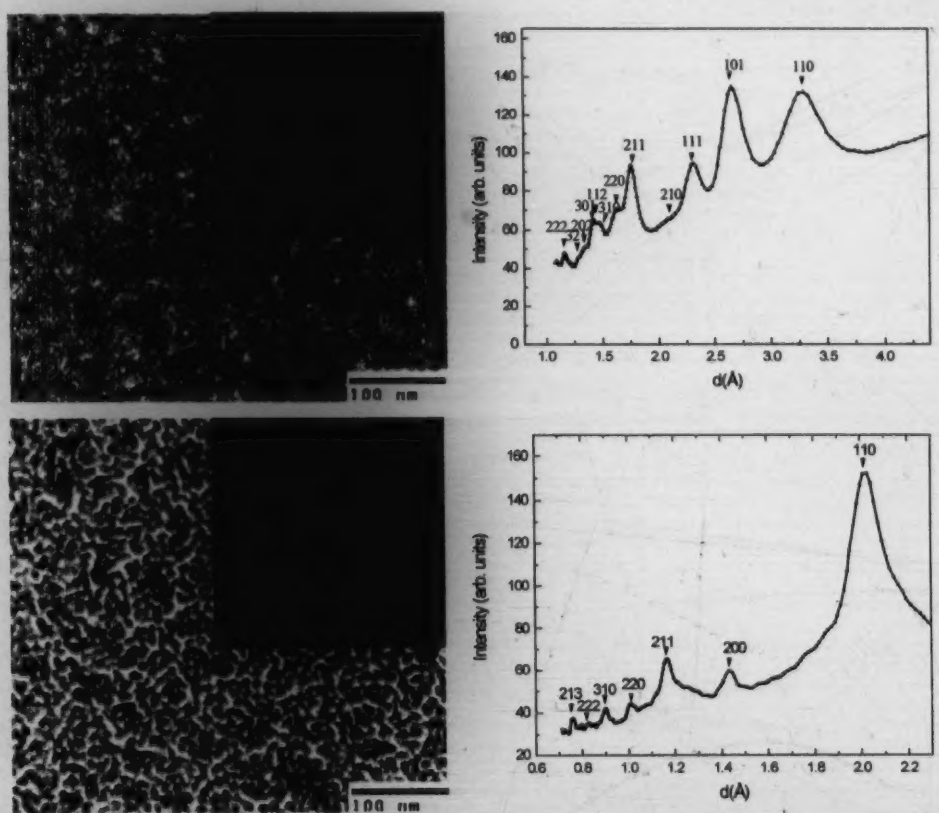

Figure 2-2 a) BF image with SAD pattern (inset, left) of FeF_2 before irradiation and corresponding profile of the SAD pattern (right), indexed according to a simple rutile structure (tetragonal, a=4.7 Å, c=3.3 Å). b) BF image with SAD pattern of FeF_2 (inset, left) after irradiation and corresponding profile of the SAD pattern (right), indexed according to Fe bcc structure (a=2.9 Å). No other phases can be detected.

We used the white-line ratio (WLR) of the iron L_{23} edge as a measure of local magnetic moment (Pease et.al, 2001), both during and after electron-induced decomposition. After subtraction of pre-edge background (Egerton, 1996), the WLR was obtained by fitting the L_3 and L_2 white-line peaks to two Lorentzians superimposed on

arctan functions to represent the final-state background (Morrison et.al., 1985). Lorentz microscopy was employed to observe magnetic contrast resulting from long-range magnetic alignment in the Fe-nanoparticle film. The objective lens was turned off for these measurements, leaving only a weak residual field that we measured as 1.05×10^{-2} Tesla.

2.3 Results and discussion

2.3.1 Decomposition of FeF_2

The initial FeF_2 film contained two distinct regions, schematically depicted in Figure 2-1. *Region (A)* consists of a uniform 10 nm thick FeF_2 film, whereas in *Region (B)* the film thickness drops gradually to zero at the edge of the out-of-contact mask. The width of *Region (B)* was controlled by adjusting the distance between the mask and the substrate.

As shown in Figure 2-2 (a), the initial FeF_2 film exhibits uniform nanocrystalline morphology, with a crystallite size of about 10 nm. All rings observed in the electron diffraction could be attributed to the FeF_2 rutile structure (tetragonal, a=4.7 Å, c=3.3Å) (Saifullah et.al., 1999). Following electron-beam exposure, the film in *Region (A)* was composed of large (~20 nm) particles, whose diffraction pattern, Fig. 2-2 (b), corresponds to body centered cubic (bcc) iron. No other phase was detected.

In *Region (B)*, six different sites were chosen, with thickness of the initial FeF_2 decreasing from 10 nm in Fig. 2-3 (a) to about 1nm in Fig. 2-3 (f). The effect of decreasing the initial FeF_2 thickness is clear from Figure 2-3: the size of the resulting iron particles decreases gradually from (a) to (f). Particle overlap can be observed in the area corresponding to the thickest initial film, Figs. 2-3(a) and 3(b), but does not appear in thinner areas, Figs. 2-3(c) to (f). As discussed for CoF_2 in Malac et.al. (2002), large fluoride-film thickness leads to increased frequency of particle overlap rather than to an increase in the particle size. But when the initial film is sufficiently thin, so that the iron nuclei forming by decomposition are well separated, the particle size decreases with decrease of the initial FeF_2 film thickness, as can be seen from Figs. 2-3(c) to (f).

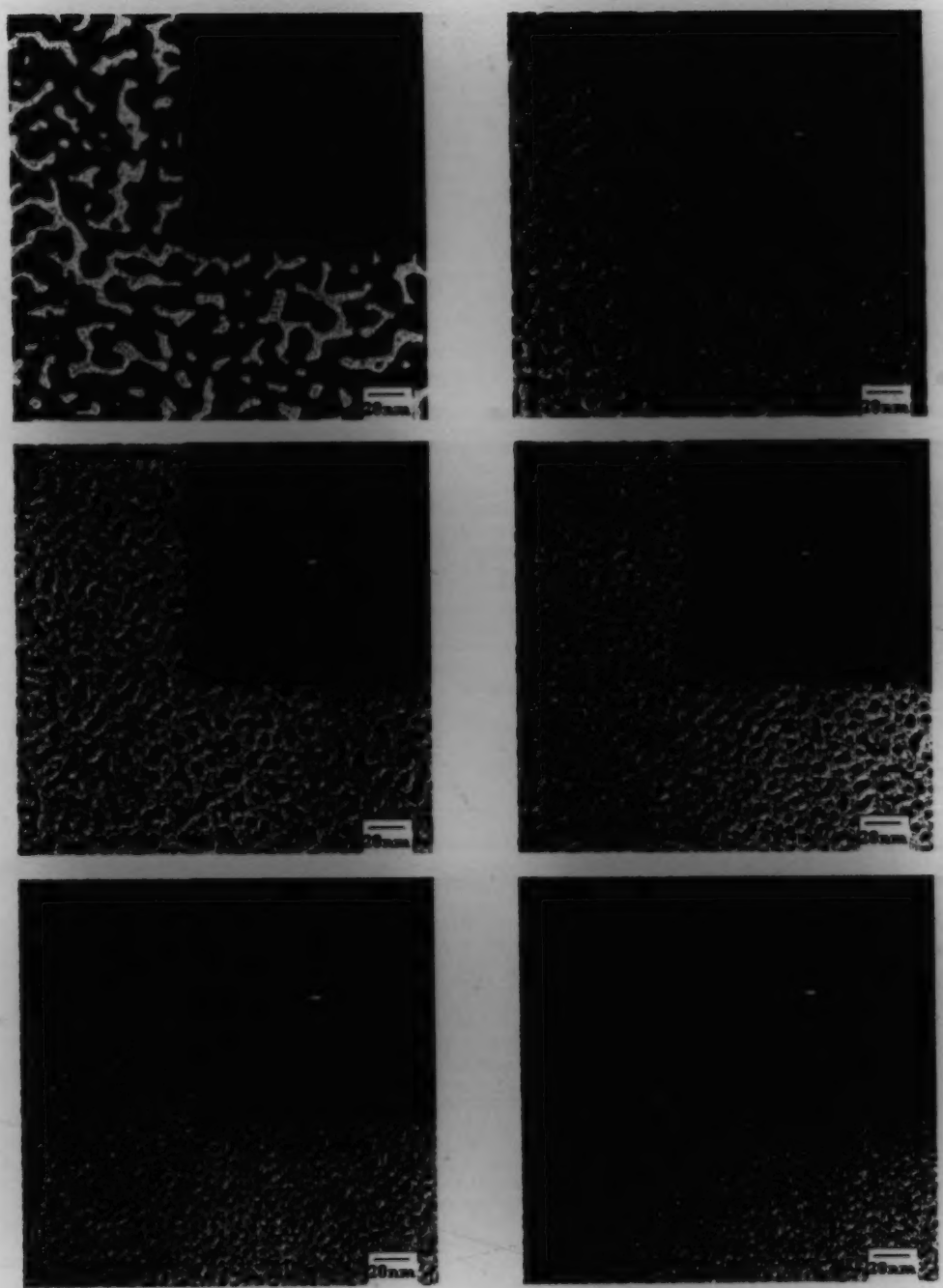

Figure 2-3 BF images and corresponding SAD patterns (inset) for iron nanoparticles of different sizes: a) 20 nm; b) 15 nm; c) 12 nm; d) 9 nm; e) 5 nm; f) 2 nm, corresponding to a thickness variation of the initial FeF_2 film from 10 nm to 1 nm.

The shape of the smallest iron nanoparticles, shown in Fig 2-3 (e) and (f), is spherical, but with increasing FeF_2 thickness the resulting particles become elliptic, with

faceting in Figs. 2-3(c) and (d), and some irregular-shaped linking observable in Figs. 2-3(a) and (b).

The growth of the iron nanoparticles is determined by their volume and by surface diffusion. Initially, iron nucleates at many sites forming small islands, whose shape is determined primarily by their surface energy, but these particles grow by Ostwald ripening (Granqvist and Buhman, 1976). The small spherical particles are formed only in the thin-FeF_2 region; due to limited iron mobility at T = 400 K, they remain at the position on the substrate at which they were formed (Malac et.al., 2002). In thicker FeF_2 regions, the Fe islands are larger, elliptical and exhibit faceting. Coalescence takes places in the thickest areas: smaller Fe islands move and coalesce with the larger ones, leading to the irregular shapes seen in Figs. 2-3(a) and (b) and an improvement in their crystallinity (Babonneau et.al., 2000).

The diffraction pattern for particles at site (a) of *Region (B)* is sharp and can be indexed as bcc-iron, as shown in Fig. 2-3(a), whereas the diffraction rings of smaller nanoparticles in Figs. 2-3 (b)-(f) are broad, as expected for nanometer-sized crystallites (Wang, 2000). Even for the small crystallites, the two strongest (albeit broad) diffraction rings match (110) and (211) reflections of the iron bcc structure. But due to larger widths of diffraction rings from the nanoparticles in Fig. 2-3. (b) - (f), we cannot exclude the possibility of a structural change. Such structural changes, for example from bcc to face centered cubic (fcc), have been described previously (Yushizaki et.al, 1990). Analysis of white-line ratios, which provides further circumstantial evidence of particle structure, is given in section **2.3.2** below.

Electron energy-loss spectroscopy (EELS) gives us further insight into the FeF_2 decomposition process. Figure 2-4 (a) shows energy-loss spectra of an initial FeF_2 for site (d), partially decomposed FeF_2 at an exposure dose $D = 400$ C/cm^2, and more fully exposed FeF_2 at a high exposure dose (D = 4500 C/cm^2). Fluorine K, iron L_{23}, and oxygen K ionization edges are visible in the FeF_2 spectrum, even for a sample already heated to 400 K. The oxygen is presumably due to water absorbed into the film during transfer to the microscope. As indicated by the O-K relative to the Fe-L_{23} edge, the amount of oxygen is small for thick region, such as in *Region (A)* and near the mask edge in *Region (B)*, but becomes large for thin regions, such as those at sites (d) - (f) in *Region*

(B). Fortunately, the oxygen can be removed by prolonged electron-beam exposure, as seen in Fig. 2-4 (a). It takes an electron dose of about D = 400 C/cm^2 to remove fluorine from the initial FeF_2 to below the detection limit, but more than 10 times higher dose D = 4500 C/cm^2 to remove oxygen from the same area.

We performed a detailed study on the iron white lines, in order to determine whether or not oxygen is chemically bound to iron. In particular, we were interested in the change of white line intensities for electron does D that caused complete fluorine removal (D > 400 C/cm^2). Figure 2-4 (b) shows that the Fe-L_3 intensity drops steadily for exposures up to 400 C/cm^2, the dose at which fluorine is removed from sample and iron nanoparticles are formed, after which the Fe-L_3 intensity remains constant up to the maximum electron dose (D = 4500 C/cm^2) used in our experiments. The L_2 intensity remains constant over the entire dose range, whereas oxygen is gradually removed within the dose range 400 C/cm^2 and 4500 C/cm^2, as observed by the decreasing intensity of O-K edge in Fig. 2-4 (a). These observations suggest that the chemical state of the iron changes during fluorine removal (doses up to 400 C/cm^2) but does not change as oxygen is being removed (doses above 400 C/cm^2). Quantitative discussion of the iron valence state will be made in the next section.

Our study of FeF_2 decomposition used large-area (diameter about 1 micrometer) exposure. In this situation, neither the diffusion of iron from outside of the exposed area nor electron proximity effects (Streblechenko and Scheinfein, 1998) are likely to play any significant role. To estimate the temperature increase due to this electron irradiation, we used a short computer program DORA.BAS (Egerton and Rauf, 1999) and found that it should be less than 100 °C for a dose rate of 10 A/cm^2. Therefore, our sample temperature (T < 500 K) remains much lower than the thermal-decomposition temperature of FeF_2, which is about 1400 K (Streblechenko and Scheinfei, 1998), indicating that the iron nanoparticles were obtained by electron-stimulated (rather than thermal) decomposition of FeF_2.

2.3.2 White lines

The white-line intensity ratio (WLR) is sensitive to change in the valence state and crystal structure of the transition metals and their oxides. It has been previously used to

study the variation of the local magnetic moment (Pease et.al., 2001 and Yuan et.al., 1996). The L_2 and L_3 edges (white lines) correspond to excitations of 2p electrons to bound 3d states near the Fermi level, and to continuum states above the Fermi level; energy separation of the L_2 and L_3 components arises from spin-orbit splitting. The intensity ratio for bulk metals is found to deviate from the statistical value WLR = 2, based on the relative occupancy of the initial-state levels (Egerton, 1996) except for Fe where WLR = 2:1 (Williams and Carter, 1996). Much work has been done to relate the variation in white-line intensity ratios to the occupancies of 3d levels and to local magnetic moment (Graetz et.al., 2004, Morrison et.al., 1985, Pease et.al., 2001,Yuan et.al., 1996). Pease et. al. (2001) demonstrated that there is linear relationship between WLR and the local magnetic moment for various transition metals and their oxides.

We have used a standard fitting procedure to measure the ratios of white-line intensity and white line widths in a well-defined way. First, multiple scattering was removed by Fourier-ratio deconvolution (Egerton, 1996). Then, the white-line component of the experimental data was fitted to (Pease et.al., 2001 and Colliex et.al., 1991):

$$I(E) = \alpha_2 L_2(E) + \alpha_3 L_3(E) + \beta_2 \sigma_2(E) + \beta_3 \sigma_3(E) \qquad (1)$$

where $L_2(E)$ and $L_3(E)$ represent the white-line profiles described by a Lorentzian:

$$L_i(E) = B_i \omega_i / [4(E-E_{i0})^2 + \omega_i^2] \qquad (2)$$

L_2 and L_3 respectively); $\sigma_2(E)$ and $\sigma_3(E)$ account for continuum background from the Here, E_{io} is the peak position, and ω_i is the lifetime broadening of the peak (i = 2 or 3 for core-to-continuum transition (Morrison et.al., 1985):

$$\sigma_i(E) = \sigma_i(E_{i0}) \{1/2 + (1/\pi)\arctan[(E-E_{i0})/\gamma_i/2]\} \qquad (3)$$

where E_{i0} is the continuum onset energy (the inflection point of the arctan curve), taken to be the same as the peak positions of $L_i(E)$; γ_i is the lifetime broadening for the core to continuum-state transitions. We assume $\sigma_2(E) = (1/2)\sigma_3(E)$ and $\gamma_2 = \gamma_3$ in our fitting procedure, as proposed by Morrison et.al. (1985). The purpose of this fitting procedure is to separate the white-line intensities from the continuum background. An additional constraint comes from the fact that L_2 width must exceed the L_3 width, owing to the possibility of Coster-Kronig transitions (Pease et al., 2001). The intensities of the white lines (Fe-L_2 and Fe-L_3) are taken as the integrated intensities under the fitted Lorentzians.

A typical fit of the experimental data shown in Figure 2-5(a) exhibits a good match to the experimental data.

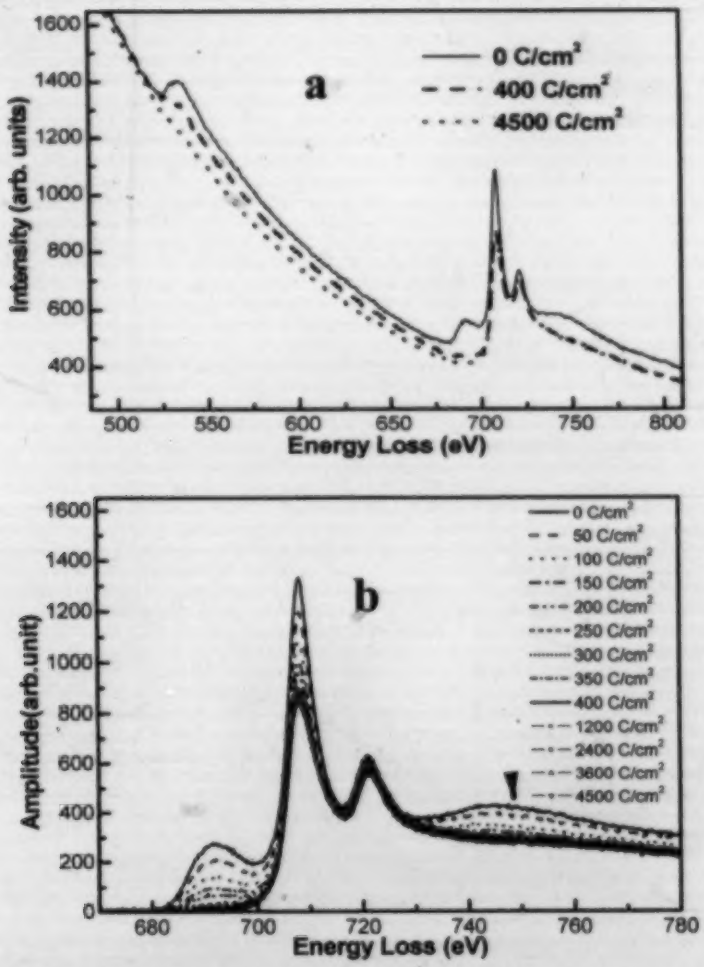

Figure 2-4 a) Typical O-K-, F-K- and Fe-L23- edges recorded at the start of electron exposure (represented by solid line), and after a dose of 400 C/cm^2 (dashed line) and 4500 C/cm^2 (dotted line) at site (d). The spectrum for 4500 C/cm^2 was rescaled to give it similar a Fe-L_2 intensity as that of the spectra for 0 C/cm^2 and 400 C/cm^2, which represent raw data from the spectrometer. b) Dose dependence of the F K-edge and Fe L-edges. The spectra for irradiation from 0 C/cm^2 to 400 C/cm^2 (represented by different line styles) are all raw data and have almost the same Fe L_2 intensity, while the spectra for irradiation of 1200 C/cm^2, 2400 C/cm^2, 3600 C/cm^2 and 4500 C/cm^2 (represented by solid line and different symbols) were rescaled to have the same Fe L_2 intensity as spectra representing 0 C/cm^2 to 400 C/cm^2.

The dependence of integrated white-line intensity ratio L_3/L_2 on irradiation dose D is shown *for region (A)* in Fig. 2-5 (b). WLR drops quickly as the dose increases from

zero to about 400 C/cm^2, corresponding to the removal of fluorine and a change from Fe^{2+} to Fe^0 oxidation state. The ratio remains constant at $L_3/L_2 \approx 2$ (the value for metallic bulk bcc iron) for doses above 400 C/cm^2. The lack of influence of oxygen removal on the L_3/L_2 ratio suggests that the oxygen is not chemically bonded to iron. WLR as a function of particle size for completely exposed Fe nanoparticles (D > 4500 C/cm^2) is also shown in Fig. 2-5 (b). For particles with sizes ranging from 2 nm to 20 nm, the white-line intensity ratio is $L_3/L_2 = 2.0 \pm 0.1$, the same as for bulk bcc iron. We believe that this invariance of the WLR is a genuine effect. Within experimental error (about 10 %, mostly due gain variation of spectrometer and spectra processing), there is no change in occupancy of the 3d levels with decrease in particle size down to 2 nm in diameter. Factors, which could change the d-band occupancy, such as structural change (from bcc to fcc), doping of the nanocrystals, their alloying and oxidation, can therefore be excluded.

2.3.3 Origin of the postpeak

A broad post-edge peak (postpeak) can be observed around 750 eV, about 40 eV above Fe L_3 edge. It is clearly visible in the as-prepared fluoride films, over the entire range of thickness studied in our work, and is marked by an arrow in Fig. 2-4 (b). This peak decays gradually with the decay of the F-K edge and completely disappears at D ≈ 400 C/cm^2.

In thicker samples, a broad peak following a core-loss edge is generally attributed to multiple scattering, involving a core loss and a bulk plasmon. However the total thickness of our sample is 14 nm or less (maximum 10 nm of FeF_2 film plus 4 nm of carbon substrate), so the probability of multiple scattering should be very low. As discussed above, 400 C/cm^2 is also the dose needed for fluorine removal, so it seems that the postpeak is associated with fluorination. Light atoms such as fluorine or oxygen should strongly scatter electrons near Fermi energy, and could therefore have could have a significant impact on the near-edge structure, according to multiple-scattering theory (Stern et.al., 1983).

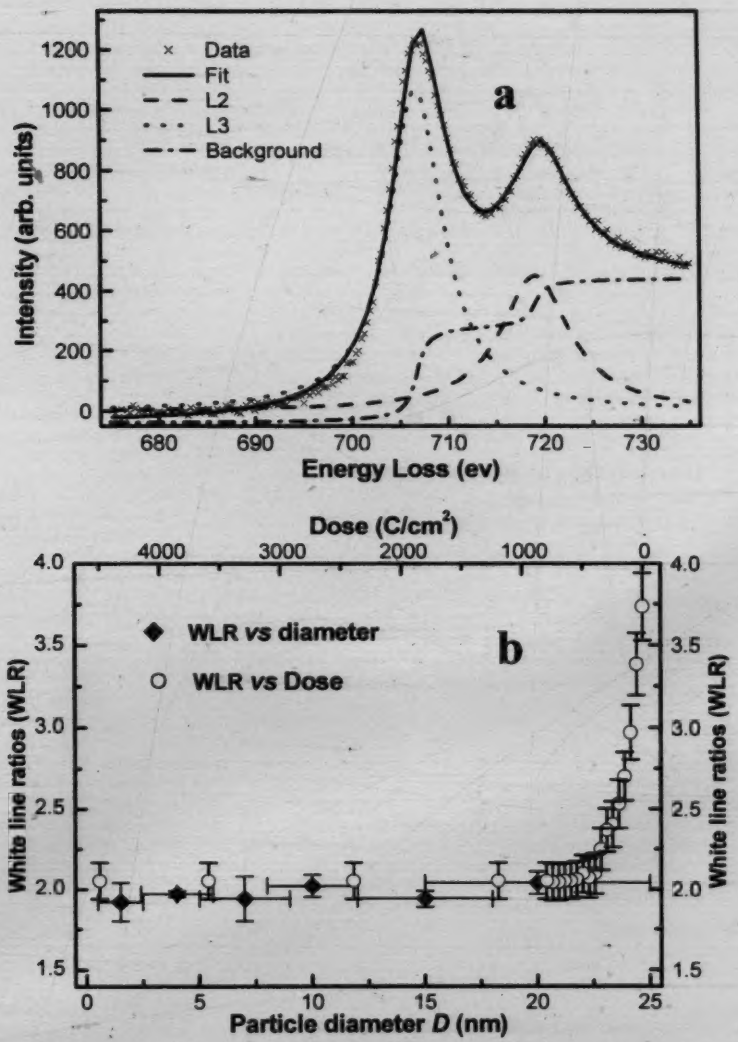

Figure 2-5 a) Typical curve-fitting result, in which crosses represent the experimental data; solid line is the fitted curve for the core-loss data; dashed line, dotted line and dash-dot line represent the L_2, L_3 and continuum background, respectively. b) Dependence of the white line ratio on the electron dose (diamonds) and on the size (circles) of the iron nanoparticles.

To confirm the above interpretation, we performed an oxidation experiment on a metallic iron film, produced by electron-beam evaporation of iron (purity: 99.95 %) in an ultra-high vacuum (UHV) system with initial pressure of 1×10^{-7} Pa. This 2 nm iron was deposited onto a 4 nm carbon film, with 4 nm and 8 nm SiO_2 as the buffer and capping layers. We confirmed the metallic characteristic of the iron by EELS, obtaining a white line ratio (WLR) of about 2.0 ± 1 according to the methods described above. After 30

days exposure to air, we checked the WLR again and found moderate oxidation in the film, as indicated by a white line ratio of about 3.1 ± 0.2. To further oxidize the film, we heated the sample in air and held it at 200 °C for 3 hours, after which the WLR increased to 4.2 ± 0.2 due to extensive oxidation. Figure 2-6 shows these experimental results; the spectra were rescaled to have similar Fe-L_2 intensities. No postpeak can be observed in the initial metallic iron film, a small bump is visible after air exposure for 30 days, and a large broad peak appeared at around 750 eV after heating in the air. Oxidation caused other changes in fine structures, such as a valley developed at about 730 eV.

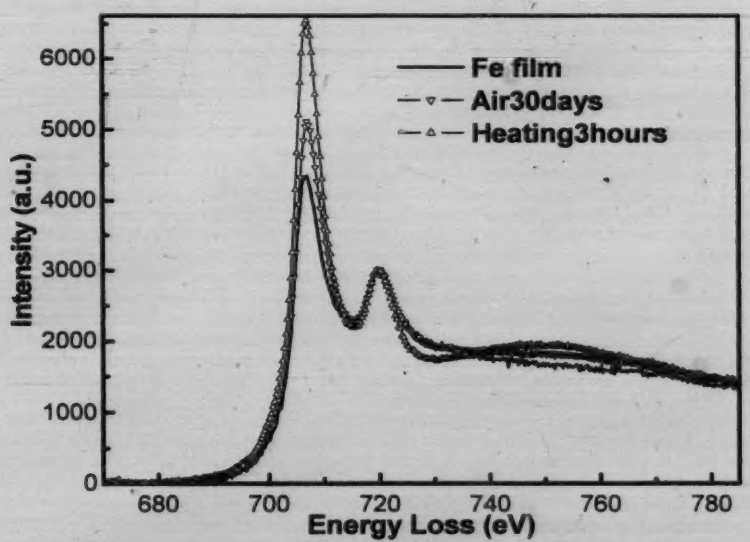

Figure 2-6 Experimental results for oxidization of iron films: no postpeak in metallic iron film with WLR=2.0 (solid line), small bump found in the film exposed to air for 30 days with WLR=3.1 (solid line, triangle down) and big broad peak in the film oxidized at 200 °C in air for 3 hours with WLR = 4.2 (solid line, triangle up). The spectra were rescaled to have similar Fe-L_2 intensities to show the different fine structures above the L_2 edge.

A similar postpeak is visible in the spectra of iron oxides published by Leapman et.al.(1982) and Colliex et.al. (1991). Its origin remains unexplained, as far as we know, but it appears to be characteristic of iron in an oxidized state. To further study its origin, we are performing multiple-scattering calculations of the near-edge structure of iron L edges, using the FEFF 8.2 code (Ankudinov et.al., 1998).

2.3.4 Collective behaviour

As discussed above, the L_3/L_2 ratio measured by EELS is an indication of the local magnetic moment within the specimen. However, a local technique such as EELS cannot address the question of whether the individual magnetic moments of the particles couple to each other over larger distances, and the spatial extension of such coupling. On the other hand, TEM Lorentz microscopy (LM) can be used to assess the magnetic microstructure of the film (De Graef, 2001). In particular, LM allows us to determine whether the particles are coupled ferromagnetically (i.e. magnetic moments aligned in the same direction over large areas) or whether each particle acts individually, possibly coupled only by dipole interactions.

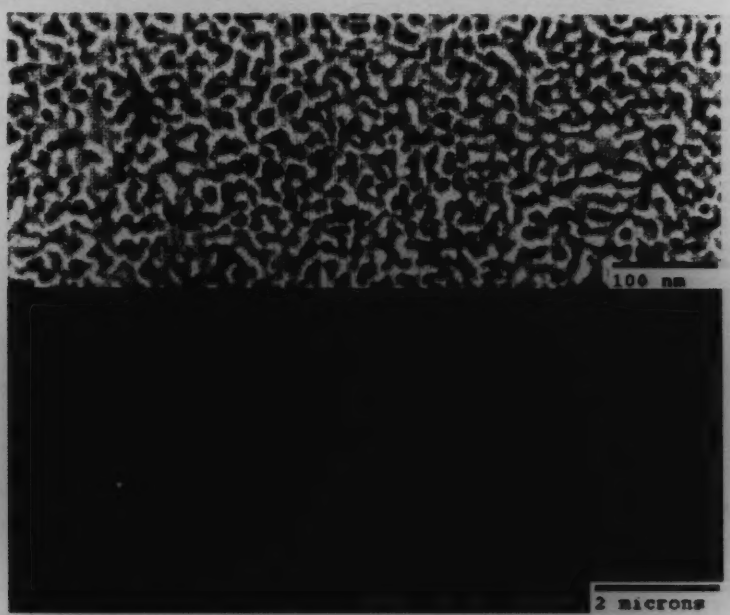

Figure 2-7 Bright-field image (top) and Lorentz images in underfocus, focus and overfocus modes (bottom) for the nanoparticles shown in Figure 2-3 (a).

We used Lorentz microscopy for in-situ observation of the magnetic contrast arising from our iron nanoparticles of different particle sizes and inter-particle distances, as shown in Fig. 2-3. Figure 2-7 shows bright field (BF) and LM images from thick part *Region (B)* (shown in Fig. 2-3(a)) where the surface coverage factor (i.e. fractional area covered by iron nanoparticles) is more than 90%. Magnetic ripple structure can be seen clearly in these overlapping particles, and shows contrast reversal in a through-focus series, as expected for magnetic contrast. This ripple contrast is an indication of long-

range ferromagnetic order in our film of densely packed nanoparticles. The behavior is similar to that of a continuous ferromagnetic thin film and comes as no surprise, in view of the strong exchange interaction between the overlapping nanoparticles.

Such collective behavior is not observed in the less dense areas in *Region B*, due to a decreased strength of magnetostatic interactions. Exchange interaction becomes weaker as the particles overlap less frequently, so eventually the long-range order will break down. Detailed magnetic contrast cannot be observed with our microscope setup, due to the limited spatial resolution with the objective lens off. Also, very small particles are likely to be superparamagnetic, as the critical diameter for iron is 10 nm at room temperature (Tofail et.al., 2001), and should exhibit no LM contrast.

2.4 Conclusions

Monolayers of metallic Fe nanoparticles with varying particle size and interparticle distance were prepared by in-situ electron-induced decomposition of FeF_2. Selected-area diffraction and EELS allowed us to study this decomposition process. L-edge white lines were used to identify the phase and structure of iron nanoparticles, and also as a probe of the local magnetic moment. We found no change of magnetic moment with varying particle size, from 2 nm to about 20 nm. On the other hand, we did observe collective magnetic behavior in densely packed iron nanoparticles.

A broad post-edge peak exists in iron fluorides and oxides but not in metallic iron. It may be a characteristic feature of iron compounds, that can be used as an additional check on the valence state of iron. We hope to gain insight into its origin by performing multiple-scattering calculations using the FEFF 8.2 code.

Acknowledgements

This work was supported by *NRC* and *NSERC*. The authors would like to thank M.R. Freeman and M.S. Moreno for helpful discussions, D. Mullin and G. Popowich for technical assistance. Feng Wang wishes to acknowledge support from Prof. Zhenghe Xu and the *Izaak Walton Killam Memorial Scholarship*.

References

Ankudinov, A.L., Ravel, B., Rehr, J.J. and Conradson, S.D., 1998. Real Space Multiple Scattering Calculation and Interpretation of X-ray Absorption Near Edge Structure. Phys. Rev. B 58, 7565-7576.

Babonneau, D., Naudon, A., Cabioch, T. and Lyon, O., 2000. Morphology of encapsulated iron nanoparticles obtained by co-sputtering and implantation: a GISAXS study. J. Appl. Cryst. 33, 437-441.

Biedermann, A., Schmid, M. and Varga, P., 2001. Nucleation of bcc iron in ultrathin fcc films. Phys. Rev. Lett. 86, 464-467.

Colliex, C., Manoubi,T. and Ortiz, C., 1991. Electron-energy-loss-spectroscopy near-edge fine structure in the iron-oxygen system. Phys. Rev. B 44,11402-11411.

De Graef, M., 2001. Chapter 2: Lorentz microscopy: theoretical basis and image simulations. In De Graef, M. Zhu, Y. (Eds.), Magnetic Imaging and its Applications to Materials. Experimental Methods in the Physical Sciences, vol. 36. Academic Press, New York, pp. 27-67.

Egerton, R.F., 1996. Electron Energy-Loss Spectroscopy in the Electron Microscopy, 2nd ed., New York: Plenum Press.

Egerton, R.F. and Bennett, J.C., 1996. Micrometallurgy: a technique for examining the structure of binary-element thin films over a wide range of composition. J. of Microscopy 183, 116-123.

Egerton, R.F. and Rauf, I., 1999. Dose-rate dependence of electron-induced mass loss from organic specimens. Ultramicroscopy 80, 247-254.

Egerton, R.F., Yang, Y.Y. and Cheng, S.C., 1993. Characterization and use of the Gatan 666 parallel-recording electron energy-loss spectrometer. Ultramicroscopy 48, 239- 250.

Graetz, J., Ahn, C.C., Ouyang, H., Rez, P. and Fultz, B., 2004. White lines and d-band occupancy for the 3d transition-metal oxides and lithium transition-metal oxides. Phys. Rev. B 69, 235103-1~5.

Granqvist, C. G. and Buhman, R., 1976. Ultrafine metal particles. J. Appl. Phys. 47, 2200-2219.

Kodama, R.H., 1999. Magnetic nanoparticles. J. Mag. Mag. Mater. 200, 359-372.

Leapman, R.D., Grunes, L.A. and Fejes, P.L., 1982. Study of the L23 edges in the 3d transition metals and their oxides by electron-energy-loss spectroscopy with comparisons to theory. Phys. Rev. B 26, 614-635.

Malac, M., Schoefield, M., Zhu, Y. and Egerton, R.F., 2002. Exposure characteristics of cobalt fluoride (CoF_2) self-developing electron-beam resist on sub- 100 nm scale. J. Appl. Phys. 92, 1112-1121.

Morrison, T.I., Brodsky, M.B., Zaluzec, N.J. and Sill, LR., 1985. Iron d-band occupancy in amorphous Fe_xGe_{1-x}. Phys Rev. B 32, 3107-3111.

Poddar, P., Telem-Shafir, T., Fried,T. and Markovich, G., 2002. Dipolar interactions in two- and three-dimensional magnetic nanoparticle arrays. Phys. Rev. B 66, 060403-1~4(R).

Pease, D.M. Fasihuddin, Daniel, A. M. and Budnick, J.I., 2001. Method of linearizing the 3d L_3/L_2 white line ratio as a function of magnetic moment. Ultramicroscopy 88, 1-16.

Saifullah, M. S. M., Botton, G. A., Boothroyd, C. B. and Humphreys, C. J., 1999. Electron energy loss spectroscopy studies of the amorphous to crystalline transition in FeF_3. J. Appl. Phys. 86, 2499-2504.

Stern, E.A., Heald, S.M., Koch, E.E., 1983. Handbook of Synchrotron Radiation. North-Holland, New York, 995-1014.

Streblechenko, D. and Scheinfein, M.R., 1998. Magnetic nanostructures produced by electron beam patterning of direct write transition metal fluoride resists. J.Vac. Sci. Technol. A 16, 1374-1379.

Sun, S., Murray, C. B., Weller, D., Folks, L. and Moser, A., 2000. Monodisperse FePt nanoparticles and ferromagnetic FePt nanocrystal superlattices. Science 287,1989-1992.

Tofail, S.A.M., Rahman, I.Z. and Rahman, M.A., 2001. Patterned Nanostructured Arrays for High-density Magnetic Recording. Appl. Organometal. Chem. 15, 373-382.

Wang, Z.L., 2000. Chapter 3: Transmission electron microscopy and spectroscopy of Nan particles. In Wang, Z.L. (Eds.), Characterization of Nanophase Materials. Wiley-VCH; 1st edition, PP. 61-70.

Williams, D.B. and Carter, C.B. 1996. Transmission Electron Microscopy: A Textbook formaterials Science. New York: Plenum Press 691.

Yuan, J., Gu, E. Gester, M. Bland, J.A.C. and Brown, L.M., 1996. Electron-energy-loss spectroscopy of Fe thin films on GaAs(001). J. Appl. Phys. 75, 6501-6503.

Yushizaki, F., Tanaka, N. and Mihama, K., 1990. Growth of γ-iron crystallites in MgO films and the magnetic properties. J. Electron Microsc. 39, 459-464.

Chapter 3 Interpretation of the postpeak in iron fluorides and oxides

(Feng Wang, Ray F Egerton, and Marek Malac Ultramicroscopy 106 (2006) 925)

3.1 Introduction

Because of the potential applications, there is renewed interest in the development of synthesis and characterization techniques for nanoparticles and nano-scale sandwich structures [1,2]. One potential problem with nanoparticles is their tendency to oxidize by reacting with the environment, due to their large surface/volume ratio. Electron energy-loss near-edge structure (ELNES) is the electron-beam counterpart of x-ray absorption near-edge structure (XANES) and is well suited to the characterization of nano-structures, since its interpretation requires no assumption of symmetry or periodicity [3]. In addition, ELNES in transmission electron microscope (TEM) offers the advantage (over XANES) of high spatial resolution, allowing it to be used for the in-situ characterization of the chemical state within a high-resolution TEM [4].

During experiments on *in-situ* fabrication of iron nanoparticles by electron-beam-induced decomposition of iron fluoride (FeF_2) films, we observed a broad but prominent peak about 40 eV above the Fe-L_3 ionization threshold in FeF_2. This postpeak disappeared when the film was converted to metallic iron but reappeared when the iron was oxidized. In the case of thicker samples, a broad peak following a core-loss edge is attributed to plural scattering, involving a core loss and a bulk plasmon, and can be removed by deconvolution techniques. However, such an explanation does not apply to our observations, since film thickness is less than 0.1 mean free path and therefore too thin to scatter electrons more than once.

A similar postpeak is visible in the spectra of iron oxides published by Leapman et.al. [5] and Colliex et.al. [6], but is plainly absent in the spectrum of pure iron [5], in agreement with our own observations. This broad peak appears also in other transition-metal oxides but not in the metals [5, 7]; in our previously reported data [8], a prominent

postpeak is apparent in the near-edge structure of Co-L edge in CoF_2 but disappears with the removal of fluorine under electron irradiation.

In this article, we show that this variation of the postpeak is associated with change of the chemical state of iron. The absence of a postpeak in α-Fe and the presence and distinctive features of the postpeak in FeF_2 and α-Fe_2O_3 can be reproduced by multiple-scattering* calculations of the fine structure for the iron L-edge, using FEFF 8.2 code [12]. Calculations as a function of cluster size allow us to attribute the postpeak in FeF_2 and α-Fe_2O_3 to the backscattering of fluorine and oxygen atoms, respectively. Extension of the conclusion to other transition metals is also discussed.

Table 3-1: Radii and occupancy of the first five shells surrounding the central iron atom in α-Fe, FeF_2 and α-Fe_2O_3.

	Shell	Element	Radius (Å)	Atom number
α-Fe	1	Fe	2.48549	8
	2	Fe	2.87000	6
	3	Fe	4.05879	12
	4	Fe	4.75936	24
	5	Fe	4.97099	8
FeF_2	1	F	1.99260	2
	2	F	2.12183	4
	3	Fe	3.30910	2
	4	F	3.57682	4
	5	Fe	3.71033	8
α-Fe_2O_3	1	O	1.94567	3
	2	O	2.11616	3
	3	Fe	2.90038	4
	4	Fe	3.36416	3
	5	O	3.39850	3

3.2 Experimental Methods

The experimental procedure for preparation of iron nanoparticles by electron-beam decomposition of iron fluoride (FeF_2) is reported in [4]†. Briefly: films of FeF_2 were deposited onto a 4 nm-thick carbon film by thermal evaporation in high vacuum. An out-of-contact masking technique was used to produce a thickness gradient within the film (continuous change from 1 nm to 10 nm), resulting in iron nanoparticles of different sizes following the electron exposure. Immediately after FeF_2 deposition, samples were transferred to a TEM (JEOL 2010), limiting their air exposure to less than 10 minutes.

* Here multiple-scattering means the scattering of the excited electrons.

The FeF_2 film was irradiated with 200 keV electrons at a current density j = 10 A/cm^2 and a specimen temperature T = 400 K. The exposure process was monitored by real-time TEM imaging and by electron energy-loss spectroscopy (EELS), using a Gatan 666 spectrometer. The energy-loss spectra were collected in TEM diffraction mode (image-coupled spectrometer) with a collection semi-angle of 3.0 mrad.

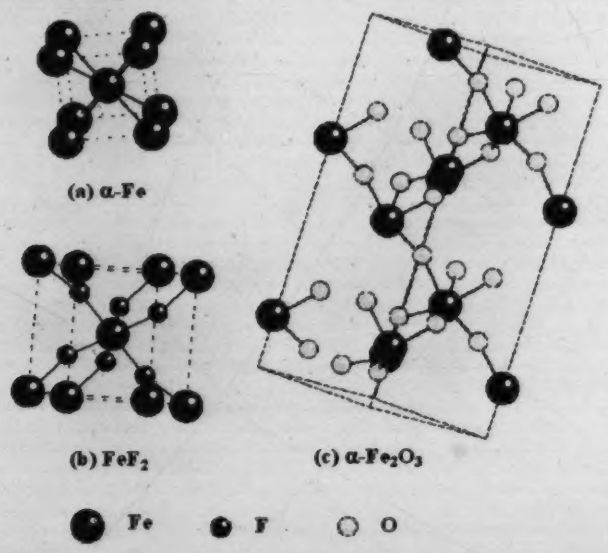

Figure 3-1 Unit cells for α-Fe, FeF_2 and α-Fe_2O_3 reproduced from Crystal Kit software. (a) Crystal structure of α-Fe (body centered cubic structure), each iron atom being coordinated by another 8 iron atoms. (b) Crystal structure of FeF_2 (tetragonal rutile structure): Fe atoms are on a body-centered tetragonal lattice, each iron atom being coordinated by six fluorine atoms with two short and four long Fe-F bonds. (c) Crystal structure of α-Fe_2O_3, showing hexagonal unit cell: there are two kinds of Fe-atom pairs, one with a short and one with a larger Fe-Fe distance; the O atoms form close-packed basal planes, each Fe atom being coordinated octahedrally by six O atoms.

Metallic Fe films were produced by electron-beam evaporation of iron (purity 99.95%) in an ultra-high vacuum (UHV) system with base pressure of 1×10^{-8} Pa. More specifically, 3nm-thick iron films were deposited onto 5nm-thick carbon, buffered and capped with 4nm-thick SiO_2 layers for a temporary protection from oxidation. The total sample thickness (including iron film, carbon film substrate and SiO_2 capping layer) does not exceed 16 nm. The metallic iron samples were annealed above 170°C in an oven, resulting in moderate oxidization and presence of the FeO phase; further oxidization of

† Please refer to the Experiment section in Chapter 2.

the samples was made by annealing in air above 600°C and 720°C, to obtain the Fe_3O_4 and α-Fe_2O_3 phases respectively. The presence of different oxides of iron was determined by selected area diffraction (SAD) and core-loss EELS in the TEM.

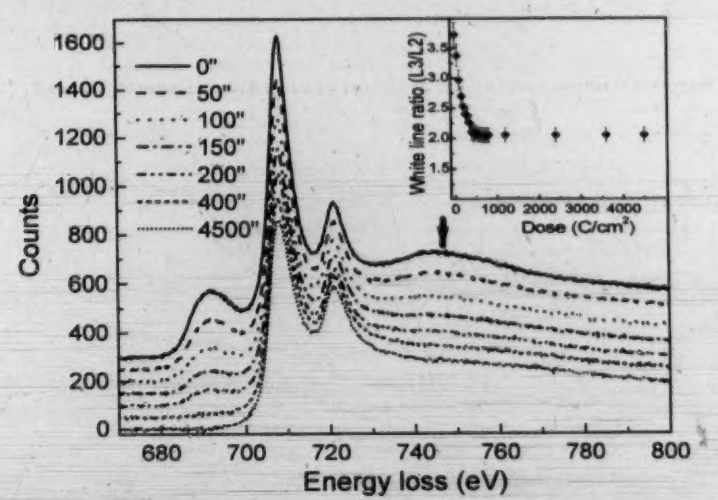

Figure 3-2 Dose dependence of the Fe-L_{23} and F K-edges. The spectra (represented by different line styles) were recorded after irradiation with electron doses up to 4500 C/cm^2. The inset shows the dependence of white-line ratio on electron dose.

Real-space multiple-scattering (RSMS) calculations of the iron L-edge near-edge structure were performed for α-Fe, FeF_2 and iron oxides using the FEFF 8.2 code with its implemented full multiple scattering (FMS) and self-consistent field (SCF) cards [12]. We used the Hedin-Lundqvist self-energy to calculate inelastic mean free path of the ejected core electron in these FEFF calculations. A sequence of near-edge structure calculations of the L_3 edge was made by adding successive shells about the central excited Fe atom, in order to ascertain the contributions from different shells. Near-edge structure calculation of L_2 edge was also made in considering its contribution to the postpeak. For the "bulk" calculations, we used cluster sizes of 169, 177 and 171 atoms for α-Fe, FeF_2 and α-Fe_2O_3 respectively. Energy shifts of 3 eV, 1 eV and 2 eV were added to match the experimental thresholds of iron Fe-L_3 edges of α-Fe, FeF_2 and α-Fe_2O_3 respectively.‡ In all the calculations, 1eV Gaussian broadening was applied to

‡ The Fermi level is determined by *self-consistent field* calculation of the potentials. The discrepancy of the FEFF calculation with experiments, mainly because the *muffin-tin model* is used.

account for our experimental energy resolution. RSMS calculations were also made for intermediate iron oxides, i.e. FeO and Fe_3O_4, but are not reported here.

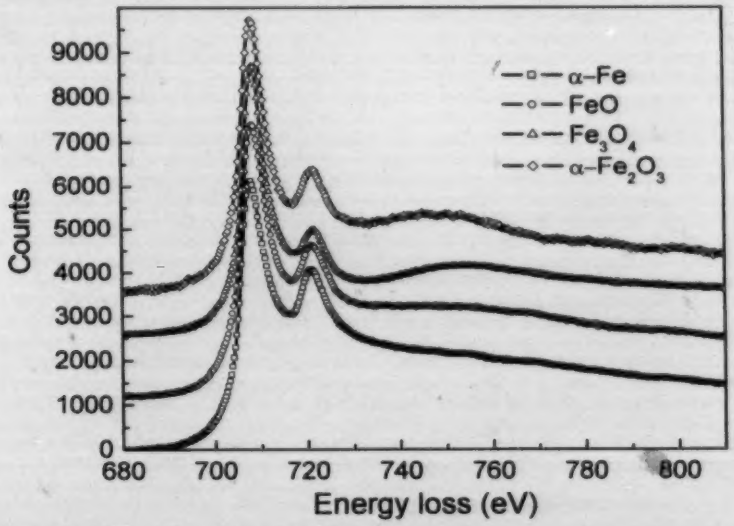

Figure 3-3 Experimental ELNES of iron and iron oxides: a solid line with hollow squares is for metallic iron, a solid line with hollow circles for FeO, a solid line with hollow triangles for Fe_3O_4 and a solid line with hollow diamonds for α-Fe_2O_3.

3.3 Results

The electron energy-loss near-edge structure (ELNES) is a mirror of the electronic structure of the specimen and is closely related to crystal structure in the multiple scattering regime [9]. Therefore we must consider the relevant crystal structures in order to interpret the postpeak. α-Fe has a relatively open body-centered cubic (bcc) structure shown in Figure 3-1 (a). FeF_2 has a tetragonal rutile structure with space group P42/mnm, the Fe atoms occur on a body-centered tetragonal lattice with the D_{2h} symmetry, as shown in Figure 3-1 (b); they are coordinated by six fluorine atoms with two short ($d_{Fe\text{-}F}$ = 1.9926 Å) and four long ($d_{Fe\text{-}F}$ = 2.1218 Å) Fe-F bonds [10]. The crystal structure of the thermodynamically stable iron oxide α-Fe_2O_3 is rhombohedral (with space group R-3C) and consists of hexagonal closed-packed (001) layers of oxygen atoms with two thirds of the octahedral holes filled by Fe atoms, as shown in Figure 3-1(c). There are six formula units in the conventional hexagonal unit cell, combining to yield the uniaxial corundum structure in which each iron atom is coordinated by six oxygen atoms. There is a slight deviation from octahedral symmetry, with three short ($d_{Fe\text{-}O}$ = 1.9436 Å) and three long

(d_{Fe-O} = 2.1162 Å) Fe-O bonds [11]. The atomic distributions around a central Fe atom within the first five shells are listed in Table 1, including the radii of the coordination shells, the atomic species and atom numbers of the first five shells.

Besides the fluorine K- and iron L-edges, a broad post-edge peak (postpeak) can be observed around 746 eV in the energy-loss spectrum of the as-prepared fluoride films, as marked by an arrow in Figure 3-2. This peak is visible over the entire range of film thickness studied in our work. The postpeak decays gradually with decay of the F-K edge and has completely disappeared at an electron irradiation dose D = 400 C/cm^2, which causes fluorine to be removed from the sample, leaving behind metallic iron nanoparticles. In addition, the Fe-L_3 intensity drops steadily while Fe-L_2 remains almost constant for exposures up to 400 C/cm^2. Thereafter, the Fe-L_3 intensity remains constant up to the maximum electron dose (D = 4500 C/cm^2) used in our experiments.

It is known that the white-line ratio (integral intensity ratio L_3/L_2) is sensitive to the change in the valence state of transition metals and their oxides [13]. We used a standard procedure to quantify the white-line peaks, fitting them to a combination of Lorentzian and arctangent functions [4]. In this way, the white-line ratio (WLR) of Fe-L_{23} was obtained to identify the variation in the valence state of iron; the inset of Fig. 3-2 shows the dependence of WLR on electron dose. The ratio drops quickly as the dose increases from 0 to 400 C/cm^2 but stays constant at L_3/L_2 = 2.0 ± 0.1 up to 4500 C/cm^2, suggesting that the chemical state of the iron changes from Fe^{2+} to Fe^0 during fluorine removal (doses up to 400 C/cm^2) and then remains unaltered. The plural scattering contribution to the postpeak is negligible according to the Appendix E.

Figure 3-3 shows the near-edge structures of the iron-L edges, for the α-Fe, FeO, Fe_3O_4 and α-Fe_2O_3 films that were grown in UHV and after-growth oxidization. No postpeak can be observed in the metallic iron film, a small bump is visible in FeO, and large broad peaks appeared at around 751 eV in Fe_3O_4, and 748 eV in α-Fe_2O_3. The oxidation phases were checked with SAD and were found to be consistent with the white line ratios obtained from the core-loss EELS. Metallic iron (pure α-Fe phase) has a white line ratio (WLR) of L_3/L_2 = 2.1 ± 0.2; the WLR for FeO, Fe_3O_4 and α-Fe_2O_3 are 3.2 ± 0.3, 3.6 ± 0.2 and 4.8 ± 0.2 respectively.

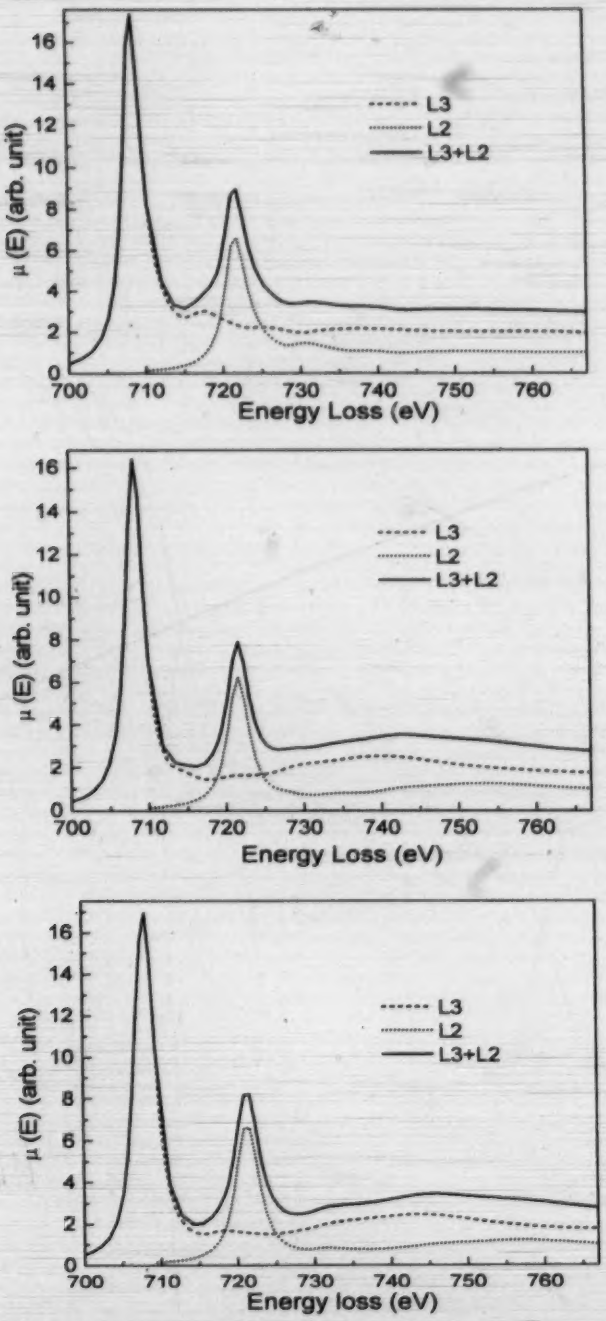

Figure 3-4 Multiple-scattering calculation of the cross-sections for Fe-L edges of (a) α-Fe, (b) FeF_2 and (c) α-Fe_2O_3. The dashed lines are cross-sections for iron L_3, dotted lines for L_2, and the solid line the sum of L_3 and L_2.

Figure 3-4 shows the results of RSMS calculations of the core-loss cross-section μ(E) for Fe L-edge structures of α-Fe, FeF_2 and α-Fe_2O_3. The dashed lines are μ(E) of

Fe-L_3, dotted lines are $\mu(E)$ for Fe-L_2, and the solid lines represent summed $\mu(E)$ for L_3 and L_2. Prominent postpeaks at around 744 eV for FeF_2 and 747 eV for α-Fe_2O_3 are visible, their energy positions being comparable with those found experimentally in Figs. 3-2 and 3-3. In agreement with our observations, the postpeak does not appear in the calculated cross-section of Fe-L_3 or Fe-L_2 for metallic iron, although there are some small oscillations in the post-edge region. RSMS calculations for FeO, Fe_3O_4 (not shown here) gave postpeaks that are consistent with our experiments.

Figure 3-5 shows a sequence of calculations of the Fe-L_3 cross-section $\mu(E)$ for α-Fe, FeF_2 and α-Fe_2O_3. These calculations were made in order to study the contributions from different elements, by adding successive coordination shells about the central Fe atom (in Table 1). The cross-sections for increasing cluster size are shown together with that for the bulk (with cluster sizes of 169, 177 and 171 atoms for α-Fe, FeF_2 and α-Fe_2O_3 respectively) in Fig. 3-5.

In Fig. 3-5 (a), the convergent calculations are shown for the near-edge structure above the Fe-L_3 edge. With one shell (containing one Fe atom as absorber and 8 surrounding iron atoms as scatters) the calculation shows only broad features and no fine structures. Adding a second shell produces more variation in the cross-section; in particular, small peaks are visible at round 717 eV and a small bump at around 737 eV, which increases in intensity when a third shell (with 6 Fe atoms) is added. Including a 4^{th} and 5^{th} shells increases the bump intensity further and introduces additional fine structure (a peak at around 725eV); the result closely resembles that for the bulk (169 atoms). The small feature around 737 eV is not seen in our experiments, probably because it is too small in amplitude and merges into the near-edge structure of the L_2 edge.

Contributions of different shells in FeF_2 and α-Fe_2O_3 were considered in a similar manner and are shown in Fig. 3-5 (b) (c). One can see the greater effect of backscattering of the electron from the O and F atoms, compared to Fe. For FeF_2, both the first and second coordination shells are fluorine atoms. Although calculation with only one shell yields no sharp structure, a broad postpeak appears at about 740 eV. Calculation with two shells produces a postpeak at 744eV that resembles that obtained in a bulk calculation (177 atoms in FeF_2 case). Lack of significant change upon adding a third shell (with 2 Fe atoms) indicates a relatively small contribution from Fe atoms. Adding more shells, i.e.

the 4th shell (4 F) and 5th shell (8 Fe) has little effect on the postpeak at 744 eV, although it gives rise to additional fine structure in the region near the core-edge threshold.

For α-Fe_2O_3, it is interesting to note the similarity and difference of the atom distributions in the shell structure (Table 1) as compared to FeF_2, and their effects on the cross-section. As in the case of FeF_2, a postpeak at around 747eV appears upon adding the second shell; however, α-Fe_2O_3 contains 3 oxygen atoms in the second shell. Similarity of the atom distribution in the first two shells leads to almost the same behavior of the spectra. The main difference in the atom distribution (between FeF_2 and α-Fe_2O_3) occurs in the 3rd and 4th shells. Seven Fe atoms occupy the 3rd and 4th shells in α-Fe_2O_3 but they contribute little to the cross-section. Calculations that include a 5th shell of three O atoms change the fine structure again, so that it closely resembles the bulk case. It is worth noting the difference of the energy position of the postpeak between FeF_2 and α-Fe_2O_3. The posteak for FeF_2 (at 744 eV) is about 3 eV lower than that of α-Fe_2O_3 (at 747 eV), a similar trend being seen in the experimental data. An even higher postpeak position can be seen in Fe_3O_4 in Figure 3-3. The FEFF calculations indicate that this difference arises from their different crystal structures, mainly in the difference in their shell radii [14].

By comparing the contributions of individual shells in α-Fe, FeF_2 and α-Fe_2O_3, we conclude that the near-edge structures derive mainly from the oxygen or fluorine nearest neighbors in the first and second shells, and that the amplitude of the peaks depends on the type of atoms occupying these shells. Light elements, such as O and F, contribute strongly to the ELNES while a heavier element, such as Fe, has less effect. As a result, a prominent postpeak appears in FeF_2 and α-Fe_2O_3 but not in metallic iron. The postpeak are so broad in iron fluorides or oxides, as revealed both by the experiments and calculation. This is attributed to the final-state broadening as discussed in Chapter 1, e.g. excited electron with an over-40-eV kinetic energy has limited mean free path [9]. Meanwhile, this brings difficulty in discriminating the different phases of iron oxides.

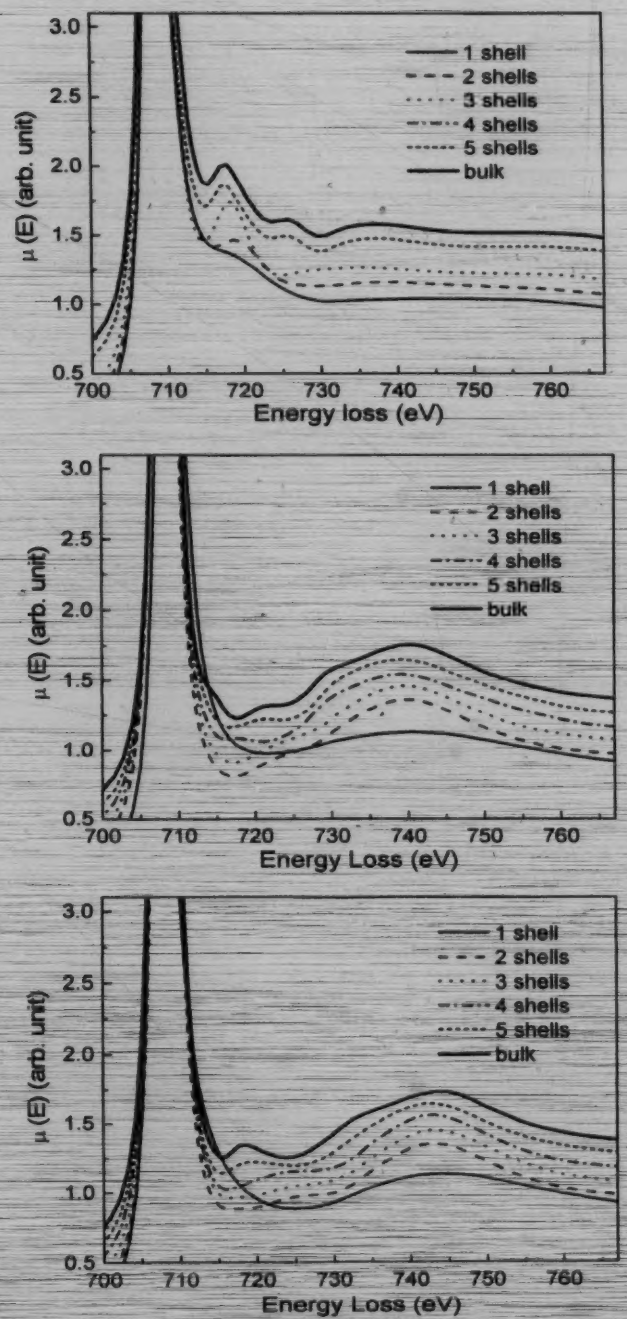

Figure 3-5 Calculated results of the L_3 cross-sections of (a) α-Fe, (b) FeF_2 and (c) α-Fe_2O_3 for scattering clusters of different sizes.

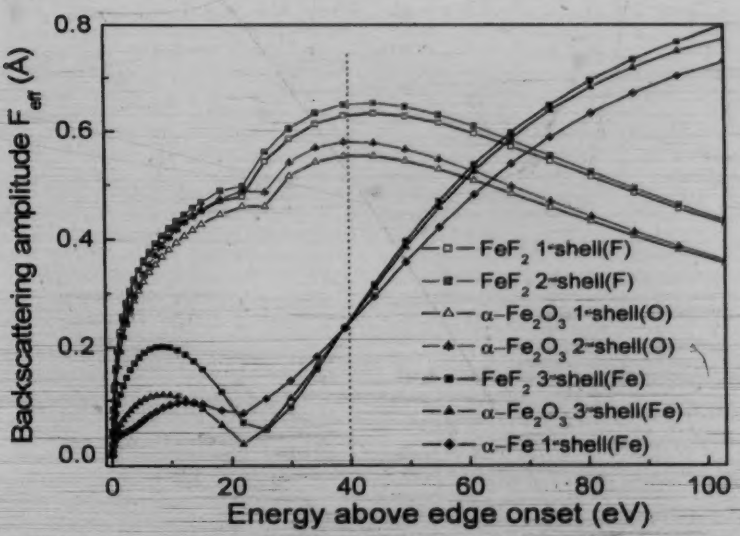

Figure 3-6 Calculated results of the backscattering amplitudes F_{eff} for iron, fluorine and oxygen in α-Fe, FeF_2 and α-Fe_2O_3. The postpeak position is indicated by a vertical dotted line.

3.4 Discussion

As far as we know, there has been no discussion of L-edge postpeaks in transition-metal compounds that are not accounted for by the plural scattering of the transmission electrons. Peaks following the oxygen K-edge of transition metal oxides were reported in [15, 16] and of MgO, CaO, SrO and NiO in [17,18]. The experimental near-edge features were in agreement with MS calculations and could be explained in terms of electron backscattering or scattering resonance, the oxygen shells dominating the backscattering compared to that of metal atoms over the ELNES energy range [15,16]. In support of the interpretation, Wu et. al. showed that the XANES peaks in α-Fe_2O_3 are well reproduced by a MS calculation that took account only of oxygen-atom contributions [15].

The strength of the reflected ejected-electron wave depends on the type and number of the neighboring atoms through their scattering amplitude. This quantity is primarily responsible for the amplitude of the spectra in XANES and EXAFS regions, although other factors, including phase shift and mean free path, have to be considered for a quantitative explanation [19]. The scattering amplitude for light elements is highest for electrons with energies near the Fermi level and decays rapidly with increasing energy. In contrast, the scattering amplitude for heavier elements is relatively low near

the Fermi level and peaks at higher energies. However, low-energy electrons (near the Fermi level) are the ones that contribute in the near-edge region. The dependence of backscattering amplitude and phase shift on the wave vector *k* was calculated and tabulated by Lee and collaborators [20,21], revealing a systematic variation that is consistent with experimental results in the EXAFS region. Additional improvements to the backscattering amplitude and phase shifts were made by McKale et.al. [22] and by Rehr et.al. [23], using a *curved-wave theory*. Later development of the full curved-wave theory allows extension of the calculation into the XANES region, 15eV or more above the edge [22, 23]. The FEFF code developed in Rehr's group allows calculation of the k-dependence of the backscattering amplitude $F_{eff}(k)$ and phase shifts, once the atomic numbers, coordination numbers, and the neighbor distances are known [23]. Figure 3-6 shows calculated results of the backscattering amplitude $F_{eff}(E)$ for the first, second and third shells of FeF_2 and α-Fe_2O_3 and first shell of α-Fe, where contributions to the backscattering amplitude come from Fe atoms in the third shells of FeF_2 and α-Fe_2O_3, from the first shell of α-Fe, and from F and O atoms in the first and second shells of FeF_2 and α- Fe_2O_3. The trends observed are qualitatively similar to published ones [21-23]. The backscattering amplitude F_{eff} at the postpeak energy position (indicated by the vertical dotted line) has a high value for F in FeF_2 and O in α-Fe_2O_3; conversely, F_{eff} for iron in α-Fe, FeF_2 and α-Fe_2O_3 is low at the postpeak position. The effective backscattering amplitude F_{eff} for F and O nearest neighbors (in the first and second shells) is a factor of three larger than that for Fe at the postpeak energy. It is also interesting to note that, in all three different compositions, F_{eff} for iron atoms shows little dependence on the local chemical environment, except for changes at low energies, and that F_{eff} has same small value at the postpeak energy. The open structure of α-Fe, resulting in the larger shell radii, accounts for the small amplitude of the near edge structures [19].

Fe L_2-edges also contribute to the ELNES intensity; the detailed shell contributions show similar trends to those of the Fe L_3-edges, and so are not shown here. The algebraic sum of the integrated L_3 and L_2 intensities, as shown in Fig. 3-4, results in a larger intensity, a further broadening and a small shift of the postpeak in both FeF_2 and Fe_2O_3. Therefore we can conclude that the postpeaks experimentally observed in FeF_2

and α-Fe_2O_3 result mainly from the large backscattering amplitude of F and O atoms, whereas the lack of a postpeak in pure iron is due to the relatively weak backscattering from Fe atoms.

Our FEFF calculations predict additional fine structure between the postpeak and the L-threshold, resulting from inter- or intra-shell multiple scattering [15, 16]. However this fine structure is not observed in our experiments, either because of insufficient energy resolution or because it is an artifact associated with the model: a muffin-tin approximation is used in the self-consistent potential calculations in the FEFF model. Outside the muffin tin, the charge density is not spherical and the charge density is not constant; instead there is often a buildup of charge between neighboring atoms. This "warping" of charge density can be treated by taking advantage of the periodicity of the crystal, as in band structure models [19]. In the FEFF code, the warping is ignored for regions far beyond the core edge, since the kinetic energy of the electron is typically much larger than the size of the warping potential, but it is a serious problem in the near-edge region. In the FEFF calculations, charge transfer is accounted for by charge redistribution in the self-consistency loops, which enables the transfer direction agree well with the electronegativity of the elements [24]. The charge redistribution due to bonding however affects only the very low energies and near L-threshold, and has little influence to the postpeak region. In addition, the dynamic screening effect is important in calculating the iron L-edges, b[illegible] is not accounted for in the FEFF8.2 code [12]. More accurate calculations of the Fe-L edges should consider multiplet effects, as discussed in [25]. In summary, fine structure close to the L-edge threshold is beyond the validity of the real-space scattering model used in our FEFF calculations.

The white-line ratio (WLR) has been widely used to characterize the oxidization state of transition metals. For example, there are different WLR values in the iron and its oxides, depending on the oxidization state. However, quantification of the white lines involves considerable effort in spectral processing and fitting, and results obtained using different spectrum processing and fitting procedures are not always consistent. If, as suggested above, a correlation between the postpeak and the presence of fluorine and oxygen is a general effect, the ELNES postpeak may act as a useful characteristic feature for all transition metals and their compounds (this is discussed in *Chapter 5* using data

from EELS Atlas in Ref. [7]). In support of this statement,we note that a prominent postpeak is also visible in the near edge structure of the Co-L edge in CoF_2 and disappears with the removal of fluorine under TEM irradiation [8]. Our calculations of the near-edge structures of the Co-L_3 edges for metallic Co, CoF_2 and CoO are shown in Figure 3-7. They indicate that postpeaks are expected for CoF_2 and CoO, but not for metallic Co. The postpeak may therefore constitute a fingerprint (indicating high oxidization state) that can be used as a convenient check on the oxidation of transition metals.

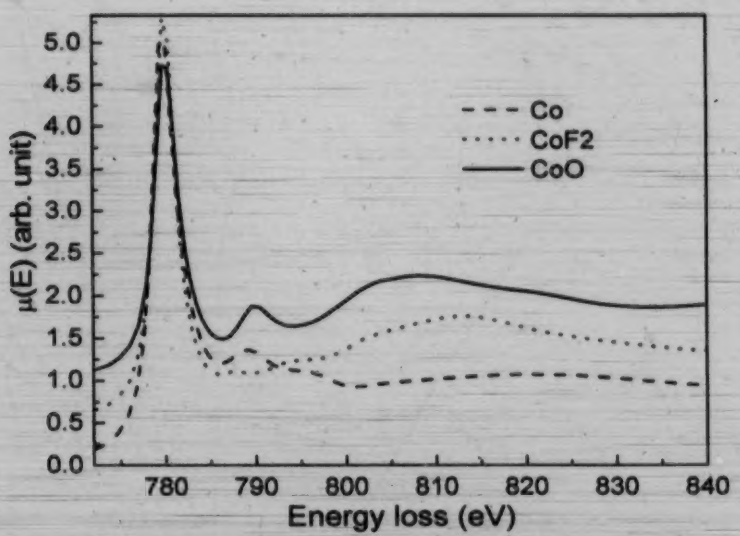

Figures 3-7 Calculated results of the Co-L_3 cross-sections of Co, CoF_2 and CoO for cluster sizes of 81, 83 and 81 atoms respectively.

3.5 Conclusions

A broad peak (postpeak) is observed about 40 eV above the Fe L-edge in iron fluoride and oxides. In very thin specimens, this peak cannot be attributed to plural scattering. Instead, it must be interpreted in terms of backscattering of the excited core electron from halogen or oxygen atoms, as indicated by RSMS calculations using the FEFF 8.2 code. Other experimental data, and calculations performed for cobalt oxide and fluoride, suggest that this peak is a characteristic feature of other transition metal compounds where the metal is in a high oxidation state. Consequently the postpeak may be useful in assessing the oxidation of transition metals.

Acknowledgements

This work was supported by *NRC* and *NSERC*. The authors would like to thank M.R. Freeman and M.S. Moreno for helpful discussions, and D. Mullin and G. Popowich for technical assistance. FW wishes to acknowledge support from Prof. Z. Xu and from the Killam Trust.

References

[1] S. Sun, C.B. Murray, D. Weller, L. Folks, A. Moser, Science **287** (2000) 1989.

[2] R.H. Kodama, J. Mag. Mag. Mater. **200** (1999) 359.

[3] E.A. Stern, S.M. Heald, E.E. Koch, Handbook of Synchrotron Radiation, North-Holland, New York, (1983) P. 995-1014.

[4] F. Wang, M. Malac, R.F. Egerton. Micron. **37** (2006)316.

[5] R.D. Leapman, L.A. Grunes, P.L. Fejes, Phys. Rev. B **26** (1982) 614.

[6] C. Colliex, T. Manoubi, C. Ortiz, Phys. Rev. B **44** (1991) 11402.

[7] C.C. Ahn, O.L. Krivanek, R.P. Brugner, M.M. Disko, P.R. Swann, EELS Atlas. ASU HREM facility and Gatan Inc. (1983).

[8] M. Malac, M. Schoefield, Y. Zhu, R.F. Egerton, J. Appl. Phys. **92** (2002) 1112.

[9] R.F. Egerton, Electron Energy-Loss Spectroscopy in the Electron Microscopy, 2nd ed., New York: Plenum Press, 1996.

[10] Y.Y. Zhou, M.G. Zhao, J. Phys. C: Solid State Phys. **20** (1987) 1827.

[11] P.A. Van Aken, S. Lauterbach, Phys. Chem. Minerals **30** (2003) 469.

[12] A.L. Ankudinov, B. Ravel, J.J. Rehr, S.D. Conradson, Phys. Rev. B **58** (1998) 7565.

[13] D.M. Pease, A. Fasihuddin, M. Daniel, J.I. Budnick, Ultramicroscopy **88** (2001) 1.

[14] A. Bianconi, M.Dell'Ariccia, A. Gargano, C.R. Natoli, in EXAFS and Near-edge structure structure, edited by A. Bianconi, L. Incoccia and S. Stipcich, Springer-Verlag, Berlin (1983) P. 57.

[15] Z.Y. Wu, S. Gota, F. Jollet, M. Pollak, M.Gautier-Soyer, C.R. Natoli, Phys. Rev. B **55** (1997) 2570.

[16] H. Kurata, E. Lefevre, C. Colliex, R. Brydson, Phys. Rev. B **47** (1993) 13763.

[17] X. Weng, P. Rez, Phys. Rev. B **39** (1989) 7405.

[18] P. Rez, J. Bruley, P. Brohan, M. Payn, L. A. J. Garvie, Ultramicroscopy, **59** (1995) 159.

[19] J.J. Rehr, R.C. Albers, Rev. Mod. Phys. **72** (2000) 621.

[20] P.A. Lee, J.B. Pendry, Phys. Rev. B **15** (1975) 2862.

[21] B.K. Teo, P.A. Lee, J. Am. Chem. Soc. **101** (1979) 2815.

[22] A.G. McKale, B.W. Veal, A. P Paulikas, S. K. Chan, G. S. Knapp, J. Am. Chem. Soc. **110** (1988) 2763.

[23] J.J. Rehr, J. Mustre de Leon, S.I. Zabinsky, R.C. Albers, J. Am. Chem. Soc. **113** (1991) 5135.

[24] B. Ravel, J. All. Comp. **401** (2005) 118.

[25] Frank de Groot, Coord. Chem. Rev. 249 (2005) 31.

Chapter 4 Multilayer route to iron nanoparticle formation in an insulating matrix

(F. Wang, M. Malac, R. F. Egerton, A. Meldrum, X. Zhu, Z. Liu, N. Macdonald, P. Li, and M.R. Freeman, J. Appl. Phys. (in press))

4.1 Introduction

Ferromagnetic nanoparticles embedded in an insulating matrix have been extensively studied owing to the richness of their physical properties and the wide range of potential applications (e.g., see Refs. 1 and 2). Magnetization behavior of ferromagnetic nanoparticles has been studied for many years,[3] and it is known that particles in a matrix are different from free-standing particles or particles dispersed in a non-bonding medium.[4] Such nanocomposite systems showed complicated magnetic properties influenced by many factors, such as the dipole interaction,[5] the exchange coupling between the metallic core and oxide shell,[6] surface anisotropy,[7] magnetoelastically induced anisotropy due to large stress between a metal particle and the surrounding matrix,[8] and shape anisotropy.[3]

In recent years, various methods of nanocomposite fabrication have been developed, including evaporation, sputtering, ball milling, ion implantation and microemulsions.[9-15] The particle size strongly depends on the preparation parameters and methods, and can be difficult to control. Ion implantation was shown to produce metallic iron nanoparticles that exhibited large Faraday rotation and fast dynamic response,[3,13,16] but the size distribution was wide. Effective size control has been pursued, using self-assembly in ordered nano-materials,[17-19] and chemical synthesis of monodispersed ferro/ferrimagnetic nanoparticles by reduction of metal salts and/or thermal decomposition of organometallic precursors.[2, 20]

An additional problem is nanoparticle oxidation, arising from the large surface-area-to-volume ratio and the high electro-negativity of metallic iron. For example, iron/gold core/shell nanocomposites prepared by a microemulsion technique were

expected to produce metallic iron with a uniform size distribution,[8] but the iron component was oxidized. Very recent studies showed that the oxidation resulted from the rough surface of Au shell, and complex iron oxide phases were identified in the iron/gold core/shell nanocomposites.[15, 21] Oxidation seems to be a persistent problem in core/shell nanoparticles[15, 20-23] Size control down to nanometer level has been well accomplished in the chemical synthesis or the combination of self-assembly and patterning techniques, but the unprotected metallic nanoparticles are susceptible to oxidation.[16-19] Development of useful nanocomposite materials and fabrication processes still poses a challenging problem.

For a nanocomposite system, microstructural analysis is critical for understanding the physical properties, particularly when surface atoms in the metallic nanoparticles are oxidized or bonded to the matrix. Electron / x-ray diffraction is suitable for identifying the crystallographic structure of nanoparticles, but provides only average properties, and it is difficult to detect oxidation of the particle surface. Additionally the metal oxides that are often amorphous are difficult to detected by diffraction techniques. High resolution TEM shows the crystal structure on an atomic level but the properties of the nanoparticle-matrix interface can be difficult to ascertain. Therefore it is important to develop convenient methods of characterizing the particle-matrix interfacial layer, such as the oxidation state and even oxidation layer thickness, as a reference for the study of other physical properties. In this work, we show that iron nanoparticles with a narrow size distribution can be fabricated by annealing Fe layers that are protected from oxidization by encapsulation in a SiO_2 matrix. The microstructure and the oxidation were examined in an analytical TEM, using electron energy-loss spectroscopy (EELS) and energy-loss near-edge structure (ELNES). We relate the magnetic properties to the results of this microstructural analysis.

4.2 Experiment

Alternating layers of iron and silicon dioxide (Fe-SiO_2) were prepared by electron-beam evaporation and annealing. Five layers of SiO_2/ Fe (SiO_2 purity: 99.999%; Fe: 99.95%) were deposited onto 4-nm thick carbon films (supported by copper grids), 50 nm Si_3N_4 membranes, and 1x1 cm^2 Si wafers in an ultra-high vacuum (UHV) system with 10^{-10}

Torr base pressure. All samples were deposited and annealed *in-situ*. The thickness of the SiO_2 layers was fixed at 3 nm, while the Fe layer thickness was varied to control the iron particle size. Before the deposition, the substrates were baked for 10 hours in the load-lock chamber at 180°C to remove adsorbed water. One layer of 8-nm SiO_2 film capped the 5th (last) layer of Fe, to protect the iron films from the atmosphere. The pressure during film growth of Fe and SiO_2 was 10^{-9} Torr (with $H_2O$and O_2 partial pressure: 10^{-11} Torr and 10^{-12} Torr respectively). Films were deposited at a rate of 1.0 Å/s onto substrates kept at room temperature. The film thickness and deposition rate were monitored by a quartz-crystal monitor. The resulting Fe/SiO_2 multilayers were annealed *in-situ* in the chamber at a temperature of 880°C for one hour at 10^{-10} Torr. The samples are named after the iron film thickness; for example Fe10 implies nominal iron layer thickness 10 Å in the as-deposited film. The composition of the as-deposited samples is listed in the second column of Table I.

The morphology of the as-grown and annealed samples on the carbon films and Si_3N_4 membranes was examined by plan-view TEM using a 200 kV LaB_6 instrument (JEOL 2010) equipped with Gatan 666 parallel-EELS spectrometer. The samples on Si substrates were also examined in cross-sectional TEM, after thinning by standard polishing and ion milling procedures. The presence of iron oxides was investigated with selected area electron diffraction (SAED) and core-loss EELS. The energy-loss spectra were collected in TEM diffraction mode (image-coupled spectrometer) with a collection semi-angle of 1.5 mrad and energy dispersion of 0.3 eV/channel. In recording the spectra, an area of about 2.5 micron in diameter (in the specimen plane) was chosen by a selected area aperture, containing thousands of iron nanoparticles. The analysis was done immediately after fabrication and repeated after a 3-month storage in laboratory air. In-plane magnetization hysteresis was measured using magneto-optical Kerr effect (MOKE) measurements with a field sweeping range of 4000 Oe (=318.3 KA/m), immediately after fabrication, and also measured on a 9T-PPMS (Physical Properties Measurement System, Quantum Design) dc magnetometer with a field range of 20000 Oe (= 1591.5 KA/m) after 14-month storage in laboratory air.

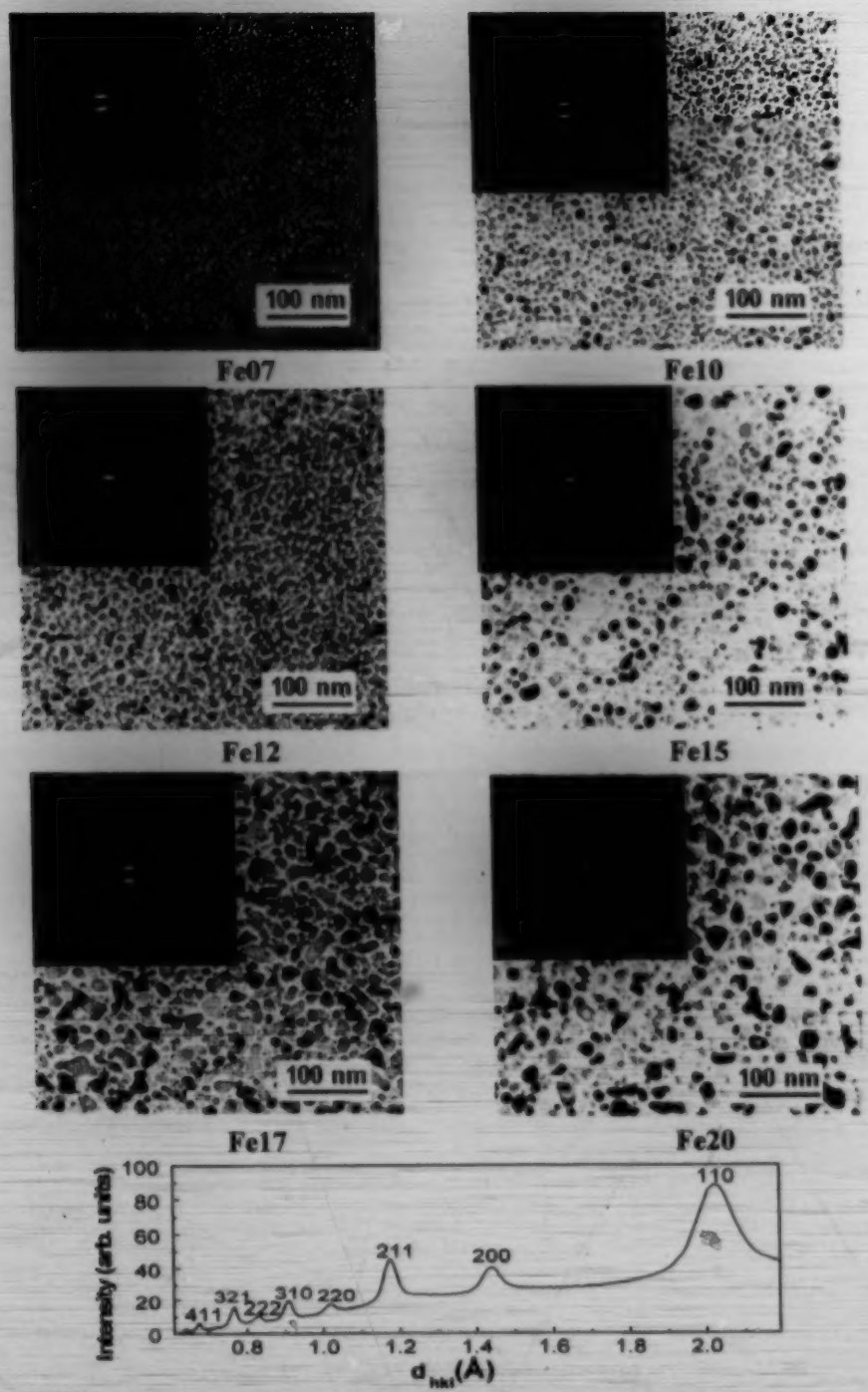

Figure 4-1 Plan-view TEM images and SAED patterns (inset) of iron nanoparticles embedded in a silicon dioxide matrix. On the bottom is an integrated intensity profile of the diffraction peaks of Fe12; the peaks can be well indexed according to iron bcc structure.

4.3 Results and discussion

4.3.1 Microstructure and oxidation analysis

The morphology and structure of films with different nominal iron thickness are shown by plan-view TEM in Fig. 4-1. These bright-field TEM images display the iron nanoparticles (darker regions) embedded in the SiO_2 matrix (lighter regions). Figure 4-1 also reveals that the Fe nanoparticles are densely distributed in the SiO_2 matrix and well separated from each other. SAED patterns (figure insets) and diffraction-intensity profiles show well-defined rings that can be assigned to randomly oriented, crystalline bcc-Fe particles. The average diameter of the Fe nanoparticles depends on the initial thickness of the iron film. Individual diameters of the nanoparticles were measured from plan-view TEM images and the results of a size analysis of 300 to 400 particles for each film are shown in Fig. 4-2. The size distributions are rather narrow; the standard deviations and mean nanoparticle diameters are listed in Table I.* The size variation (given by the standard deviation) is smaller for low Fe thickness. The standard deviation increases rapidly beyond Fe17, in which the iron particles start to coalesce into extended structures. In the Fe30 specimen, the particles coalesced so extensively that no individual particles could be discerned.

Based on the diffraction patterns for all of the samples (insets in Fig. 4-1), bcc-Fe is clearly the predominant phase; diffraction rings associated with iron oxide phases were rarely observed. However, some oxidization of the particle surface is expected due to the high chemical reactivity of iron. In our recent work, we established that a post-edge peak in the L-shell ELNES constitutes a fingerprint (indicating high oxidization state) and can be used as a convenient check on the oxidation of transition metals.[24] This postpeak found in various kinds of iron oxides can be attributed to strong backscattering of the excited L-electrons from oxygen anions. Even a slight amount of oxidation can be detected from the appearance of this post-edge peak, located at about 40 eV above the iron L3 edge.[24]

* Normal distribution is used here; the fitting by the lognormal function, which is more reasonable in describing the particle size distribution, gives similar results for mean diameter and deviations.

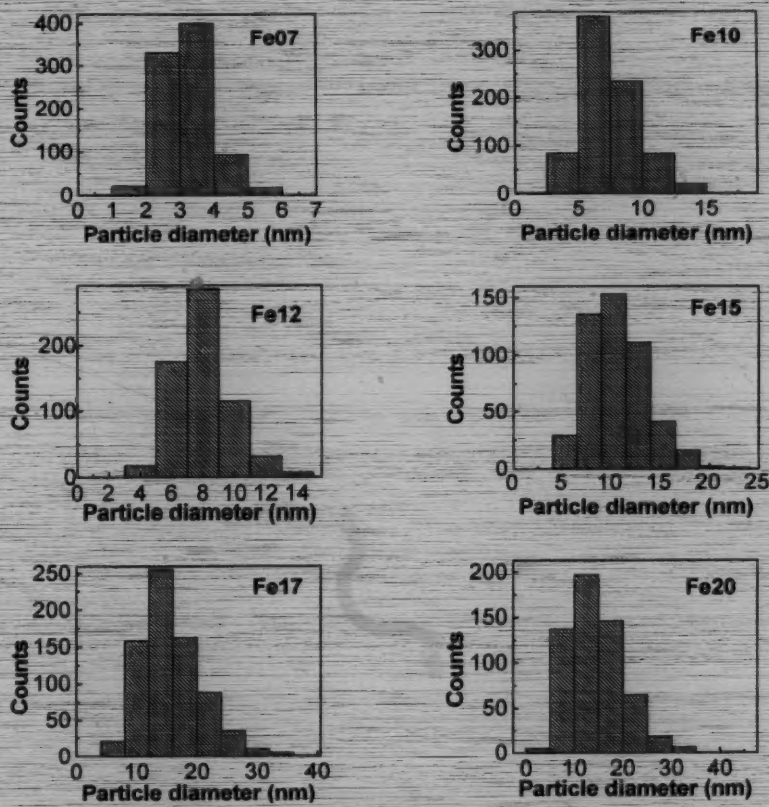

Figure 4-2 Size distribution of iron nanoparticles embedded in a silicon dioxide matrix. The averaged particle diameter and standard deviations obtained by fitting to a normal distribution are listed in Table I.

Table 4-1 Composition, particle diameter, coercivity and saturation of the samples (saturation magnetization (M_s) measurements were made after 14-month storage in laboratory air)

Sample	Composition	Particle diameter (nm)	Coercivity (Oe)	Ms (emu/cm^3)
Fe07	Fe/SiO2: 0.7 nm/3.0 nm	3.2±0.7	0	620
Fe10	Fe/SiO2: 1.0 nm/3.0 nm	7.4 ± 2.2	33	920
Fe12	Fe/SiO2: 1.2 nm/3.0 nm	8.0±1.8	113	
Fe15	Fe/SiO2: 1.5 nm/3.0 nm	10.6±2.9	251	1610
Fe17	Fe/SiO2: 1.7 nm/3.0 nm	15.7±5.1	415	
Fe20	Fe/SiO2: 2.0 nm/3.0 nm	21.0±7.7	666	
Fe30	Fe/SiO2: 3.0 nm/3.0 nm	~50	593	
Fe150	Fe/SiO2: 15 nm/0 nm	Continuous film	76	210

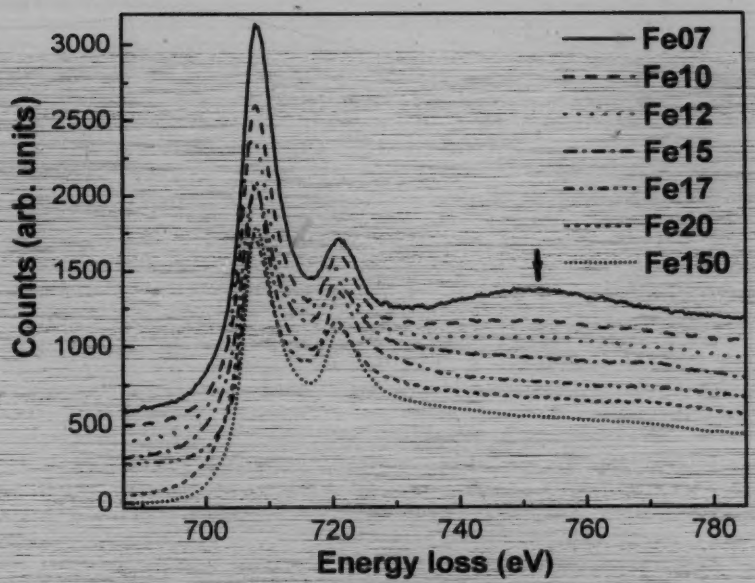

Figure 4-3 Energy-loss near-edge structure of Fe-L_{23} edges in iron nanoparticles. The ELNES of a 15 nm thick metallic iron film, with flat feature post the L23 edges, is also shown for comparison; the post-edge peak position is indicated by an arrow.

Figure 4-3 shows the near edge structure of the iron- L23 edges from spectra of all the samples, after removal of background using polynomial fit and of multiple scattering by Fourier-ratio deconvolution. A prominent post-edge peak can be seen in sample Fe07, even though oxidation is extremely difficult to distinguish from the diffraction patterns. The post-edge peak is still observed in samples Fe07, Fe10 and Fe12, but is barely observable in other samples. From the strong presence of metallic bcc-Fe in the diffraction pattern and from the presence of the post-edge peak, we deduce that iron oxide volume is small compared to the volume of bcc Fe, and is expected to be predominantly on the particle surface. Our recent high-angle annular dark-field scanning TEM images of single iron nanoparticles show metallic iron crystal lattice that continues to the edge of the nanoparticle, which supports the surface oxide model.[25]

To further clarify the oxidation type the diffraction-intensity profiles, integrated along a full circular path in the diffraction pattern, were used to enhance the visibility of the weak diffraction rings. At the bottom of Fig. 4-1 is a profile for sample Fe10, in which a weak and broad peak, labeled by an arrow, may be attributed to (113) of γ-Fe_2O_3 (maghemite) or Fe_3O_4 (magnetite), as determined by close inspection of the diffraction

intensity profile. The peak was only observable in the samples with smaller iron nanoparticles. Both magnetite and maghemite have the inverse spinel structure, and their lattice constants are similar. Superlattice reflections specific to maghemite are not detectable due to the lack of long-range periodicity in the present specimens. Therefore magnetite and maghemite cannot be distinguished using diffraction techniques.[26]

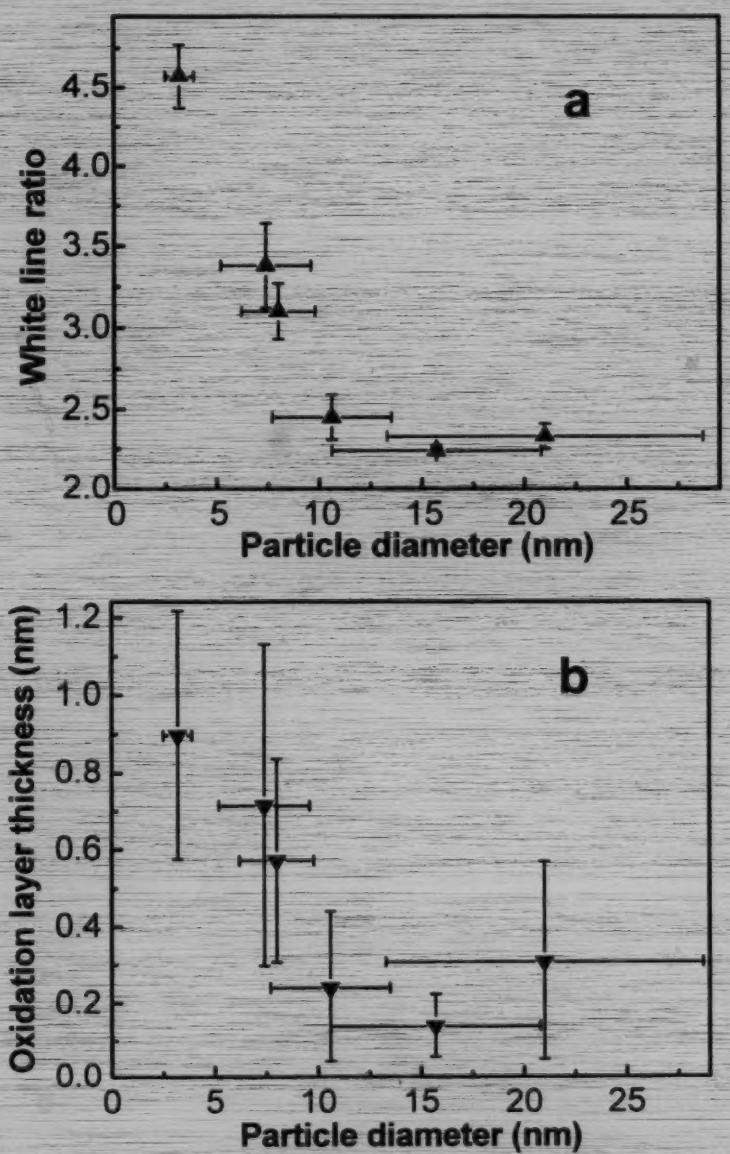

Figure 4-4 Dependence of (a) white-line ratio and (b) oxidation-layer thickness on the diameter of iron nanoparticles. Measurement errors are also shown.

To establish the nature of the oxide phase, the valence state of the transition metal oxide was determined by white-line ratios (integrated L3/L2 intensity ratio).[27-29] The L2 and L3 edges (white lines) correspond to excitations of 2p electrons to bound 3d states near the Fermi level; white-line intensity ratios are found to deviate from the statistical value (2:1) and vary in accordance of the occupancies of the 3d levels, and thus the oxidation state. We used a standard procedure to quantify the white-line peaks; multiple scattering was removed by Fourier-ratio deconvolution, and the white-line component of the experimental data was fitted to a combination of Lorentzian and arctangent functions.[24] Using this procedure, the white line intensities can be separated from the continuum background, and the fit was found to match the experimental data quite well.[30] The measured ratio is 4.6 ± 0.3 in Fe07, much higher than the calculated value of 3.6 ± 0.2 of a Fe_3O_4 control sample.[24] This indicates a higher level of oxidation and therefore that γ-Fe_2O_3 is the main oxidation phase in sample Fe07. This should be also true for other samples, considering that they were all annealed under the same conditions.

Assuming that maghemite (γ-Fe_2O_3) is the only oxidation phase and that the white-line ratio (WLR) depends linearly on the atomic fraction of the oxide, the degree of oxidation can be estimated according to:

$$WLR_{exp} = WLR_{\gamma-Fe_2O_3} \cdot x + WLR_{Fe} \cdot (1-x) \qquad (4.1)$$

Here WLR_{exp} is the experimental WLR value for different samples, $WLR_{\gamma\text{-}Fe2O3}$ is the WLR value for γ-Fe_2O_3, WLR_{Fe} is the WLR value for metallic Fe, and x is the percentage of oxidization to α-Fe_2O_3. In the calculation, we used $WLR_{\gamma\text{-}Fe2O3}$= 4.8±0.2 and WLR_{Fe}= 2.1±0.2, as obtained in previous experiments.[24] Figure 4-4 (a) shows the dependence of white-line ratio on the particle diameter; the decrease of WLR with particle size indicates reduced oxidation with increase in the particle size. The γ-Fe_2O_3 percentage can be calculated for all the samples according to Eq. (4.1), and an oxidation-layer thickness can be deduced by assuming that oxidation occurs only at the surface. The results are shown in Fig. 4-4 (b). It appears that only about one atomic layer of iron is oxidized on the surface of the larger nanoparticles.

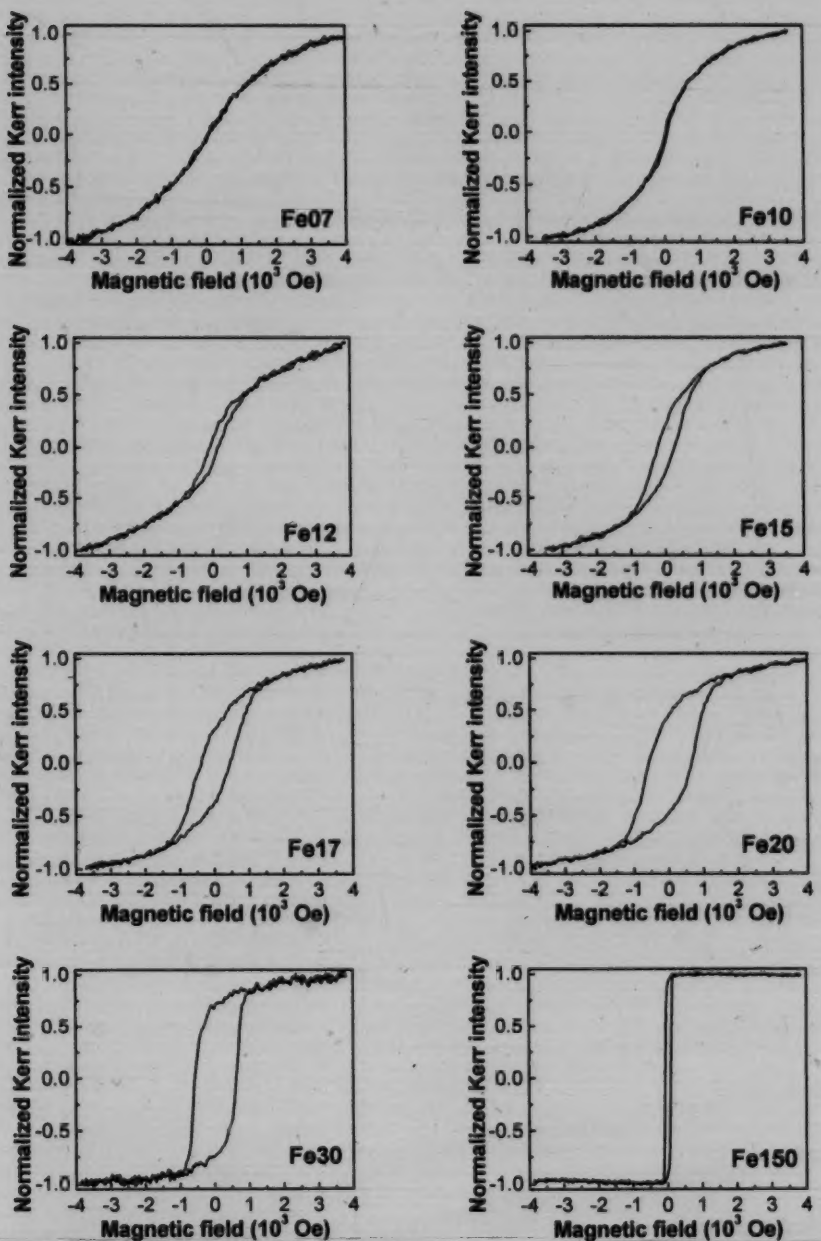

Figure 4-5 Normalized magnetization hysteresis measured by MOKE for iron nanoparticles in different samples, as labeled on the panels.

4.3.2 Magnetic properties

Magnetic properties of the nanoparticles were investigated by MOKE measurements. Figure 4-5 shows the in-plane hysteresis loops for samples with different iron-layer thicknesses. Thicker iron layers resulted in larger particles and a corresponding increase

in the coercivity. The samples with the smallest iron clusters (i.e. Fe07) exhibit superparamagnetism, in which the activation energy is small and the magnetization is easily flipped by thermal fluctuations. Ferromagnetic behaviour first appears in sample Fe10, where a single-domain magnetic structure is energetically favored for each particle. The maximum coercivity, measured in Fe20, was 666 Oe. The remanences are much higher than those of iron nanoparticles implanted in SiO_2[5, 13] indicating less perpendicular anisotropy in the present samples. In samples with large Fe thickness (Fe30), the Fe particles were sufficiently large to support more than one domain (thereby reducing the demagnetization energy). Consequently, the coercivity decreases with further increase in initial Fe layer thickness.[31] Finally, in the case of the continuous Fe film, the coercivity was only 76 Oe for the 15-nm Fe film. The hysteresis loops for these iron nanoparticles never reach saturation within field range of ± 4000 Oe, due to the persistent presence of a small proportion of superparamagnetic particles (see Figure 4-1).

In Figure 4-6 (a) (b), coercivity H_c is plotted as a function of both particle diameter D and the volume-filling factor f_v (defined as the iron volume in relation to the total volume in the as-deposited films), as measured by MOKE. The dotted line represents a calculated result of the coercivity H_c as a function of the particle diameter D, as discussed below. H_c increases rapidly with increasing particle size or filling factor, reaches a maximum near D~20 nm, and then decreases slowly. An inverse relationship, namely $H_c \propto 1/D$ above the maximum,[32] is only observed approximately because of the limited number of data points. The behavior of H_c as a function of particle size below D~20 nm can be investigated by analyzing the factors influencing the coercivity.

First, magnetoelastic effects, which may lead to larger coercivity if each iron nanoparticle is strained by a large interfacial stress, can be ignored in the Fe-SiO_2 nanocomposite system, where the iron nanoparticles were produced from a slow annealing process during which the strain can be released. The magnetoelastic energy is so small relative to the magneto-crystalline anisotropy energy that it can be neglected.[26] Second, based on TEM observations, iron particles are spherical, and thus shape anisotropy is negligible. Passivation of maghemite on the surface of iron nanoparticles can alter their magnetic behavior by exchange coupling between the oxidation layer and metallic core,[33] such an effect is expected to be small in consideration of the slight

oxidation.[34] It has been confirmed that the surface anisotropy plays an influential role for fine particles within a thin layer of oxides.[7, 35] By assuming an assembly of spherical, random, single domain particles, the following expression can be derived approximately, using the Stoner-Wohlfarth model:[36]

$$H_c(V,T) = H_c(V,0)[1-(\frac{V_p}{V})^{0.77}] \qquad (4.2)$$

Here, V is the volume of the nanoparticle and V_p is the critical volume for a superparamagnetic limit.

Based on Eq. (2), Chen et al., calculated the particle-size dependence of the coercivity for noninteracting nanoparticles and confirmed the dominant effects of the uniaxial surface anisotropy on the reversal process, by comparison to the experimental data.[32] The expression for the coercivity in the case of uniaxial surface anisotropy can be written as:

$$H_c(d,T) = \frac{5.76K_s}{M_s d}[1-(\frac{25kT}{K_s \pi d^2})^{1.155}] \qquad (4.3)$$

In Eq. (4.3), K_s is the surface anisotropy and M_s is the saturation magnetization. In Fig. 4-6 (a), the dotted line shows the calculated results according to Eq. (4.3); the temperature T = 295 K was fixed and K_s =3.8x10^{-3} kA/m^2 and M_s =1420 kA/m were obtained in fitting the experimental data. Except for the smallest nanoparticles (the superparamagnetic Fe07), the calculated line fits the experimental data of small particles well, while it deviates from the experimental data for large particles. Although the size distribution can cause the slight deviation, the dipole interaction can be another important reason for the discrepancy. The model is only approximate in describing the composite system, since it assumes noninteracting nanoparticles; in practice the dipole-dipole interaction cannot be ignored for nanocomposites with small inter-particle distances and high volume-filling factors, such as the iron nanoparticles in Fe17 and Fe20. The strong magnetic anisotropy, as implied by big difference between in-plane and out-of-plane magnetization hysteresis loops, was observed in our recent measurements (not shown here), which shows the strong dipole-dipole interactions between iron nanoparticles.[5, 37]

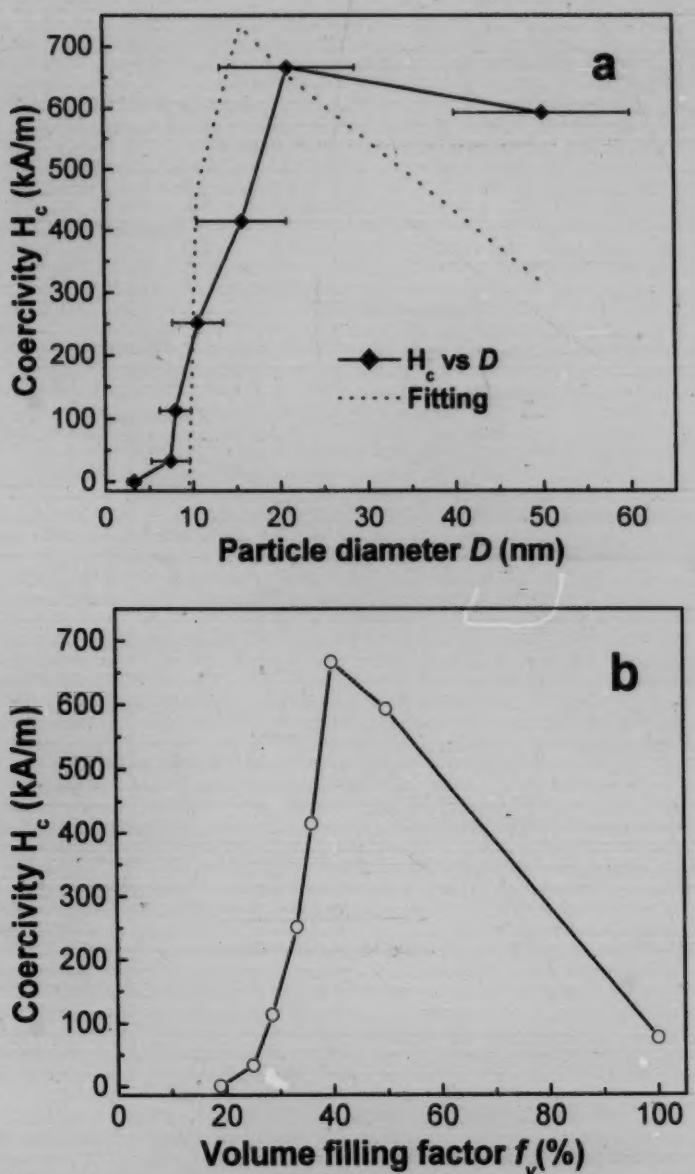

Figure 4-6 Dependence of the coercivity H_c on particle size (a) and volume-filling factor (b). Experimental data are shown by a solid line with solid diamond for the particle-diameter in (a) and by a solid line with hollow circle for filling-factor dependence in (b); dotted line represents the calculated dependence of coercivity H_c on the particle diameter. A filling factor of 100% corresponds to a continuous film: Fe150 in our experiments.

4.3.3 Morphology and air resistance of iron nanoparticles

In addition to plan-view microscopy (shown in Fig. 4-1), the microstructure of the sample Fe15 grown on Si substrates was studied by cross-sectional TEM imaging. As shown by

Figure 4-7(a), rounded iron nanoparticles are well isolated by the SiO_2 matrix. The particle sizes are comparable to those seen in the plan-view images of Fig. 4-1. Comparison between plan-view and cross-sectional TEM leads to the conclusion that the iron nanoparticles are spherical in shape; the particle size and structure are independent of substrate type, due to the buffering effects of the 8-nm SiO_2 layer. On the other hand, it is interesting to observe that there are no longer numerous alternating Fe and SiO_2 layers; the multilayers have amalgamated during the formation of iron nanoparticles. Therefore there must be significant diffusion of iron through the SiO_2 layers.

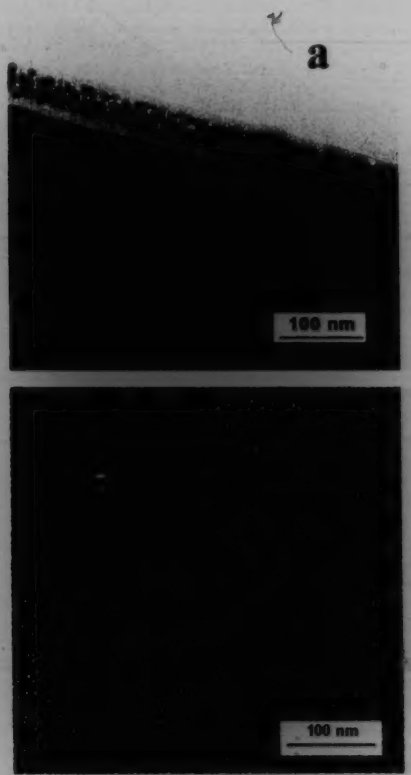

Figure 4-7 (a) Cross-sectional bright-field image for Fe 15 (on Si) after annealing. (b) Plan-view TEM image for as-grown **Fe15** sample.

Figure 4-7(b) shows a bright field image of the as-deposited Fe15 sample before annealing. Small iron clusters (approximately 1 to 2 nm in diameter) are well dispersed in the SiO_2 matrix; the inset SAED pattern indicates that these clusters have the bcc iron phase. Fe clusters (rather than a continuous Fe film) were formed in the as-grown sample because of the small thickness of the iron layer. These very small particles are

superparamagnetic (as measured with MOKE, not shown here); annealing for one hour resulted in ferromagnetic iron nanoparticles of increased diameter. The atom mobility is greatly enhanced, promoting the diffusion of iron.

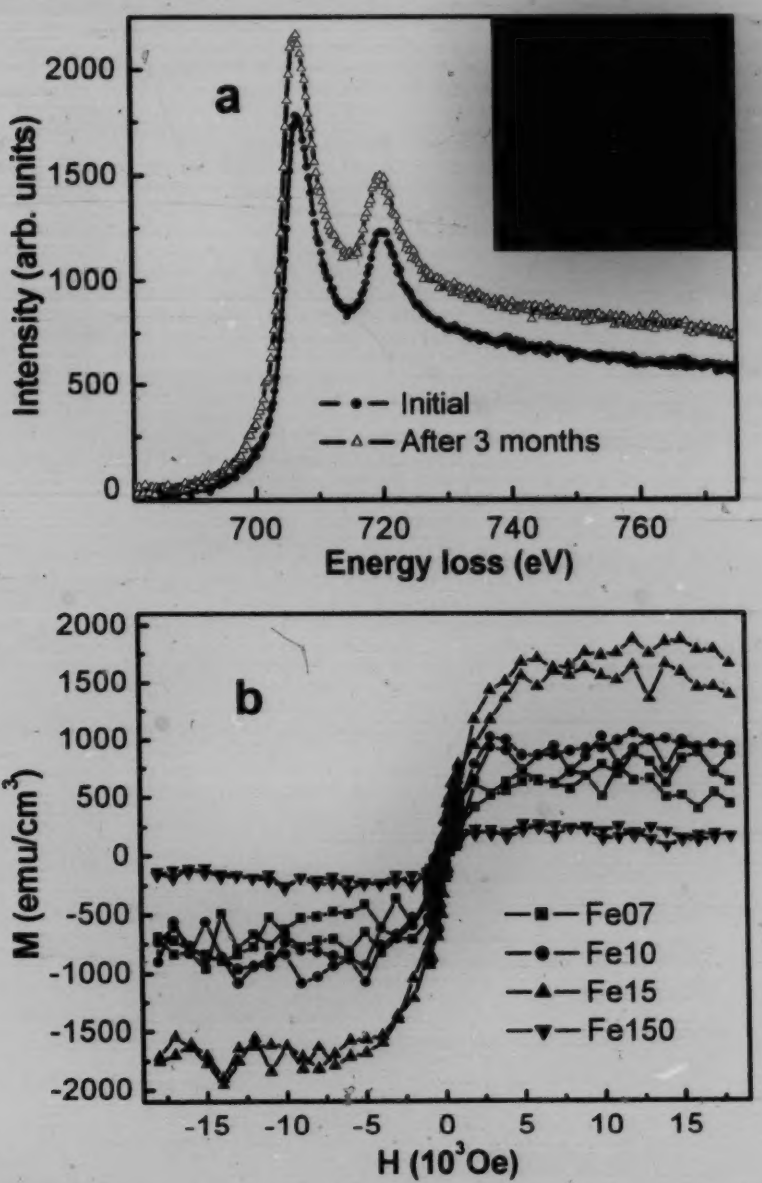

Figure 4-8 (a) Comparison of the white lines of **Fe15** as initially fabricated (solid circle) and after exposure to air for three months (hollow triangle). Inset is a selected-area diffraction pattern of Fe15 after exposure to air for three months. (b) In-plane magnetization of samples Fe07, Fe10, Fe15 and Fe150, after 14-month storage in laboratory air.

For practical applications, long-term resistance to oxidization is important for retaining well-defined magnetic properties. In order to evaluate their stability, the iron phases of all the particles were investigated after storage in laboratory air for three months. There were no phase changes within the accuracy of electron diffraction measurements, as shown in the inset of Figure 4-8 (a). The ELNES of Fe-L edge in Fig. 4-8 (a) shows that post-edge peak is still invisible and the calculated white-line ratio remains unchanged at 2.4 ±0.2, indicating no further oxidization of the encapsulated iron. The SiO_2 matrix became compact and denser when annealed at high temperature, and thus nanoparticles were effectively protected.

The saturation magnetization M_s of the iron anoparticles in SiO_2 matrix was also measured from the magnetization hysteresis *M(H)* after 14-month storage in laboratory air, as shown in Fig. 4-8 (b); the M_s values (within an error of 10%) were listed in Table I. In this measurement, a field (of 20000 Oe in this case) big enough to saturate the sample was applied, and then *M(H)* was measured as the field was reduced and reversed in direction. The M_s value of Fe150 is only about 210 emu/cm^3, being so low in comparison to saturation magnetization of the bulk Fe (being 1707 emu/cm^3, at 290 K).[3] The M_s values for iron nanoparticles are much bigger than that of the Fe150, and increase with the increase of the particle size, for example, from 620 emu/cm^3(for Fe07) to 1610 emu/cm^3 (for Fe15). The magnetization measurements are consistent with the ELNES results, and further confirmed the good protection of the SiO_2 matrix to the iron nanoparticles; the lower M_s values than that of bulk iron, is interpretable in accordance of surface oxidation. Fe150 is a 15-nm thick continuous film, without annealing; the capped 8-nm SiO_2 film could only give temporary protection to the iron content. Owing to the low iron filling factors in these samples and small pieces of samples (smaller than 5x5 mm^2) were used in the measurement, big errors (within 10-20 %) were expected in the saturation magnetization measurement; the improvement on the signal-to-noise ratio and insight study of the magnetic properties by further measurement at low temperature are being pursued. Overall, the oxidation resistance and strong magnetization retained in the iron nanoparticles, being so important for the practical application, has been well examined using combined measurements.

In summary: spherical, isolated and stable iron nanoparticles have been fabricated, embedded in a SiO_2 matrix. Size control and chemical protection were achieved in this system, as demonstrated by characterization in an analytical TEM. A magnetization study shows the importance of surface anisotropy and dipole interaction in this system. This concept is promising for the production of arrays of discrete metallic nanoparticles below 10 nm through the addition of a lithographic patterning technique. It has also been demonstrated that ELNES is very useful in detecting slight oxidation of metallic nanoparticles.

Acknowledgements

This work was supported by *NRC, NSERC, iCORE and AsRA*. The authors would like to thank Don Mullin, Greg Popowich and Cindy Blois for technical assistance in sample preparation, and Dr. Oksana Zelinska and Prof. Arthur Ma for magnetization measurements. FW wishes to acknowledge support from Prof. Zhenghe Xu and from the *Killam Trust* and help from Dr. Yimei Zhu and Dr. Marvin Schofield, at Brookhaven National Laboratory.

References

[1] Vincent Rotello, Nanoparticles: Building Blocks for Nanotechnology, Kluwer Academic/Plenum Publishers, 2004.

[2] S. Sun, C. B. Murray, D. Weller, L. Folks, and A. Moser, Science **287,** 1989 (2000).

[3] R.C. O'Handley, Modern Magnetic Materials: Principles and Applications, John Wiley & Sons, Inc. 2000.

[4] G. Xiao, and C.L. Chien, Appl. Phys. Lett. **51**,1280 (1987).

[5] K. S. Buchanan, Ph.D. thesis, University of Alberta (2004).

[6] C.P. Bean and J.D. Livingston, J. Appl. Phys. **30**,120s (1959).

[7] M. Respaud, J. M. Broto, H. Rakoto, and A. R. Fert, L. Thomas and B. Barbara, M. Verelst, E. Snoeck, P. Lecante, and A. Mosset, J. Osuna, T. Ould Ely, C. Amiens, and B. Chaudret, Phys. Rev. B **57**, 2925 (1998).

[8] S.H. Liu, and C.L. Chien, Appl. Phys. Lett. **50**, 512 (1988).

[9] S. Sahoo, O. Petracic, W. Kleemanna, S. Stappert, G. Dumpich, P. Nordblad, S. Cardoso, and P. P. Freitas, Appl. Phys. Lett. **82**, 4116 (2003).

[10] Y. K. Takahashi, T. Koyama, M. Ohnuma, T. Ohkubo, and K. Hono, J. Appl. Phys. **95**, 2690 (2004).

[11] X. Chen, S. Sahoo, W. Kleemann, S. Cardoso, and P. P. Freitas, Phys. Rev. B **70**, 172411 (2004).

[12] S. Honda, F. A. Modine, A. Meldrum, J. D. Budai, T. E. Haynes, and L. A. Boatner, Appl. Phys. Lett. **77**, 711 (2000).

[13] K.S. Buchanan, X. Zhu, A. Meldrum, M.R. Freeman, Nano Lett. **5**, 383 (2005).

[14] E. Carpenter, J. Sims, J. Wienmann, W. Zhou, and C. J. O'Conner, J. Appl. Phys. **87**, 5615 (2000).

[15] S. Cho, J. Idrobo, J. Olamit, K. Liu, N.D. Browning, and S.M. Kauzlarich, Chem. Mater. **17**, 3181 (2005)

[16] K.S. Buchanan, A. Krichevsky, M.R. Freeman, and A. Meldrum, Phys. Rev. B **70**, 174436 (2004).

[17] D. Farrell, Y. Cheng, R. William McCallum, M Sachan, and S. A. Majetich J. Phys. Chem. B **109**, 13409 (2005).

[18] C. A. Ross, Annu. Rev. Mater. Res. **31**, 203 (2001).

[19] J.Y. Cheng, C. A. Ross, E.L. Thomas, H.I. Smith, and G.J. Vancso, Adv. Mater. **15**, 1599 (2003).

[20] S. Sun, and H. Zeng, J. Am. Chem. Soc. **124**, 8204 (2002).

[21] S. Cho, A.M. Shahin, G.J. Long, J.E. Davies, K. Liu, F. Grandjean, and S.M. Kauzlarich, Chem. Mater. **18**, 960 (2006).

[22] B. Ravel, E. E. Carpenter, and V. G. Harris, J. Appl. Phys. **91**, 8195 (2002).

[23] S. Cho, S.M. Kauzlarich, J. Olamit, K. Liu, F. Grandjean, L. Rebbouh, and G.J. Long, J. Appl. Phys. **95**, 6804 (2004).

[24] F. Wang, R. Egerton, and M. Malac, Ultramicroscopy **106**, 925 (2006).

[25] F. Wang, M. Malac, and R.F. Egerton. Micron, (in press).

[26] L. Signorini, L. Pasquini, L. Savini, R. Carboni, F. Boscherini,E. Bonetti, A. Giglia, M. Pedio, N. Mahne, and S. Nannarone, Phys. Rev. B **68**, 195423 (2003).

[27] R.F. Egerton, Electron Energy-Loss Spectroscopy in the Electron Microscopy, 2nd ed., New York: Plenum Press, 1996.

[28] C.Colliex, T. Manoubi, and C. Ortiz, Phys. Rev. B **44**, 11402 (1991).

[29] T. Riedl, T. Gemming, K. Wetzig, Ultramicroscopy **106**, 284 (2006).

[30] F. Wang, M. Malac and R. Egerton, Micron **37**, 316-323 (2006).

[31] X. Zhu, K.S. Buchanan, C. Blois, Z. Liu, A. Meldrum, and M.R. Freeman, J. Appl. Phys. **97**, 10A720 (2005).

[32] C. Chen, O. Kitakami, and Y. Shimada, J. Appl. Phys. **84**, 2184 (1998).

[33] C. Baker, S.K. Hasanain, and S.I. Shah, J. Appl. Phys. **96**, 6657 (2004).

[34] A.N. Dobrynin, D.N. Levlev, K. Temst, P. Lievens, J. Margueritat, J. Gonzalo, C.N. Afonso, S.Q. Zhou, A. Vantomme, E. Piscopiello, and G.Van. Tendeloo, Appl. Phys. Lett. **87**, 12501 (2005).

[35] F. Bødker, S. Mørup, and S. Linderoth, Phys. Rev. Lett. **72**, 282 (1994).

[36] H. Pfeiffer, Phys. Status Solidi A **118**, 295 (1990).

[37] T.C. Schulthess, M. Benakli, P.b. Visscher, T.d. Sorge, J.R. Thompson, F.A. Mondine, T.E.Havnes, L.A. Boatner, G.M. Stocks, and W.H. butler, J. Appl. Phys. **89**, 7594 (2001).

Chapter 5 Alternative methods of identifying the oxidation of metallic nanoparticles embedded in a matrix

(F. Wang, M. Malac, R.F. Egerton. Micron, in press)

5.1 Introduction

For a nanocomposite system, such as metallic nanoparticles in an insulating matrix, microstructural analysis is critical for understanding the physical properties. In particular, atoms at a surface or interface, often oxidized or bonded to the matrix material, can have a greatly different phase state than atoms away from the interface. Electron and x-ray diffraction are ideal for identifying the crystallographic structure of materials but provide only average properties, making it difficult to detect local changes. High-resolution TEM and scanning TEM (STEM) show the crystal structure on an atomic level but the chemical state of species at the nanoparticle-matrix interface can be difficult to deduce (Moltaji et al., 2000). Therefore it is important to develop convenient methods for characterizing the properties of a particle-matrix interfacial layer, such as its oxidation state, as an aid to interpret other physical properties.

Energy-loss near-edge structure (ELNES) provides information on the local environment of excited atoms, such as the coordination, valence and chemical bonding in nanostructures, for example by comparison to known fingerprint spectra (Egerton, 1996). A real-space multiple-scattering (RSMS) calculation of ELNES is based on the propagation of excited electrons through clusters of atoms without the requirement of periodicity, allowing the structural origins of particular features in the ELNES to be determined (Ankudinov et al., 1998; Rehr and Albers, 2000). Such calculations can help us to develop more reliable and better-understood fingerprints for identifying local crystallographic structure and improve our understanding of local chemical bonding.

The white-line ratio (WLR), a measure of the 3d-orbital occupancy, is widely used to evaluate the valence state of transition metals (TMs) (Egerton, 1996; Pease et al., 2001; Riedl et al., 2006; Wang et al., 2000). Here we discuss two alternative methods: observation of a "prepeak" (a sharp pre-edge peak in the O-K edge) and a "postpeak" (a broad post-edge peak beyond the L-edge). According to RSMS calculation, their appearance is correlated with oxidation of the TMs, and they have practical advantages for identifying the local electronic structure, for example in the interface for metallic nanoparticles embedded in a matrix.

A characteristic pre-edge peak (prepeak) appears in the O-K edge when oxygen atoms are chemically bonded to 3d transition metals (Colliex et al., 1991; de Groot et al., 1989; Wu et al., 1997). For metallic nanoparticles in an oxide-rich matrix such as silica, an oxygen K-edge can arise from the matrix or from oxidation of the metal, whereas the presence of a prepeak in the O-K edge is characteristic of the TM oxides. A postpeak in the 3d transition metal L-shell ELNES appears upon oxidization of TMs, as demonstrated in our own experiments (Wang et al., 2006_a) and by reference to data in the EELS Atlas (Ahn et al., 1983). RSMS calculations using clusters of increasing size established that the postpeak originates from photoelectron backscattering by the nearest-neighbor oxygen atoms, so it provides a clear indication of the presence of oxygen in the near vicinity of TM atoms. The method is very sensitive, even a slight amount of oxidation results in a detectable postpeak. The application of these techniques will now be demonstrated by detecting the oxidation of iron nanoparticles that are embedded in a SiO_2 matrix.

5.2 Experimental methods

Iron nanoparticles embedded in silica (so-called Fe-SiO_2 nanocomposites) were fabricated by depositing multilayers of Fe/SiO_2 films onto 5 nm-thick carbon in an ultra-high vacuum (UHV) system. The deposited films were annealed *in-situ*, resulting in well-defined iron nanoparticles within the SiO_2 matrix (Wang et al., submitted). Through this procedure, particle size can be controlled by adjusting the iron layer thickness. We fabricated six samples with iron nanoparticles of different average diameters: 3.2±0.7,

7.4±2.2, 8.0±1.8, 10.6±2.9, 15.7±5.1, 21.1±7.7 nm, each size measurement coming from the analysis of 300 to 400 nanoparticles in a bright-field TEM image. For comparison, another three films were deposited onto 5 nm-thick carbon in the UHV system. One is a 15 nm-thick SiO_2 film (without inclusion of iron); two others are iron films of different thickness, namely, 15 nm and 3 nm, that were both buffered and capped with 4 nm-thick SiO_2 layers. The 3 nm-thick film was then annealed in air at above 720 °C for 3 hours, resulting in extensive oxidation, as confirmed by electron diffraction (not shown here).

The morphology of the as-grown samples was examined by plan-view TEM imaging, using a 200 kV LaB_6 instrument (JEOL 2010), and by high-angle annular-dark-field (HAADF) microscopy of individual nanoparticles, using a Hitachi HD 2300 scanning-transmission electron microscope (STEM) equipped with a cold field emission gun (CFEG). All the core-loss electron energy-loss spectroscopy (EELS) spectra were recorded using a Gatan 666 parallel-EELS spectrometer, from a number of particles of similar size over an area of about one square micrometer. The spectra were collected in TEM diffraction mode (image-coupled spectrometer) with a collection semi-angle of 0.6 mrad and energy dispersion of 0.2 eV/channel. The energy resolution (measured as the full-width at half-maximum of the zero-loss peak) was 1.2 eV. The pre-edge background was subtracted as a power law and multiple scatterning removed by Fourier-ratio deconvolution (Egerton, 1996).

Real-space multiple-scattering (RSMS) calculations were performed for the iron L-edge of Fe (α-phase), FeO (wüstite) and Fe_2O_3 (hematite), and for the oxygen K-edge for SiO_2 (α-quartz), FeO and Fe_2O_3, using the crystal structures in Wyckoff (1963). We used the FEFF 8.2 code with its implemented full multiple-scattering (FMS) and self-consistent-field (SCF) cards (Ankudinov et al., 1998). Hedin-Lundqvist self-energy was used to account for the inelastic losses. A sequence of near-edge structure calculations were made by adding successive shells about the central excited atom, in order to ascertain the contributions from different shells. Energy shifts and Gaussian broadenings were added in matching the measured edge onsets and energy resolution.

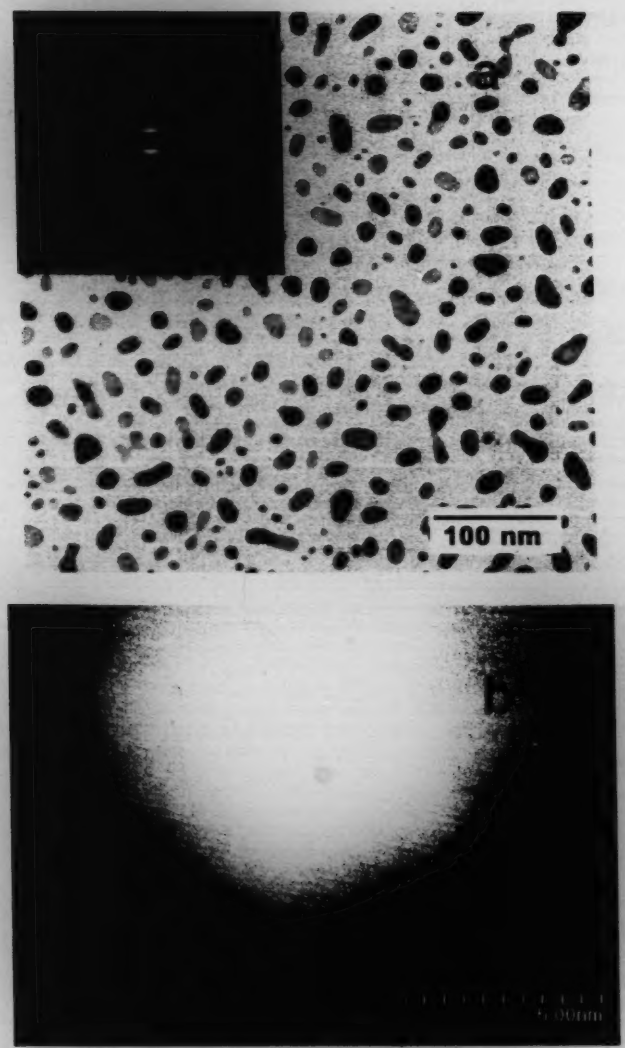

Figure 5-1(a) Bright-field TEM image of iron nanoparticles embedded in silica matrix; (b) High-angle annular dark field (HAADF) image for a single iron nanoparticle, recorded in a Hitachi HD 2300 STEM. (Courtesy of Drs. Koji Kimoto and Kuniyasu Nakamura.

5.3 Results

5.3.1 Imaging

Figure 5-1 (a) shows a bright-field TEM image for a typical Fe-SiO_2 nanocomposite film: iron nanoparticles (darker regions) are evenly distributed in the SiO_2 matrix (lighter

regions), and they are well separated from each other. Based on the diffraction pattern (shown in the inset), bcc-Fe is clearly the predominant phase; diffraction rings associated with iron oxide phases were rarely observed.

A high-angle annular dark-field (HAADF) image recorded for a single Fe nanoparticle is shown in Fig. 5-1(b). It is clear that the iron particle (with a diameter of about 12 nm) is crystalline and the interface between the nanoparticle and the SiO_2 matrix is very sharp; the Fe lattice continues to the edge of the nanoparticle, suggesting little oxide has been formed. However, some oxidization of the particle surface is expected in consideration of the high chemical reactivity of iron.

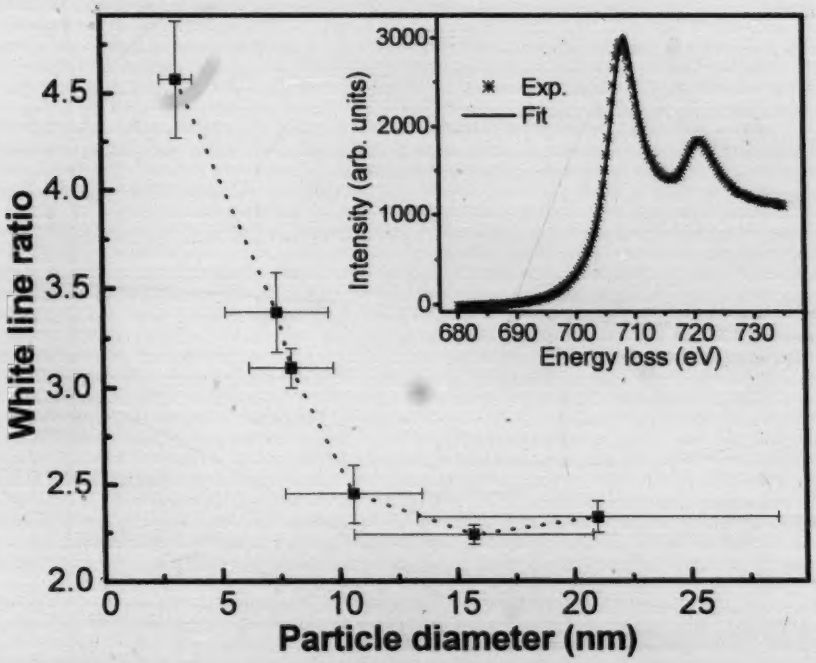

Figure 5-2: A variation of the white line ratio (WLR) as a function of particle diameter, measurement errors in the particle diameter and WLR are also shown. Inset is Fe-L_{23} edge for a typical sample (with average particle diameter of 10.6nm) and the fitted curve.

5.3.2 White line ratio

The white line ratio (WLR) is sensitive to the change in the valence state of the transition metals and their oxides, showing a systematic variation with oxidation state; for the case of iron, the ratio increases with increase of the extent of oxidation (Colliex et al., 1991; Pease et al., 2001; Wang et al., 2000; Wallis et al., 1996). At the L_{23} edges, white-line

peaks correspond to excitations of 2p electrons to bound 3d states near the Fermi level; their separation arises from spin-orbit splitting. The experimental data can be fitted to two Lorentzians representing the white lines and two arctangent functions accounting for continuum background from core-to-continuum transition (Pease et al., 2001). Through a standard fitting procedure, one can separate the white lines from the continuum background and isolate the L2 and L3 lines from each other (Wang et al., 2006-b). It is important to recognize a constraint coming from the fact that L_2 width must exceed the L_3 width, owing to the possibility of Coster-Kronig transitions (Pease et al., 2001). We performed fittings to the iron L-edges for the six samples of different particle size and obtained a good match to the experimental data. In the inset of Figure 5-2, a typical fitting to the experimental Fe-L_{23} edges is shown, for a sample with an average particle diameter of 10.6 nm. The intensities of the white lines were taken as integrated intensities under the fitted Lorentzians.

Figure 5-2 shows the dependence of white-line ratio on the particle diameter. It appears that serious oxidation has occurred in the small iron nanoparticles, as reflected by their high WLR values, and as might be expected from the high chemical activity of iron (Wang et al., submitted). Only slight oxidation is evident in the samples with larger nanoparticles, as indicated by their reduced WLR values. This result is consistent with the HAADF TEM image shown in Fig. 5-1 (b).

5.3.3 Prepeak

When oxygen atoms are chemically bonded to 3d transition metals (TMs), a characteristic pre-edge peak appears in the O-K edge. It has been investigated experimentally and theoretically (de Groot et al., 1989; Colliex et al., 1991; Wu et al., 1997). This prepeak, located about 3eV below the O-K threshold, is believed to correspond to 1s → 2p transitions toward the oxygen 2p states hybridized with 3d transition-metal orbitals (de Groot et al., 1989; Wu et al., 1997). By multiple scattering calculation, we will show that the prepeak is very sensitive to the presence of TM oxides.

Figure 5-3(a) shows the calculated near-edge fine structure of the oxygen K-edge for SiO_2 (α-quartz), FeO (wüstite) and Fe_2O_3 (hematite). A prominent prepeak is present in FeO and Fe_2O_3, but not in SiO_2. In particular, this feature already shows up in a small

cluster of 5 atoms for Fe_2O_3 and 7 atoms for FeO, with a central oxygen atom surrounded by nearest-neighbour iron atoms.

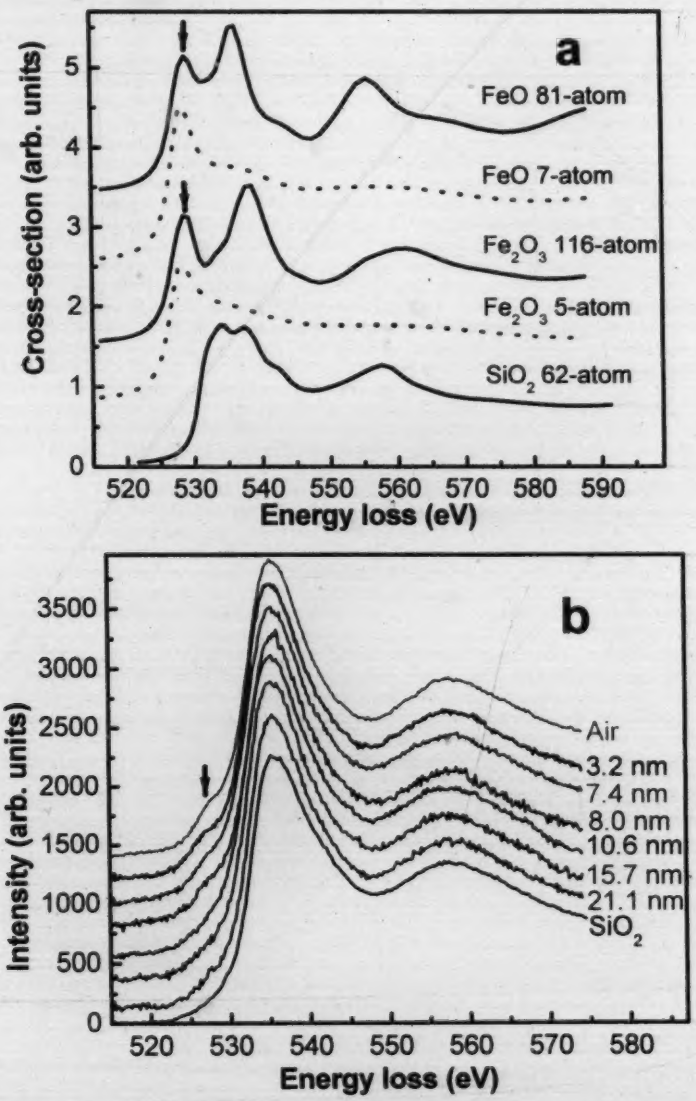

Figure 5-3 (a) Calculations of the O Kedges for SiO_2 (of 62-atom cluster), Fe_2O_3(of 5-and 116-atom clusters) and FeO (of 7- and 81-atom clusters). The prepeaks are marked by arrows. (b) Experimental O K-edges for the six Fe-SiO_2 nanocomposite films (labeled by the average particle diameter) together with that of the sample annealed in air and SiO_2 film. The prepeak position is marked by an arrow.

The very appearance of an oxygen K-edge provides a direct indication of oxidation of the transition metal, but only if it is separated sufficiently from other media containing oxygen. For the iron nanoparticles embedded in SiO_2 shown in Figure 5-1, the

oxygen K-edge can also arise from the SiO_2 matrix. However, the multiple-scattering calculations above established that a prepeak appears only in iron oxides, even for a very small cluster (central O atom plus the first shell of Fe atoms) and not in SiO_2; thus the oxidation of the iron nanoparticles is still detectable using the characteristic prepeak.

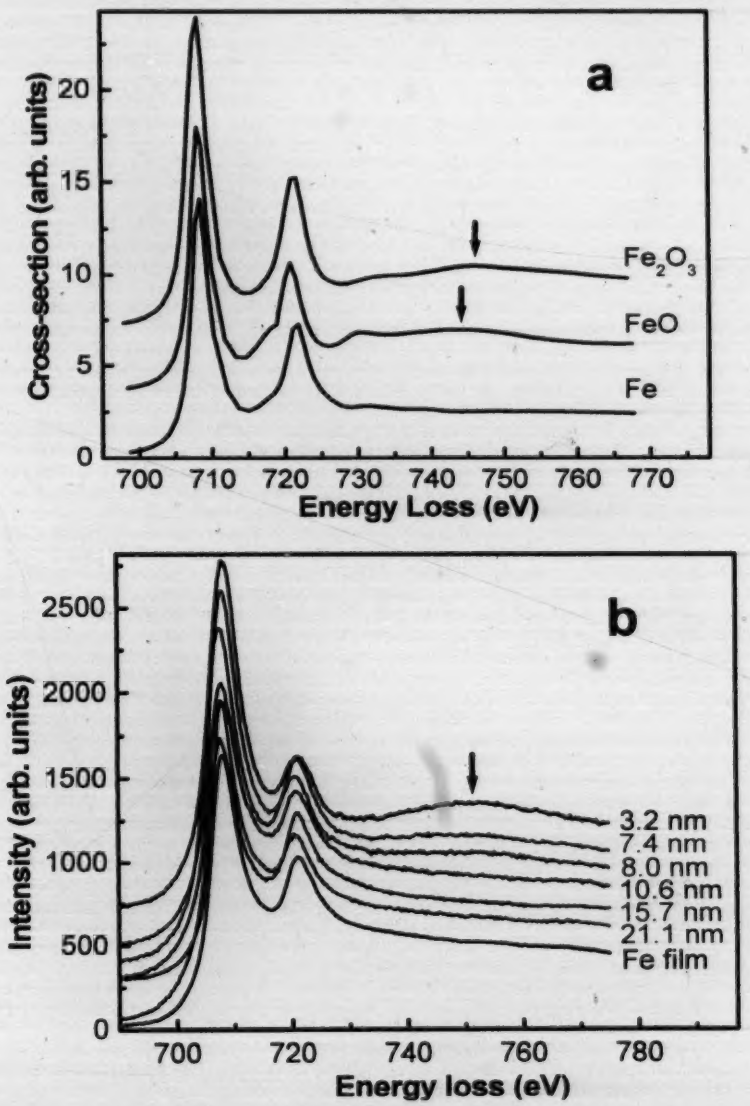

Figure 5-4 (a) Calculated iron L_{23} edges for Fe, FeO and Fe_2O_3, for cluster sizes of 65, 57 and 75 atoms respectively. The postpeak positions are marked by arrows. (b) Experimental iron L-edges for the six Fe-SiO_2 nanocomposite films (labeled by the average particle diameter), showing a size dependent postpeak marked by an arrow. The iron L-edge for a continuous 15nm-thick Fe film was also shown for comparison.

Figure 5-3 (b) shows oxygen K-edges for the six Fe-SiO_2 nanocomposites (labeled with the average particle diameter), together with that of the iron/SiO_2 multilayer annealed in air (labeled as Air) and a SiO_2 film for a comparison. RSMS calculation (on a cluster of 62 atoms) reproduced the oxygen K-edge for SiO_2 film well, showing similar features in peak shapes and positions. However, the prominent prepeak (marked by an arrow), distinctively appearing in the oxygen K-edge of the sample annealed in air, was not shown in the experimental or calculated results for a SiO_2 film.

The prepeak feature is very obvious in Fe-SiO_2 nanocomposite films containing smaller iron nanoparticles but is hardly seen in the samples with larger nanoparticles (diameter above10 nm). Clearly the prepeak amplitude decreases with increase in particle size. This comparison not only clarifies the cause of the prepeak, namely the oxidation during annealing, but demonstrates a variation of the extent of the oxidation with particle size. We obtained very similar results from the WLR method, as shown in Figure 5-2. However it is interesting to note that, although the oxygen K-edge comes predominately from SiO_2 matrix, the slight surface oxidation on the Fe nanoparticles is detectable from the appearance of a prepeak.

5.3.4 Postpeak

A broad post-edge peak (postpeak) in the core-loss spectrum is often attributed to plural scattering of the transmitted electrons, involving a core loss and a bulk plasmon (Egerton, 1996). However, we recently found that a prominent postpeak occurs at about 40 eV beyond the iron L_3-edge, even in very thin films of iron oxides and fluorides, and not in films of pure iron. This peak appears to be characteristic of iron in an oxidized state (Wang et al., 2006-a). To clarify the origin of the pospteak, we performed RSMS calculations of the near-edge fine structure of the Fe L_2 and L_3 edges for Fe, FeO and Fe_2O_3. Figure 5-4 (a) shows the white lines obtained by algebraic sum of the calculated L_3 and L_2 components, weighted according to their scattering cross sections. The postpeaks are well reproduced in FeO and Fe_2O_3, as indicated by the arrows. RSMS calculations as a function of cluster size (not shown here) suggested that the postpeak

arises from the backscattering of nearest-neighbor oxygen atoms. Therefore even a slight amount of oxidation should result in the appearance of a postpeak.

Figure 5-4(b) shows the iron L-edges for samples with iron nanoparticles of different average sizes and for a 15 nm-thick continuous bcc-iron film. The postpeaks are broad and are located about 40eV above the Fe-L_3 edge, agreeing with the calculation in Fig. 5-4 (a). Size-dependent oxidation is demonstrated by the decrease of the postpeak with the increase of the particle size, and its absence in the iron film. From the strong presence of metallic bcc-Fe in the diffraction pattern, together with the HAADF image of Fig. 5-1 and the limited presence of the post-edge peak, we deduce that the volume of iron oxide is small compared to that of bcc Fe. We would expect any oxide to be predominantly on the particle surface.

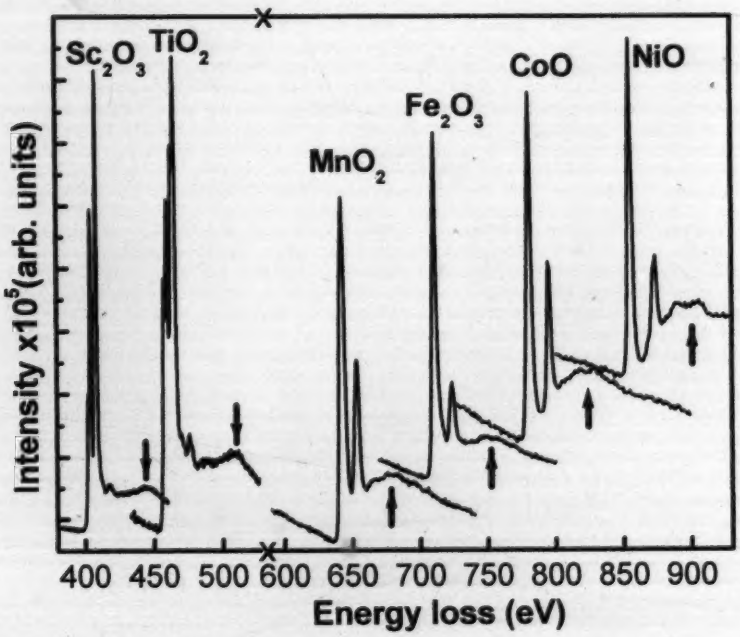

Figure 5-5 L_{23} edges of transition metal oxides, reproduced from EELS Atlas. The postpeak positions are marked by arrows.

5.4 Discussion

The white-line ratio has been widely used in characterizing the oxidization state of transition metals (Pease et al., 2001; Riedl et al., 2006) but involves considerable effort in

spectral processing and fitting. Moreover, the results obtained using different processing procedures are not always consistent (Riedl et al., 2006). If, as suggested above, a correlation between the prepeak or postpeak and the presence of metal oxides is a general effect, these peaks could act as a useful characteristic feature for identifying oxides of all transition metals and their compounds.

In fact, a prepeak arising from the covalent mixing of metal and oxygen states appears to be a general feature of the oxygen K-edge of the transition metal oxides (de Groot et al., 1989). Also, a postpeak is visible in published spectra of various transition-metal oxides (Leapman et al., 1982). Figure 5-5 shows experimental data for Sc_2O_3, TiO_2, MnO_2, Fe_2O_3, CoO and NiO, reproduced from EELS Atlas (Ahn et al., 1983); the postpeak can be found in all of the these oxides, although at slightly different positions, as indicated by the arrows.

Nowadays there is increased interest in valence state determination at high spatial resolution, due to greater access to (S)TEMs equipped with cold field emission guns. In this case, an electron probe can be focused locally on the interface to reduce matrix effects. When measuring at high spatial resolution, the obtainable edge intensities are relatively low and the exposure time is limited because of specimen drift and radiation damage, resulting in poor signal-to-noise ratio (SNR). As we have shown, a prepeak in the oxygen K-edge and postpeak in transition-metal L-edge arise from the chemical bonding to nearest-neighbour (TM or oxygen) atoms and are thus very localized. These factors favor the prepeak and postpeak techniques over the WLR approach, in combination with the high-resolution STEM imaging. Actually, it was already verified in our experiment that the prepeak and postpeak methods are highly sensitive to oxidation, despite the masking effect from a dominant volume of SiO_2 or iron, in a nanocomposite system.

In summary: we have demonstrated use of the prepeak and postpeak techniques as alternative ways to detect the oxidation of transition metals. These techniques provide a test of local valence-state change, such as at the interface in a metallic nanoparticles embedded in an insulting matrix, and are compatible with (S)TEM-EELS at high spatial resolution.

Acknowledgement

This work was supported by NRC and NSERC. The authors would like to thank Dr. Al Meldrum for help with sample preparation, Dr. Koji Kimoto (NIMS, Tsukuba) and Dr. Kuniyasu Nakamura (Hitachi High Technologies, Naka division) for access to Hitachi HD 2300 STEM and for help with STEM imaging, Dr. John Hunt (Gatan) and Dr. Channing Ahn (California Institute of Technology) for permission to reproduce Figure 5-5 from EELS Atlas. We are grateful for technical support of Don Mullin and Greg Popowich. FW wishes to acknowledge support from the Killam Trust.

References

Ahn, C.C., Krivanek, O.L., Brugner, R.P., Disko, M.M., and Swann, P.R., 1983. EELS Atlas. ASU HREM facility and Gatan Inc..

Ankudinov, A.L., Ravel, B., Rehr, J.J., and Conradson, S.D., 1998. Real space multiple scattering calculation and interpretation of X-ray absorption near edge structure. Phys. Rev. B 58, 7565-7576.

Colliex, C., Manoubi, T., and Ortiz, C., 1991. Electron-energy-loss-spectroscopy near-edge-fine structures in the iron-oxygen system, Phys. Rev. B 44, 11402-11411.

de Groot, F.M.F., Grioni, M., Fuggle, J.C., Ghijsen, J., Sawatzky, G.A., and Petersen, H., 1989. Oxygen 1s x-ray-absorption edges of transition-metal oxides. Phys. Rev. B 40, 5715-5723.

Egerton, R.F., 1996. Electron Energy-Loss Spectroscopy in the Electron Microscopy, 2nd ed., New York: Plenum Press.

Leapman, R.D., Grunes, L.A., Fejes, P.L., 1982. Study of the L23 edges in the 3d transition metals and their oxides by electron-energy-loss spectroscopy with comparisons to theory. Phys. Rev. B 26, 614–635.

Moltaji, H.O., Buban, J.P., Zaborac, J.A., Browning, N.D., 2000. Simulating the oxygen K-edge spectrum from grain boundaries in ceramic oxides using the multiple scattering methodology. Micron 31, 381-399.

Pease, D.M., Fasihuddin, A., Daniel, A. M. and Budnick, J.I., 2001. Method of linearizing the 3d L_3/L_2 white line ratio as a function of magnetic moment. Ultramicroscopy 88, 1-16.

Riedl, T., Gemming, T., Wetzig, K., 2006. Extraction of EELS white-line intensities of manganese compounds: Methods, accuracy, and valence sensitivity. Ultramicroscopy 106, 284-291.

Rehr, J.J., and Albers, R.C., 2000. Theoretical approaches to x-ray absorption fine structure. Rev. Mod. Phys. 72, 621-654.

Wallis, D.J., Browning, N.D., Megaridis, C.M., and Nellist, P.D., 1996. Analysis of nanometer-sized pyrogenic particles in the scanning transmission electron microscope. J. Microscopy 184, 185-194.

Wang, F., Egerton, R.F., and Malac, M., 2006_a. Interpretation of the postpeak in iron fluorides and oxides. Ultramicroscopy 106, 925-932.

Wang, F., Malac, M., and Egerton, R.F. 2006_b. Energy-loss near-edge fine structures of iron nanoparticles. Micron 37, 316-23.

Wang, F., Malac, Egerton, R.F., M., Meldrum, A., Zhu, X., Liu, Z., Macdonald, N., Li, P., and Freeman, M.R., submitted. Multilayer route to iron nanoparticle formation in an insulating matrix. J. Appl. Phys.

Wang, Z.L., J. Bentley, J., and Evans, N.D., 2000. Valence state mapping of cobalt and manganese using near-edge fine structures. Micron 31, 355-362.

Wu, Z.Y., Gota, S., Pollak, M., Gautier-Soyer, M., Ratoli, C.R., 1997. Chracterization of iron oxides by x-ray absorption at the oxygen K edge using a full multiple-scattering approach. Phys. Rev. B 55, 2570-2577

Wyckoff, R.G.W., 1963. Crystal Structures, 2nd ed. (Wiley, New York).

Chapter 6 Controlled growth of silicon oxide nanowires from a patterned reagent

(Feng Wang, Marek Malac, and Ray F. Egerton, A. Meldrum, Peng Li, and Mark R. Freeman, and Jonathan G. C. Veinot. J. Phys. Chem. C (Letter; in press))

Silicon-based nanowires, including crystalline and amorphous silicon and silicon oxide nanowires, have shown promising applications in nanoelectronics and integrated optic devices[1,2,3]. Synthetic methods including chemical vapor deposition,[4] laser ablation,[3] sol-gel,[5] and thermal evaporation,[6] have been used for random (*i.e.*, non-patterned) growth of nanowires (NWs). However, for many potential applications it is desirable to control the position and size of the NWs so that post-growth manipulation is not required.[7, 8] Recently, selective growth of silica NWs via a vapor-liquid-solid mechanism[9] was achieved using an ion implantation mask;[10] herein, we will show that much higher spatially resolved patterning (by several orders of magnitude) than the report could be achieved by employing electron beam lithography. The diameter of NWs is determined by the iron nanoparticles encapsulated at individual NWs, similar to other reports in Si and GaP nanowires;[11, 12] but in our case the NWs grow directly from a patterned reagent and the inflow of the Si-containing gas is required.

The fabrication procedure can be divided into three stages: i) formation of the Fe-SiO_2 nanocomposites (i.e. iron nanoparticles embedded in a SiO_2 matrix), ii) patterning of the reagent, and iii) the growth of the silicon oxide nanowires. Fe-SiO_2 nanocomposites were fabricated by electron-beam deposition of SiO_2 (purity: 99.999%) and Fe (99.95%) to form a SiO_2/Fe/SiO_2 trilayer on 50 nm-thick silicon nitride (Si_3N_4) membranes and annealed *in-situ* at 880°C, in an ultra-high vacuum (UHV) system with base pressure 10^{-10} Torr.[13] A 6 nm-thick carbon film was pre-coated on the Si_3N_4 membrane to suppress charging during electron beam lithography. Following fabrication of the Fe/SiO_2 composite, a 60 nm-thick layer of hydrogen silsesquioxane (HSQ: Fox17, Dow Corning, which is a well known negative planarizing electron beam resist) was spin-

coated onto the sample surface. An array of circular dots of a 50 nm diameter separated by 1 μm was patterned in the HSQ layer using a Raith 150 electron-beam lithography system. Areas of the Fe/SiO_2 nanocomposite not protected by the exposed HSQ were subsequently removed by dry etching in an argon ion mill, leaving the Fe/SiO_2 nanocomposite film only in areas under the exposed HSQ dots. The samples were finally annealed for one hour at 900°C in a slight overpressure of N_2/H_2 (95%/5%) forming gas. Microstructural and chemical investigations were carried out in an analytical transmission electron microscope (TEM, JEOL 2010), using bright-field imaging, electron energy-loss spectroscopy (EELS) and energy-loss near-edge structures (ELNES).

An array of circular nanodots of 50 nm diameter and 1 μm spacing, is shown in Figure 6-1 (a). A limited number of iron nanoparticles (typically less than 5) are present within each nanodot (see, in the inset of Fig 6-1(a)); Figure 6-1 (b) shows a TEM image of an array of NWs grown from the patterned nanodots. Iron nanoparticles are present at the end of NWs, which grew only from the original patterned HSQ/Fe nanodots, leaving the areas between the dots bare and completely free of NWs. The inset of Fig. 6-1 (b) shows NWs produced from a typical dot, with higher magnification.

Most of the nanowires have a length less than 1 μm, determined by the supply of the stock material. It is worth noting that the number of iron nanoparticles is determined by the size of each HSQ dot and the areal density of Fe nanoparticles. Therefore, it is expected that a suitable choice of Fe nanoparticle growth parameters and HSQ dot diameters can be used to control the number of iron nanoparticles per dot and consequently the number of NWs grown from each dot.

Using a thick Si_3N_4 membrane as substrate results in some difficulty in the TEM investigation; however, this problem was avoided by examining NWs that were suspended between gaps in the Si_3N_4 film, allowing microstructural and chemical analysis without influence from the substrate. Figure 6-2 shows a TEM image of a bundle of NWs protruding from the Si_3N_4 substrate. The nanowires have a smooth surface and a closed end containing a single iron particle. The nanowires have diameters of 10 - 30 nm, comparable to the diameter of the iron nanoparticles encapsulated at the nanowire tips. TEM imaging and diffuse rings in electron-diffraction pattern (not shown here) collected from a body of nanowires showed that the nanowires are non-crystalline. Indexing the

electron diffraction pattern collected from the particles at the end of the NWs (inset in Fig. 6-2) indicated that bcc-Fe is the main phase; no peaks associated with iron oxides were found.

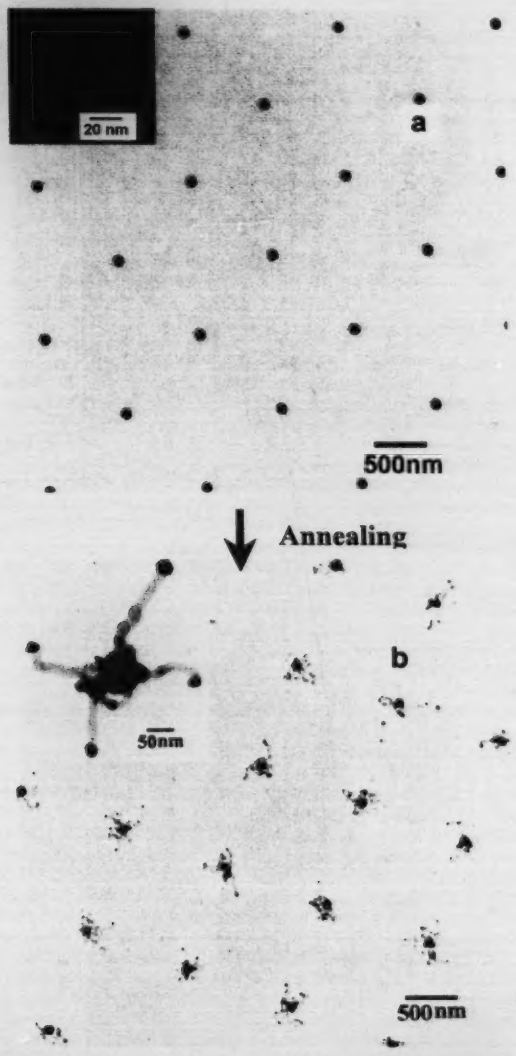

Figure 6-1 Bright-field TEM images for (a) arrays of iron nanoparticles after lithographic patterning, of 50 nm diameter and 1 um spacing (the inset shows one nanodot containing several nanoparticles), and (b) arrays of nanowires grown from the patterned nanodots (here the inset shows nanowires on a nanodot).

The diameters of individual nanowires and encapsulated nanoparticles are similar. 98 nanowires were measured from plan-view TEM images for a quantitative comparison. Figure 6-3 shows the size analysis of the nanowires as a function of the particle diameter. The solid line is a linear least square fit. The results suggest that the diameter of the

nanowires is predominantly determined by the iron nanoparticles, which leads to the possibility of synthesizing diameter-controlled silicon oxide nanowires. Control of Fe seed particle size has been demonstrated through a multiple-layer synthesis procedure.[13]

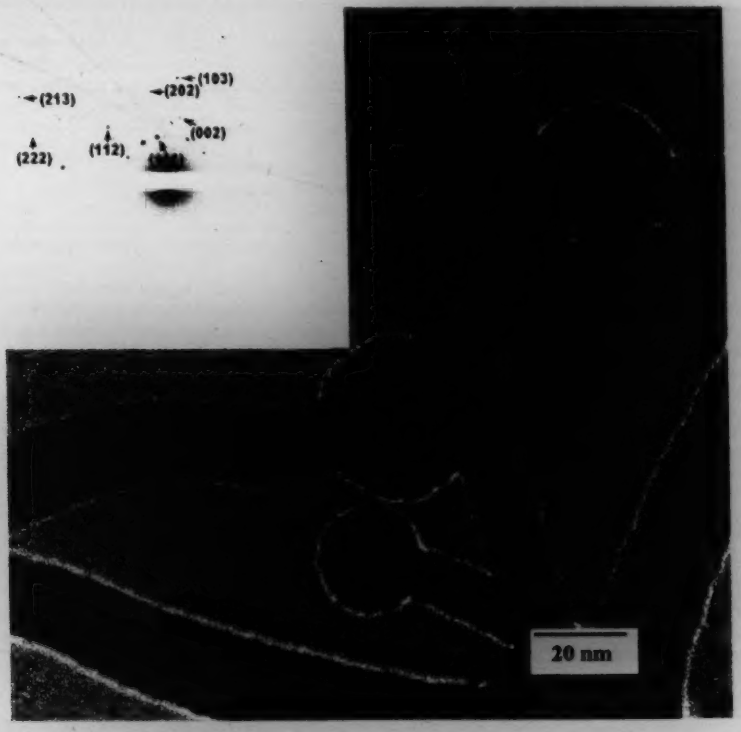

Figure 6-2 Bright-field TEM image of a bundle of individual nanowires projecting from the substrate, with iron nanoparticles encapsulated (darker region) at the NW tips. The insets are selected-area diffraction patterns of iron nanoparticles, which are consistent with the bcc-Fe phase.

Analysis of electron energy-loss (EELS) and Auger spectra showed that the nanowires are composed of silicon and oxygen. To further clarify the chemical environment of the silicon in the nanowires, the silicon L_{23} and oxygen K-ionization edges were measured from individual nanowires protruding from the substrate (shown in Figure 6-2). The Si L_{23}-edge shows a different fine structure than that recorded from nanowires on the Si_3N_4 substrate and no nitrogen K-edge was discerned in the energy loss spectra. The integral intensities of oxygen K and silicon L-edges allowed determination of the [O]:[Si] ratio, using O-K and Si-L ionization cross-sections calculated from SIGMAK3 and SIGMAL3 programs,[14, 15] and the resulting atomic [O]:[Si] ratio was 1.7±0.1. In addition, the near-edge fine structure of the silicon L_{23}-edge of SiO_2 and

elemental Si differ near the threshold energy,[16,17] negating the possibility that the wires contain elemental Si.

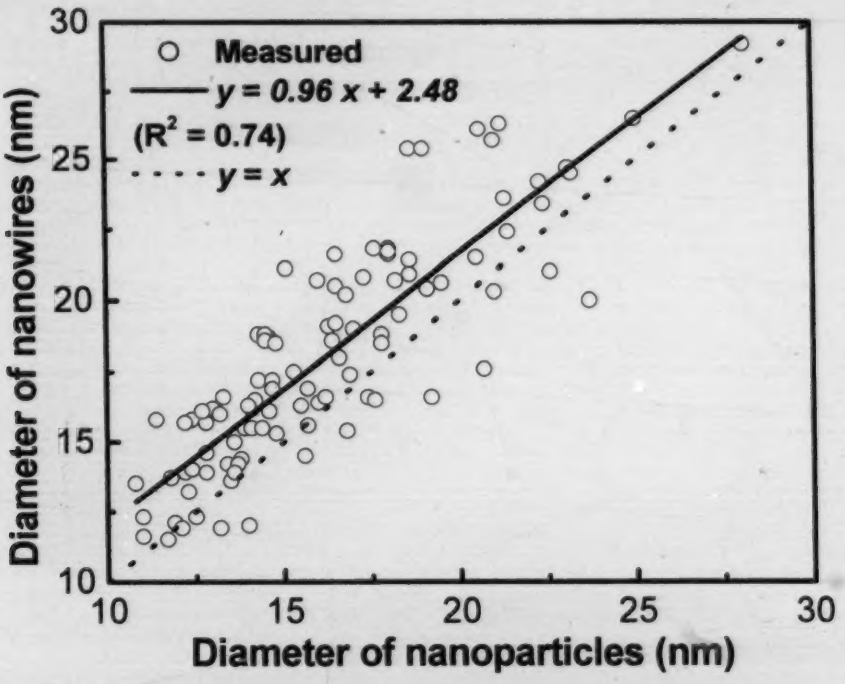

Figure 6-3 Dependence of the diameter of the nanowires on that of the encapsulated Fe particles. The solid line is a fit to the measured data: y = 0.96x + 2.48 (y: diameter of the nanowire; x: diameter of the nanoparticle (exclusive of the shell); the dotted line y = x is used for comparison.

The morphology of the NWs (with metal particles attached to the end) and the linear relation between the diameters of the nanowires and the encapsulated nanoparticles suggest the operation of a classical vapor-liquid-solid (VLS) growth mechanism.[9] Nevertheless no vapor source such as silane (SiH4) or other gaseous silicon compound was provided in the present growth process. Furthermore, the presence of liquid iron droplets, on which gaseous silicon precursor might produce silicon for the growth of nanowires,[2,9,11] is unlikely in this system because the annealing temperature used (900°C) was much lower than both the melting point of iron and the eutectic point for iron-silicon (i.e. $FeSi_2$),[18] even when the surface energy of the cluster is considered.[19,20] Therefore it is unlikely that the present nanowires grew by a VSL-like mechanism. The SLS (solid-liquid-solid) mechanism can also be excluded, in view of the top-growth mode and the low processing temperature in this growth process.[21]

Instead, NW growth could proceed via a direct solid-state transformation, similar to the mechanism proposed for the formation of amorphous silicon oxide nanowires grown from silica films; [22] a reduction layer, believed to induce the diffusion of silicon atoms being critical in the growth, becomes unnecessary in this case. Iron nanoparticles initially embedded in the SiO_2 layers of the underlying trilayer structure, diffuse to the surface when the sample was heated to 900°C. Similar diffusion through the reduction layer has been reported for nickel nanoparticles.[22] Fe particles at the exposed HSQ surface act as NW nucleation sites. NWs nucleate underneath the iron nanoparticles and grow by the diffusion of the Si atoms from the underlying exposed HSQ.

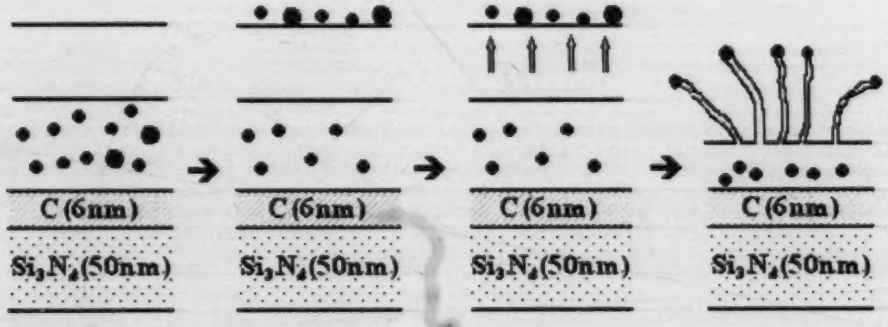

Figure 6-4 Proposed growth process of nanowires: (a) as-produced Fe-SiO_2 nanocomposites, with spin-coated HSQ on top; (b) migration of iron nanoparticles onto the top of the nanodots; (c) diffusion of Si atoms; (d) growth of nanowires onto the surface of nanodot.

Our proposed mechanism is summarized in Figure 6-4. HSQ is a well defined cage molecule with an empirical formula $(HSiO_{3/2})_n$. It has been reported, in the absence of conclusive structural characterization that upon exposure to electron-beam irradiation, some of the Si-H bonds are broken and an insoluble crosslinked siloxane network is formed. [23] This ill-defined, crosslinked network is expected to collapse upon annealing at 900 °C to form an "SiO_x-like" film containing regions rich in low valent Si. The diffusion and nucleation of oxide encapsulated, low valent Si at metal nanoparticles is known.[22, 24] In this regard, it is reasonable that the present "SiO_x-like" film, produced from annealing exposed HSQ, enhances the nucleation and one-dimensional growth of the silicon NWs, in a similar fashion to that proposed for "SiO" by Wang et al..[24] Accordingly, in the present system as-grown nanowires likely form as non-crystalline Si nanowires that subsequently oxidize rapidly to SiO_2 upon exposure to the ambient atmosphere.

In support of this proposed mechanism, control experiments using an Fe/SiO_2 nanocomposite with no overlaying exposed HSQ layer as well as with an Fe/SiO_2 nanocomposite bearing an unexposed HSQ film afforded no NWs, when annealed under identical conditions. These experiments clearly show that a crosslinked SiO_x-layer obtained from electron beam exposure of HSQ is crucial to the formation of the present NWs. At present, the exact role of the crosslinked HSQ remains unclear. Structural analysis of electron beam crosslinked HSQ films as well as an in-situ study of as-grown nanowire structure and chemical composition are expected to provide valuable information regarding the nanowire growth mechanism and are subject of further investigation in our laboratories.

In summary, a process for fabricating arrays of silicon oxide nanowires from a patterned reagent has been developed, in which the diameter of the nanowires depends on the nanoparticles attached at the end. Such an unusual growth process, being unexplainable by the VLS and SLS mechanisms, may be attributed to direct solid-state transformation.

Acknowledgements

This work was supported by *NRC, NSERC*. The electron beam lithographic patterning was made at Nanofab in the University of Alberta. The authors would like to thank Ken Bosnick for helpful discussion, Don Mullin, Greg Popowich for technical assistance. FW wishes to acknowledge support from the *Killam Trust*.

References

[1] B. Zheng, Y. Wu, P. Yang, and J. Liu, Adv. Mater. **14** (2002) 122.

[2] J.D. Carter, Y. Qu, R. Porter, L. Hoang, D.J. Masiel, and T. Guo, Chem. Commun., (2005) 2274.

[3] D. P. Yu, Q. L. Hang, Y. Ding, H. Z. Zhang, Z. G. Bai, J. J. Wang, Y. H. Zou, W. Qian, G. C. Xiong, and S. Q. Feng, Appl. Phys. Lett. **73** (1998) 3076.

[4] J. Q. Hu, Y. Jiang, X. M. Meng, C. S. Lee, and S. T. Lee, Chem. Phys. Lett. **367** (2003) 339.

[5] M. Zhang, Y. Bando, L. Wada, and K. Kurashima, J. Mater. Sci. Lett. **18** (1999)1911.

[6] C. H. Liang, L. D. Zhang, G. W. Meng, Y. W. Wang, and Z. Q. Chu, J. Non-Cryst. Solids **277** (2000) 63.

[7] R.S. Friedman, M.C. McAlpine, D.S. Ricketts, D. Ham, and C.M. Lieber, Nature **434** (2005) 1085.

[8] Q. Gu, H. Dan, J. Cao, J. Zhao, and S. Fan, Appl. Phys. Lett. **76** (2000) 3020.

[9] R.S. Wagner, and W.c. Ellis, Appl. Phys. Lett. **4** (1964) 89.

[10] D.K. Sood, P.K. Sekhar, and S. Bhansali, Appl. Phys. Lett., **88** (2006) 143110.

[11] Y. Cui, L.J. Lauhon, M.S. Gudiksen, and J. Wang, Appl. Phys. Lett. **78** (2001) 2214.

[12] M.S. Gudiksen and C.M. Lieber, J. Am. Chem. Soc. **122** (2000) 8801.

[13] F. Wang, M. Malac, R.F. Egerton, A. Meldrum, X. Zhu, Z, Liu, N. Macdonald, P. Li, and M.R. Freeman, submitted to J. Appl. Phys.

[14] R.F. Egerton, Electron Energy-Loss Spectroscopy in the Electron Microscope, 2nd edition, Plenum Press, New York (1996).

[15] The calculations are based on the formula: $\frac{[O]}{[Si]} = \frac{I_O(\beta,\Delta)}{I_{Si}(\beta,\Delta)} \frac{\sigma_{Si}(\beta,\Delta)}{\sigma_O(\beta,\Delta)}$, in which $I_o(\beta,\Delta)$ and $I_{Si}(\beta,\Delta)$ are experimentally obtained integral intensities of O K-edge and Si L-edge respectively, using window with Δ = 100 eV, and semi-collection angle β =3.0mrad; $\sigma_O(\beta,\Delta)$ and $\sigma_{Si}(\beta,\Delta)$ are cross-sections of O K-edge and Si L-edge respectively, calculated using SIGMAK3 and SIGMAL3 programs.

[16] G.A. Botton, J.A. Gupta, D. Landheer, J.P. McCaffrey, G.I. Sproule, and M.J. Graham, J. Appl. Phys. **91** (2002) 2921.

[17] P.E. Batson, Microsc. Microanal. Microstruct. **2** (1991) 395.

[18] Binary alloy phase diagrams, edited by B.M. Thaddeus, Massalski, H. Okamoto, P.R. Subramanian, and L. Kacprzak. Materials Park, Ohio: ASM International. 2nd edition, (1990).

[19] G.L. Allen, R.A. Bayles, W.W. Gile, and W.A. Jesser, Thin Solid film, **144**(1986)297.

[20] K.K. Nanda, S.N. Sahu, and S.N. Behera, Phys. Rev. A, **66** (2002) 13208.

[21] H.F. Yan, Y.J. Xing, Q.L. Hang, D.P. Yu, Y.P. Wang, J. Xu, Z.H. Xi, S.Q. Feng, Chemical Physics Letters **323** (2000) 224.

[22] K.H. Lee, H.S. Yang, K.H. Baik, J. Bang, R.R. Vanfleet, W. Sigmund, Chemical Physics Letters **383** (2004) 380.

[23] H. Namatsu, I. Yamaguchi, M. Nagase, K. Yamazaki, and K. Kurihara, Microelectronic Engineering **41/42** (1998) 331.

[24] N. Wang, Y.H. Tang, Y.F. Zhang, C.S. Lee and S.T, Lee, Phys. Rev. B **58** (1998) R16024.

Chapter 7 An ELNES study of silicon oxide nanowires grown from a patterned reagent

(*F. Wang*, M. Malac, R.F. Egerton, P. Li, A. Meldrum and M.R. Freeman. Microsc. Microanal. 12 supp 2 (2006) 1172)

7.1 Introduction

As one of the most important photoluminescence materials, silica (SiO_2) has been widely used in the electronics industry. Silicon-based nanowires, including crystalline and amorphous silicon and silicon oxide nanowires, have shown promising applications in nanoelectronics and optical devices[1,2,3]. Recently we developed a new process for fabricating silica nanowires, in which the selective growth of the nanowires is achieved through the incorporation of an electron-beam lithography (EBL) technique. In the process, hydrogen silsesquioxane (HSQ) is used as a high-resolution electron resist and its exposed product becomes the feedstock for growth of the nanowires in the presence of iron nanoparticles which is initially embedded in a silica matrix.

Yu et al., showed that amorphous silica NWs emit strong blue light and might hence be applied in integrated optical devices;[3] while several emission bands, of different emission characteristics depending on the composition and disorders of the silica nanowires, were also recently reported.[4, 5, 6, 7] Generally, it is believed that the blue bands of amorphous silicon oxide NWs are caused by the oxygen deficiency and the green bands are dominated by the SiO_4 tetrahedron. The emission intensity of the blue bands and green bands are complementary to each other, depending on the oxygen concentration: oxygen supplies diminish oxygen vacancies (thus decreasing the intensity of blue bands), and increase the SiO_4 tetrahedron (thus increase the intensity of the blue bands); and vice-versa.[6]

ELNES (energy loss near-edge structures) is sensitive to the local structure and chemical order.[8] Much work has been done on studying the structural and electronic

properties of silicon or silica films (e.g. in [9], [10], [11]), of direct relevance to their application in industry. We have used ELNES of the silicon-L and oxygen-K edges to study the structural state of the NWs, and ELNES of the Fe-L edge to study the chemical state of the iron nanoparticles at the tips, in promoting the understand to the growth mechanism and its optical properties.

7.2 Experiments

Silicon oxide nanowires were grown from a patterned reagent. Simply stated, stable iron nanoparticles embedded in SiO_2 matrix are grown onto Si_3N_4 membranes in an ultra-high vacuum system. The composite samples are then patterned and etched, using hydrogen silsesquioxane (HSQ) negative-tone resist, giving regular arrays of HSQ (exposed) nanodots covering the Fe-SiO_2 composite film. In the presence of Fe particles, nanowires are grown from the patterned nanodots by annealing in a furnace reactor in a N_2/H_2 atmosphere.

Microstructural and chemical investigations were carried out in an analytical transmission electron microscope (TEM, JEOL-2010) by bright-field (BF) imaging, electron energy-loss spectroscopy (EELS) and fine-structure (ELNES) analysis. The core-loss spectra of the iron L-edge, silicon L-edge and oxygen K-edge were collected in TEM diffraction mode (image-coupled spectrometer) with a collection semi-angle of 3.0 mrad and energy dispersion of 0.2 eV/channel. All the images and EELS spectra were collected from NWs suspended in the air, avoiding substrate influence. For a comparison, we also deposited a 15 nm-thick silicon dioxide film and recorded the spectra of its silicon L- and oxygen K-edges.

Real-space multiple-scattering (RSMS) calculations of the silicon L-edge and oxygen K-edge near-edge structure were performed for crystalline silicon dioxide SiO_2 (α-quartz)[12] using the FEFF 8.2 code with its full multiple scattering (FMS) and self-consistent field (SCF) cards implemented.[13] A sequence of near-edge structure calculations was made by adding successive shells about the central excited atom, in order to ascertain the contributions from different shells.

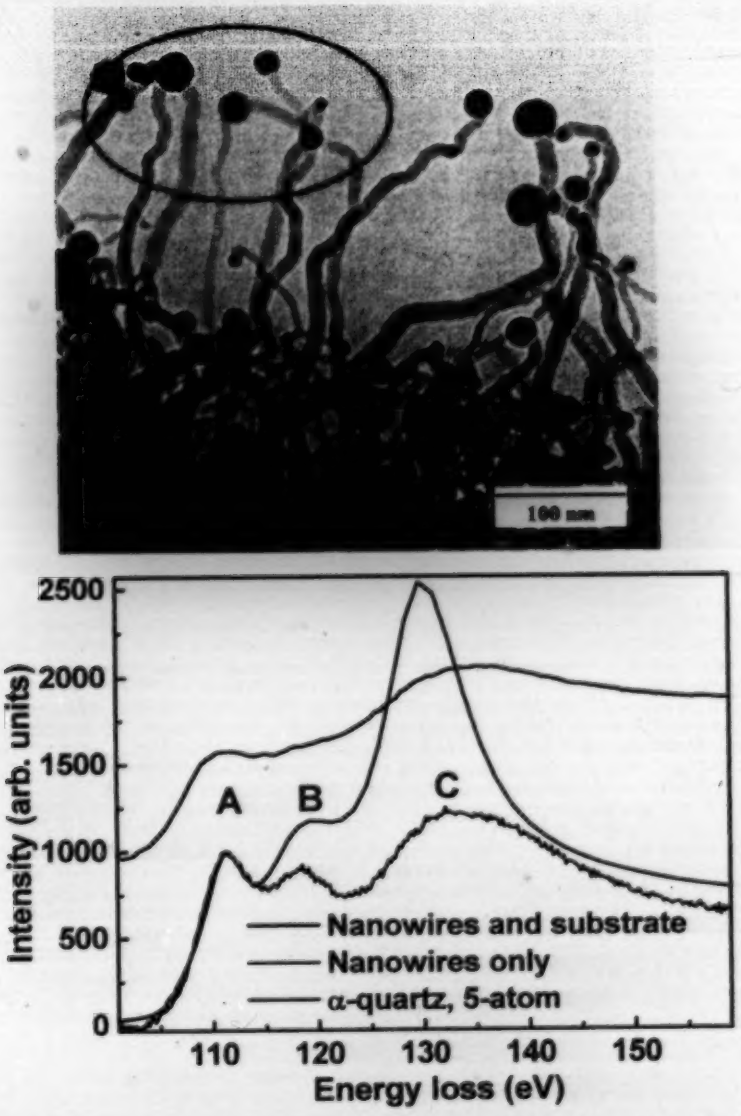

Figure 7-1 (a) Bright-field TEM image for individual NWs protruding from substrate. The ellipse shows the area for EELS recording, away from the substrate (black, left corner in the bottom). (b) Experimental Si-L_{23} edges for silicon oxide NWs with substrate (in black) and away from substrate (red), compared with a Si-L_{23} edge calculated for SiO_2 (α-quartz).

7.3 Results and discussion

Figure 7-1 (a) shows a bright-field transmission electron microscope (TEM) image of a bundle of nanowires protruding from a broken substrate. The nanowires have a smooth surface and a closed end, in which a single iron particle is entrapped. The nanowires have

diameters of 10 - 30 nm, determined by that of the nanoparticles encapsulated at the end. The structure of the nanowires is amorphous, as shown by the TEM imaging and by the diffuse nature of the electron-diffraction pattern collected from a body of nanowires.

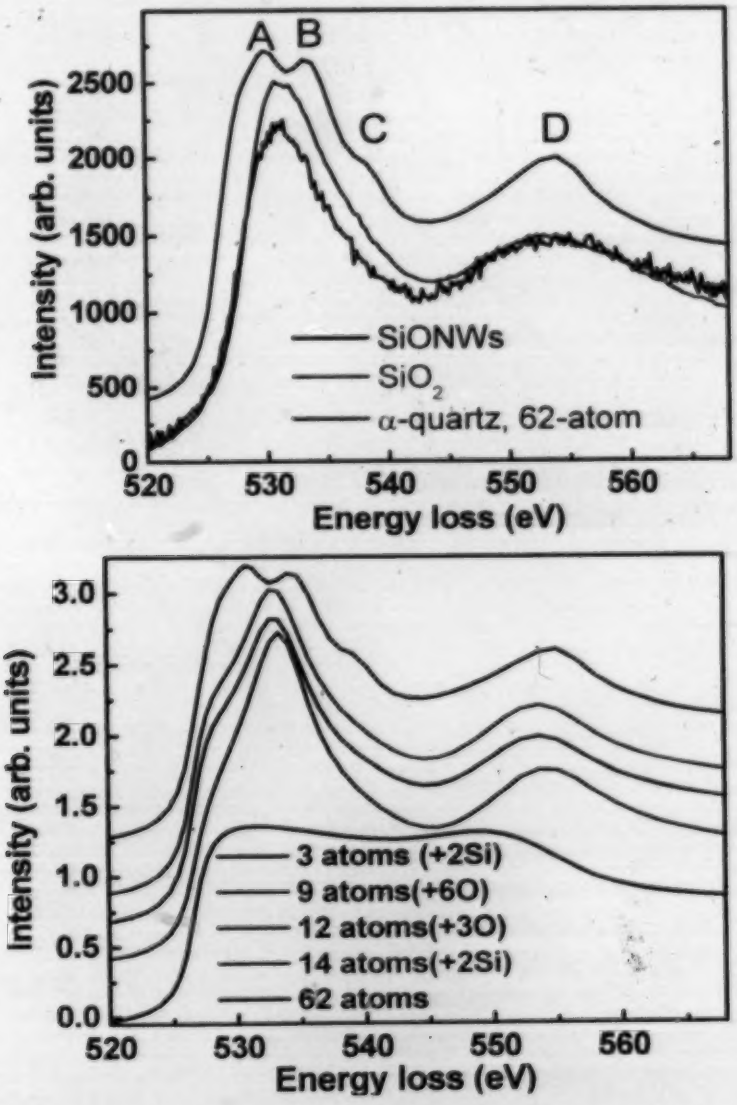

Figure 7-2 (a) A comparison of oxygen K-edge near-edge structure of NWs (black), silica (red) and α-quartz (green, a calculation based on a cluster of 62 atoms); (b) RSMS calculation on the O-K edge of α-quartz, on the clusters of increasing size.

We first checked the Si-L edges of the NWs, as shown in the Figure 7-1(b). Those recorded near the substrate (black curve) show so broad features in comparison to the spectra recorded away from the substrate (red curve), because of contribution from the

substrate (of a composition of Si_3N_4). Therefore, spectral analysis was subsequently carried out on individual NWs away from the substrate, such as those within the ellipse in Figure 7-1 (a). Meanwhile, the lack of substrate contribution can be confirmed by the absence of a N-K edge.

The silicon L-edge in NWs shows four peaks, labeled ABCD in Figure 7-1 (b). This structure, is much different in shape from the L-edge in elemental Si, and the large chemical shift (more than 5 eV)[14, 15, 16] allowed us to exclude the possibility that the wires contain an appreciable amount of elemental Si. The overall spectral shape is very similar to that of an amorphous SiO_2 film, [14, 17] and should be determined by the tetrahedral structure, consisting of a network of SiO_4 tetrahedra linked together with a large Si-O-Si angular distribution approximately centered at 144°.[17] To support this assertion, we performed RSMS calculations of silicon L-edge for α-quartz, as shown by the blue line in Figure 7-1 (b); the main features are reproducible from a calculation on a five-atom cluster, except for a red shift and the sharpening of peak C in the calculation. Apparently silicon oxide NWs are built from the same SiO_4 unit as α-quartz. Meanwhile, it can be seen that Si-L23 is restricted to the local coordination shell, while near-edge structures of O-K edge provides long-range structural information,[11] and thus were used for the study of NWs immediately below.

The O-K near edge structures of NWs is compared to that from a silica film, and also α-quartz (calculated on a cluster of 62 atoms), as shown in Figure 7-2 (a). Its features differ from those of α-quartz by absence of two small peaks, *B* and *C*, and broadening of the peak *D*. A correlation of the spectra feature with crystal structure is well demonstrated in Fig. 7-2 (b) by the RSMS calculations of the oxygen K-edge based on sequential clusters. It is obvious that the peak *A* mainly comes from the second shell of six oxygen atoms, since a calculation that includes only the first shell of two silicon atoms gives no peak, whereas calculations using clusters that include the second shell do reproduce peak *A*. A calculation using a large cluster (62 atoms) reproduced the small peaks *B* and *C*, showing that they both come from the scattering of long-range atoms. Peak *D* is so broad feature because of the limited mean free path of the excited electrons,[8] and is further broadened by the structural disorder in bonding length and angles, in silica film and NWs.

By rescaling peak *D* to the same intensity, one can see the smaller intensity of peak *A* in NWs, in comparison to that in silica film. According to the RSMS calculations, peak *A* comes dominantly from the scattering of the excited electron by the second shell of six oxygen atoms; peaks *D* comes from the first shell of two silicon atoms. If there is oxygen deficiency in the second shell, such as oxygen replaced by Si, the intensity of peak *A* is reduced because silicon atoms scatter more weakly than oxygen. This is consistent with our quantitative analysis: measuring the intensities of oxygen K and silicon L-edges and calculating their ionization cross-sections gave an atomic ratio [O]:[Si] = 1.7 ± 0.1, i.e. a composition of SiO_x with $x \approx 1.7$.

According to our study, NWs nucleate underneath the iron nanoparticles and grow by the diffusion of the Si atoms from the underlying exposed HSQ. The oxidation to the NWs would happen immediately after exposed to the air in consideration of the affinity of silicon to oxygen, the chemical composition of the as-grown nanowires can only be obtained by the real-time growth of the nanowires with in-situ method in TEM, [18] which is currently not possibly in our experimental set up.

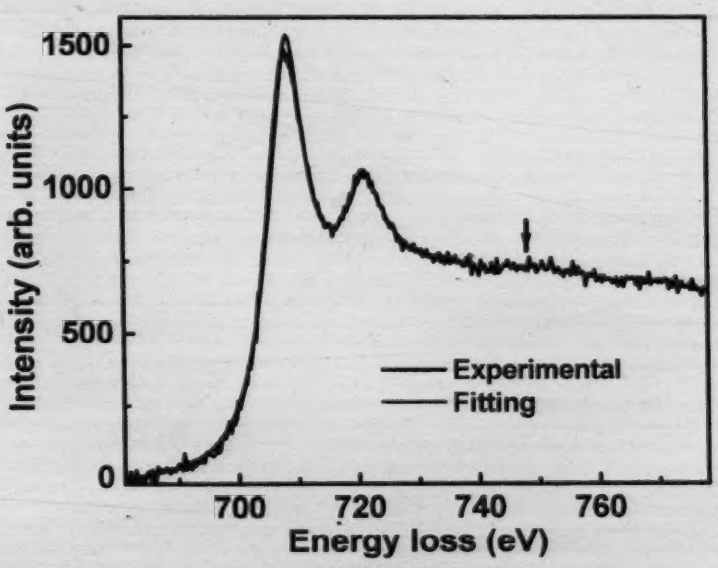

Figure 7-3 Experimental Fe-L_{23} edges (black solid line) and a computer fit of selected individual nanowires, for a spectrum recorded in the area labeled in Fig.7-1

To check the oxidation state of the iron nanoparticles at the end of tips, iron L_{23}-edges were recorded, as shown in Figure 7-3. According to our RSMS calculations, a

prominent postpeak (about 40 eV above the iron L_3 edge) occurs in iron that is oxidized even slightly, but not in pure iron.[19] This prediction was verified in our experiments and proved to be convenient technique for checking the oxidation of the iron nanoparticles embedded in a matrix.[19, 20] Here we see that the ELNES beyond the L_{23} is flat except for fluctuations due to spectral noise, so oxidation of the iron is expected to be low. The white-line ratio (WLR), a measure of the 3d-oribital occupancy, can also be used to evaluate the valence state of transition metals.[8, 21, 22] We obtained the WLR by a standard procedure, namely fitting the experimental data to two Lorentzians representing the white lines and two arctangent functions. The good fit is shown by the red curve in Figure 7-3, from which we obtained a white-line ratio of $L_3/L_2 = 2.9 \pm 0.2$. This low WLR ratio further confirms the low oxidation state of the Fe nanoparticles. Judging from the diffraction pattern, bcc-Fe is the main phase; no diffraction maxima associated with iron oxides were observed.

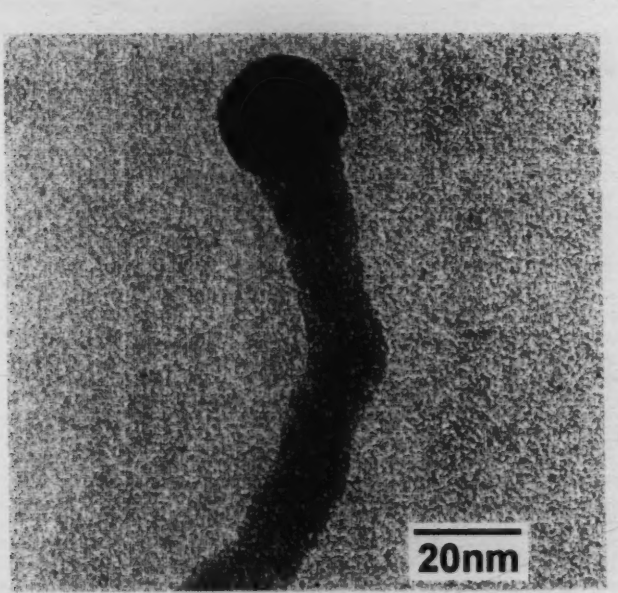

Figure 7-4 Core-shell structure at the tips of the NWs.

As checked with TEM images, core-shell structure was shown at the end of the NWs, namely, iron nanoparticles at the end being covered by a thick amorphous layer. Fig. 7-4 shows one of the NWs. Our analysis to the Fe-L edge shows clearly the low oxidation state of the iron nanoparticles, and thereby, the thick amorphous layer at the

tips could not be the iron oxides, but silicon oxides, by a combined analysis of the chemical composition of the individual nanowires by EELS.

In summary, ELNES was used to study the structural and chemical environment of silicon oxide NWs grown from a patterned reagent. Such a study provides information needed for investigation of the unusual growth process, as well as the optical properties of the NWs.

References

[1] B. Zheng, Y. Wu, P. Yang, and J. Liu, Adv. Mater. **14** (2002) 122.

[2] J.D. Carter, Y. Qu, R. Porter, L. Hoang, D.J. Masiel, and T. Guo, Chem. Commun., (2005) 2274.

[3] D.P. Yu, Q.L. Hang, Y. Ding, H.z. zhang, Z.G. Bai, J.J. Wang, Y.H. Zou, W. Qian, G.C. Xiang, S.Q. Feng, Appl. Phys. Lett., **73** (1998) 3076.

[4] J.Q. Hu, Y. Jiang, X.M. Meng, C.S. Lee and S.T. Lee, Chem. Phys. Lett. **367** (2003) 339.

[5] X.C. Wu, W.H. Song, K.Y. Wang, T. Hu, B. Zhao, Y.P. Sun and J.J. Du, Chem. Phys. Lett. **336** (2001) 53.

[6] K.H. Lee, C. Lofton, K. Kim, W.S. Seo, Y. Lee, M.H. Lee and W. Sigmund, Solid State Commun. **131** (2004) 687.

[7] Z. Chen, Y.X. Wang, H. He, Y. Zou, J. Wang and Y. Li, Solid State Communications **135** (2004) 247.

[8] R.F. Egerton, Electron Energy-Loss Spectroscopy in the Electron Microscope, 2nd edition,Plenum Press, New York (1996).

[9] D.A. Muller, T. Sorsch, S. Moccio, F.H. Baumann, K. Evans-Lutterodt, and G. timp, Nature **399** (1999) 758.

[10] L.J. Garvie, P. Rez, J.R. Alvarez, P.R. Buseck, A.J. Craven, and R. Brydson, American Mineralogist, **85** (2000) 732.

[11] D.J. Wallis, P.H. Gaskell, and R. Brydson, J. Microscopy, **180** (1995) 307.

[12] R.G.W. Wyckoff, Crystal Structures, 2nd ed. (Wiley, New York) (1963).

[13] A.L. Ankudinov, B. Ravel, J.J. Rehr, S.D. Conradson, Phys. Rev. B **58** (1998) 7565.

[14] G.A. Botton, J.A. Gupta, D. Landheer, J.P. McCaffrey, G.I. Sproule, and M.J. Graham, J. Appl. Phys. **91** (2002) 2921.

[15] P.E. Batson, Microsc. Microanal. Microstruct. **2** (1991) 395.

[16] Ahn, C.C., Krivanek, O.L., Brugner, R.P., Disko, M.M., and Swann, P.R., 1983. EELS Atlas. ASU HREM facility and Gatan Inc..

[17] X-ray absorption Near Edge Structures of SiO_2, by F. Jollet, in Structure and Imperfections in Amorphous and Crystalline Silicon Dioxide, edited by R.A.b. Devine, J.P. Duraud and E. Dooryhee. JOHN WILEY&SONS, LTD. (2000))

[18] Y. Wu, and P.Yang. J. Am. Chem. Soc. **123** (2001) 3165.

[19] F. Wang, R.F. Egerton, and M. Malac. Ultramicroscopy **106** (2006) 925.

[20] F. Wang, M.Malac and R.F. Egerton, Micron **37** (2006) 316.

[21] C. Colliex, T. Manoubi, and C. Ortiz, Phys. Rev. B **44** (1991) 11402.

[22] D.M. Pease, A. Fasihuddin, A, A.M. Daniel, and J.I. Budnick, Ultramicroscopy **88**, (2001) 1.

Chapter 8 General discussion and conclusion

The results shown in this thesis are outcomes from projects that are in many cases open-ended. This chapter will summarize the main results obtained up to now and show their significance for applications, but with emphasis on possible future directions in ongoing projects.

Electron energy-loss spectroscopy (EELS) in a transmission electron microscope (TEM) can provide compositional and chemical information, complementary to microstructural analysis by TEM imaging.[1] Dramatic advances in instrumentation have significantly improved EELS measurement capability and thus extended its applicability in nanoscience; for example, a spatial resolution of 0.1 nm and energy resolution of 0.1 eV can be expected.[2] Still, the most challenging problem is the identification of valence or bonding state of elements in nanostructural materials, such as the local oxidation of metallic nanoparticles.[3,4,5,6,7,8,9,10] The white-line ratio (WLR) has long been used in evaluating the valence state of transition metals;[1,11,12,13] extraction of WLR by standard fitting and its application in studying *in-situ* fabricated iron nanoparticles were discussed in *Chapter 2*. When measuring at high spatial resolution, the obtainable edge intensities are very low because of the limited exposure time needed to avoid specimen drift and radiation damage. *Chapters 3, 4 and 5* show that a prepeak in the oxygen K-edge and postpeak in transition-metal L-edge arise from the chemical bonding to nearest-neighbour atoms and are thus highly localized and sensitive to oxidation. These factors favour the prepeak and postpeak techniques, in combination with the high-resolution STEM imaging, over the WLR approach.

Results presented on the oxidation of iron nanoparticles in this thesis research were all obtained from a 200 kV LaB_6 instrument, the JEOL 2010, and surveyed the average oxidation of thousands of iron nanoparticles, due to the limitation in spatial resolution and beam brightness. Local oxidation of single nanoparticles can be further pursued with more advanced TEMs. In very recent experiments executed in a JEOL 2200 FS, a variation of the postpeak amplitude was observed when focusing the probe at

different locations, such as at the edge and center of a single iron nanoparticle (10 nm in diameter); this result is presented in *Appendix C*.

Nanofabrication by novel processes is an important part of this thesis research. *Chapter 2* describes the *in-situ* fabrication of iron nanoparticles by electron-induced decomposition of iron fluorides. The iron nanoparticles produced are metallic, as shown by ELNES measurements, and exhibit ferromagnetism, as shown by Lorentz imaging in TEM. Fabrication of a large area of stable magnetic nanoparticles, for magnetic storage applications, is the concern of *Chapter 4*, and is achieved by embedding iron nanoparticles in a SiO_2 matrix through a newly developed multilayer-and-annealing route in an ultra-high vacuum (UHV) system. The oxidation resistance of the iron nanoparticles was verified both by ELNES and by magnetization measurement. Iron-SiO_2 nanocomposites are compatible with electron beam lithography, in which regular arrays of circular nanodots were successfully fabricated, each dot containing only a few nanoparticles. Part of these results are shown in *Chapter 6* and reveal that such an approach is promising in fabricating desired arrays of discrete metallic nanoparticles with size well below 10 nm. *Chapter 6* also shows that these Fe-SiO_2 nanocomposites allow the growth of nanowires on selected sites, by fabricating arrays of silicon oxide nanowires (NWs) from the patterned reagent. The NWs were seeded by metallic iron nanoparticles and the resulting microstructure and morphology of the NWs is directly related to the size of the individual iron nanoparticles.

In preparing the iron nanoparticles in a SiO_2 matrix via a multilayer-and-annealing route (see, in *Chapter 4*), it was found that the multilayers amalgamate in the nanoparticle formation process, and therefore there is significant diffusion of iron through the SiO_2 layers. The particle morphology is determined by many factors, such as the annealing temperature, heating rate and composition of the multilayers. We were able to control particle size and separation by adjusting and controlling these parameters. However we still do not have detailed understanding of the physical nature of the processes. *In-situ* experiments would enable us to observe growth of the nanparticles in real time at high spatial resolution. Initial experiments done in Brookhaven National Lab (BNL), shown in *Appendix B*, proved that it is possible to observe nanoparticle growth in TEM and to perform *in-situ* analysis of chemical state by electron diffraction and EELS,

and magnetic properties by electron holography. Unfortunately the samples were pre-fabricated several weeks prior the analysis. To successfully conclude these experiments, the samples need to be prepared within a maximum of a few hours before the analysis. Such experiments exploring the growth process could be carried out following installation of the new TEMs in National Institute for Nanotechnology and a new setup of the UHV system.

In *Chapters 6 and 7*, a growth and ELNES study of the silicon oxide nanowires (ELNES) is described, showing the growth process and chemical and structural environment of the NWs. The mechanism of this unusual growth of the NW arrays is still controversial, mainly because till now it was not possible to determine the actual chemical state of the as-grown nanowires due to suspected fast oxidation when exposed to the atmosphere. If fabrication of Fe-SiO_2 nanocomposites and growth of nanowires can be carried out in a TEM, an incorporated EELS spectrometer would provide a chance for *in-situ* real time analysis, monitoring evolution of the chemical state of nanowires and iron nanoparticles by ELNES, in addition to the real time observation.

Amorphous silicon oxide NWs emit strong blue light and might therefore be applied in integrated optical devices.[14] Several emission bands, of different emission characteristics, depending on the composition and disorder of the silica nanowires, were also recently reported.[15, 16, 17, 18] Distinct optical properties of the silicon oxide NWs compared to a silicon dioxide film are implied by spectra of low-loss EELS, such as a redshift of the bulk plasmon peak and the appearance of additional fine structure. Optical properties, such as complex permittivity $\varepsilon(E)$, can be derived by Kramers-Kronig analysis; so that the results are comparable with other optical measurements.[1] Photoluminescence of those arrays of silicon oxide NWs, in combination of the low-loss EELS and ELNES study, is a subject of potential further research.

Of increasing interest for the analysis on local atomic and electronic structures is the interpretation of other properties that could be examined simultaneously in the TEM. One option is optical properties, such as dielectric function and band-gap states, that can be derived from low-loss EELS (<50 eV),[1] although the delocalization of the low-loss signal, implied by Eq. (1.12), is on a scale of several nanometers, much worse than ELNES.[19] Another property is the internal field distribution (changes in the local

magnetic or electrostatic potential) that can be examined by electron holography;[20] An enhancement of spatial resolution and flexibility of control can be expected with a double bi-prism system.[21, 22] A comprehensive understanding of sample properties might be obtained by combined characterizations within a single TEM, as illustrated by Figure 8-1.

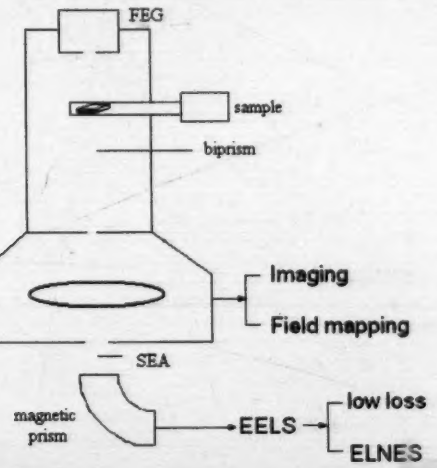

Figure 8-1 Analytical capabilities of a TEM (equipped with a field emission gun), including microstructure by *imaging* (bright field or Z-contrast), electronic and geometric structures by *ELNES*, optical properties by *low loss*, and local magnetic/electrostatic potential by *electron holography*.

References

[1] R.F. Egerton, Electron Energy-Loss Spectroscopy in the Electron Microscope, 2nd edition, Plenum Press, New York (1996).

[2] N.D. Browning, I. Arslan, R. Erni, J.C. Idrobo, Z. Ziegler, J. Bradley, Z. Dai, E.A. Stach, and A. Bleloch, Journal of Physics: conference series 26 (2006) 59.

[3] D.A. Muller, Y. Tzou, R. Raj, J. Silcox, Nature 366 (1993) 725.

[4] P.E. Batson, Nature 366 (1993) 727.

[5] N.D. Browning, M.F. Chisholm, S.J. Pennycook, Nature 336 (1993) 143.

[6] M. Varela, A.R. Lupini, H.M. Christen, A.Y. Borisevich, N. Dellby, O.J. Krivanek, P.D. Nellist, S.D. Findlay, M.P. Oxley, L.J. Allen, and S.J. Pennycook, Phys. Rev. Lett. **92** (2004) 095502.

[7] T. Suenaga et al., Science **290** (2000) 2280

[8] A. Ziegler et al, Science **306** (2004) 1768.

[9] I. Arslan et al, Phys Rev Lett. **94** (2005) 25504.

[10] J. Bradley et al, Science **307** (2005) 244.

[11] Z.L. Wang, J. Bentley, and N.D. Evans. Micron **31**(2000) 355.

[12] D.M. Pease, A. Fasihuddin, M. Daniel, and J.I. Budnick. Ultramicroscopy **88** (2001)1.

[13] C. Colliex, T. Manoubi, and C. Ortiz. Phys. Rev. B **44** (1991) 11402.

[14] D. P. Yu, Q. L. Hang, Y. Ding, H. Z. Zhang, Z. G. Bai, J. J. Wang, Y. H. Zou, W. Qian, G. C. Xiong, and S. Q. Feng, Appl. Phys. Lett. **73** (1998) 3076.

[15] Q. Hu, Y. Jiang, X.M. Meng, C.S. Lee and S.T. Lee, Chem. Phys. Lett. **367** (2003) 339.

[16] X.C. Wu, W.H. Song, K.Y. Wang, T. Hu, B. Zhao, Y.P. Sun and J.J. Du, Chem. Phys. Lett. **336** (2001) 53.

[17] K.H. Lee, C. Lofton, K. Kim, W.S. Seo, Y. Lee, M.H. Lee and W. Sigmund, Solid State Commun. **131** (2004) 687.

[18] Z. Chen, Y.X. Wang, H. He, Y. Zou, J. Wang and Y. Li, Solid State Communications **135** (2004) 247.

[19] R.F. Egerton. Microsc Microanal **12** (supp 2) (2006) 102-103.

[20] M. Lehmann, and H. Lichte, Microsc. Microanal. **8** (2002) 447.

[21] K. Harada, A. Tonomura, Y. Togawa, T. Akashi, and T. Matsuda, Appl. Phys. Lett. 84 (2004) 3229.

[22] K. Harada, A. Tonomura, T. Matsuda, T. Akashi, and Y. Togawa, Journ. Appl. Phys. **96** (2004) 6097.

Appendix A Procedures for *in-situ* annealing in UHV system

1. Open the water-cooling for the shroud.
2. Switch on the heating power supply.
3. Check the data for current-temperature shown below, to use an appropriate current for the annealing.
4. Raise the CURRENT slowly to destination temperature, for example, by 2 ampere / 3 minute, for a general purpose; or use even lower heating rate according to your own experimental requirement. *Don't raise the current too quick.*
5. Keep heating for a certain period at your destination temperature.
6. Lower the CURRENT slowly, such as 2 A/ 3 minute as a suggestion and switch off heating power supply finally. *Don't switch off the power supply until the temperature is below 400℃.*

Table A-1 Temperature vs current in MBE chamber (Rough data from annealing experiments)

Current (A)	12	18	22	24
Temperature (°C)	600	800	900	1000

Appendix B Growth process of iron nanoparticles in a silica matrix: a real time study by in-situ transmission electron microscopy

(*F. Wang*, M. Malac, R.F. Egerton, M. Schofield, and Y. Zhu, unpublished)

B.1 Introduction

As shown in Chapter 4, isolated stable iron nanoparticles embedded in a silica matrix could be prepared through a multilayer route in an ultra-high vacuum (UHV) system. [1] It is interesting to see that there are no longer numerous alternating Fe and SiO_2 layers; the multilayers are amalgamated in the formation of iron nanoparticles, larger than the layer thickness. The particle morphology is determined by many influential factors, such as the annealing temperature, heating rate, composition of the multilayers. Choosing appropriate parameters is critical in obtaining a well-dispersed iron nanopraticles in SiO_2 matrix; the real-time study in TEM will provide insight of the growth process, and guide us in further fabrications.

As far as we know, there is only one report on the structure evolution of iron nanoparticles due to the in-situ annealing treatment of iron nanoparticles on bare carbon (and Si_3N_4 membrane) recently;[2] in which iron nanoparticles grow by coalescence, leading to different crystal structures at different particle sizes. The growth process of the iron nanoparticles in an insulating matrix could be different. The diffusion of the iron atoms in the SiO_2 matrix should be restrained by the intervening layers of SiO_2, by limiting the mobility and thus the diffusion path of the iron atoms at a given temperature. In this work, the dynamic diffusion process was monitored by in-situ annealing in an advanced TEM, using movies and sequential images; the phase state of iron was examined with electron diffraction pattern. Furthermore, the equipped biprism in the

TEM provides a chance to study the magnetic properties in-situ, by taking hologram from individual nanoparticle.

B.2 Experiments

Trilayers of SiO_2/ Fe/SiO_2 (8nm/2nm/6nm) were deposited sequentially onto 4 nm-thick carbon films (supported by copper grids) in an ultra-high vacuum (UHV) system with a base pressure of 10^{-10} Torr.[1] Before the deposition, the substrates were baked for ten hours in the load-lock chamber at a temperature above 180 °C, to remove adsorbed water. The pressure during film growth of Fe and SiO_2 was 10^{-9} Torr (with $H_2O$and O_2 partial pressure: 10^{-11} Torr and 10^{-12} Torr). Films were deposited at a deposition rate of 1.0 Å/s onto room temperature substrates. A quartz-crystal monitor was used to measure the film thickness and deposition rate. Then the morphology and phase state of iron films in the samples were checked in a local TEM (JEOL 2010). The in-situ annealing was done in a JEOL 2100F field-emission TEM, equipped with a heating holder for in-situ annealing, TV-rate camera for recording a real-time video of the process, and a retractable biprism assembly for *in-situ* holography. The samples were annealed in the TEM, using a heating holder with two different modes: smart control in which the destination temperature was set and reached within 3 minutes, and manual control in which temperature can be raised manually. We used the manual heating mode with a low heating rate of 2°C/minute, during which, the movie was recorded to study the temperature dependent growth process. Then we used the smart mode to study the evolution of the nanoparticles with prolonged annealing time by recording the TEM images consequently. We used the selected area diffraction pattern to check the phase state of iron immediately after fabrication and after the annealing. The magnetic properties were investigated by in-situ hologram in JEOL 2100F, which is equipped for electron holography with a retractable biprism assembly consisting of a platinum wire, 0.6 mm in diameter. The biprism wire is rotatable ± 90° and located approximately in the selected area aperture plane of the microscope. The multiscan CCD camera located below the Gatan Image Filter attached to the microscope was used to record holograms.[3]

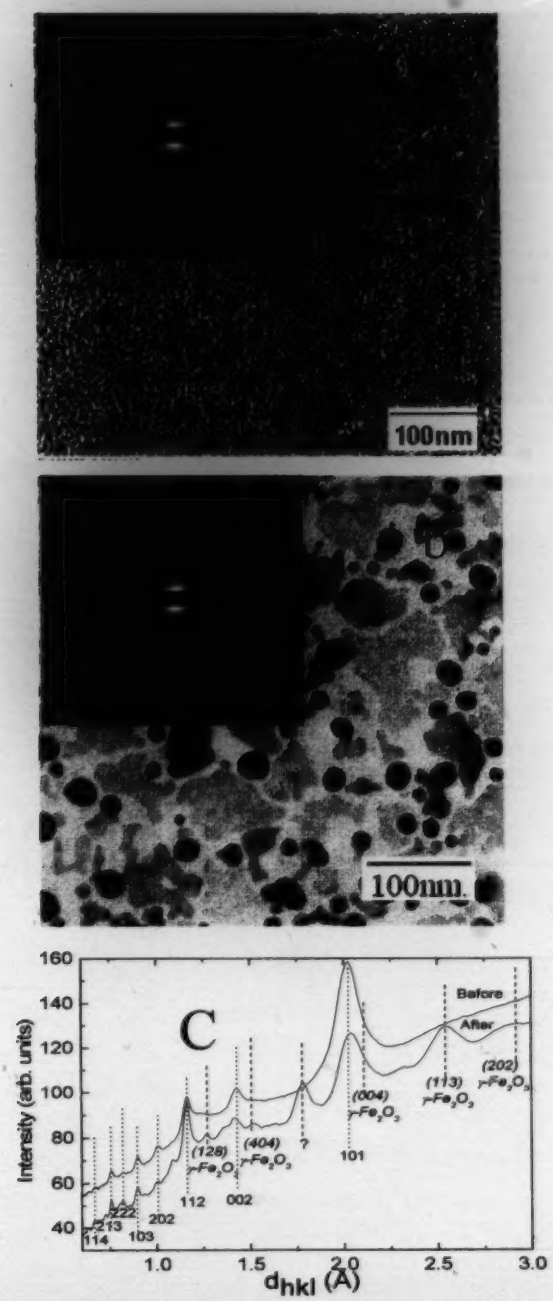

Figure B-1 Morphology and phase identification of iron nanoparticle before and after annealing. (a) Iron film embedded in SiO_2 matrix and its diffraction pattern (inset); (b) nanoparticles obtained by annealing at low heating rate and the diffraction pattern (inset) (c) diffraction intensity profile obtained by integration the diffraction rings, using Digitalmicrograph, the peaks associated to α-Fe were indicated by vertical dot lines and the peaks associated to γ-Fe_2O_3 were indicated by dashed lines.

B.3 Results

Immediately after fabrication in UHV, the samples were transferred to a local TEM (JEOL 2010) for morphology and phase analysis quickly (within 20 minutes). The iron film of only 2 nm is not continuous when grown onto 8 nm SiO_2 buffering layer, as seen in Figure B-1 (a), a network of iron clusters, below 10nm in dimension (discerned as darker region) was formed and surrounded by SiO_2 matrix. The buffering and capping SiO_2 layers give a good temporary protection of the iron film; all the diffraction maxima are associated to the α-Fe phase. For a better view and enhancement of the visibility to weak rings, integral diffraction pattern profiles (Fig. B-1 (c)) were obtained using Digitalmicrograph. No iron oxides phase can be observed in the film before the annealing.

The whole annealing process at low heating rate (2°C/minute) was recorded by movies using a TV camera in JEOL 2100F, starting from the iron clusters at room temperature to the well-dispersed iron nanoparticles in SiO_2 matrix at 830°C (the highest temperature obtainable in the TEM). Basically the annealing process can be divided into two distinct stages: the quick growth by coalescence stage and the gradual development of small nanoparticles and growth by non-coalescence stage. In the first stage, no obvious change of the iron clusters was noticed below 500°C, above which, the small clusters started to coalesce and form bigger clusters of irregular shapes, they become rounded with further increase of the temperature, and in between the clusters are bigger space left. The coalescence stage slowed down above 600°C, and was no longer noticeable above 650°C; nearly spherical nanoparticles of about 20 nm in diameter are the final result from the coalescence. In the second stage, no coalescence was observed with further increase of the temperature, the nanoparticles grew very slowly with prolonged annealing, without further change of the shape; particularly tiny nanoparticles was developed in this stage, at around 700°C in this experiment. We found that those developed nanoparticles, although are so near to big nanoparticles, keep them isolated in the whole process, during which the sample was heated to 830°C in this experiment. The ripening, namely a process that the larger particles grow at the expense of smaller particles, can be a common event happens in forming the particles by diffusion. However this was not observed in the second annealing stage. In a whole, the nanoparticles are very uniform, of about 20 nm in

diameter, although there is some smaller nanoparticles that were developed in the second stage. Unfortunately, oxidization happened during the annealing, γ-Fe_2O_3 is the main phase, as marked by the dashed line in Figure B-1 (c).

Specimen drift is so serious when the temperature changes, this brought difficulty for us in focusing the beam onto a certain group of nanoparticles. So smart control mode was also used to keep the sample stable after a short time of rapid temperature change (within about 3 minutes). In this experiment, 650°C was chosen as the destination temperature, because the growth of non-coalescence happens mostly at the temperature above 650°C, so that the dependence of the growth on the annealing time can be studied at the fixed temperature. Bright field images were taken every two minutes immediately after the stabilization of the temperature. In comparison to the first experiment, tiny nanoparticles were developed at the temperature of 650°C. They grew up gradually and the resulted nanoparticles after 16 minute annealing can be as big as 10 nm in diameter.

Big nanoparticles of wide size distribution were obtained in the annealing at this fast heating rate. The nanoparticles formed in the first stage are as big as 100 nm in the studied region, and particles of 200 nm were also found in other regions in a search over the whole sample; those gradually developed nanoparticles in the second stage are smaller than 10 nm in general. The oxidation (γ-Fe_2O_3) was also found in the nanoparicle obtained in the annealing by smart control, and is the main phase according to the integral intensity profiles of the diffraction patterns.

Figure B-2 shows four of the images taken after the temperature was stabilized, and three particles, labeled as *A*, *B* and *C* are typical particles chosen as study subjects. *A* and *B* are two big nanoparticles formed in the first stage, they did not coalescence into one bigger particle although the space in between became so small with the increase of their volume in the second stage. The small particle *C* formed in the second stage, grew up steadily with prolonged time and keep itself isolated , instead of incorporation into *B* by ripening. This is common in the annealing process at both high and low heating rates, according to the video and the sequential images. In this sense, our experimental results are much different from the in-situ annealing for iron nanoclusters on carbon film,[2] in which the nanoparticles coalesced seriously, so that no isolated nanoparticles were obtained.

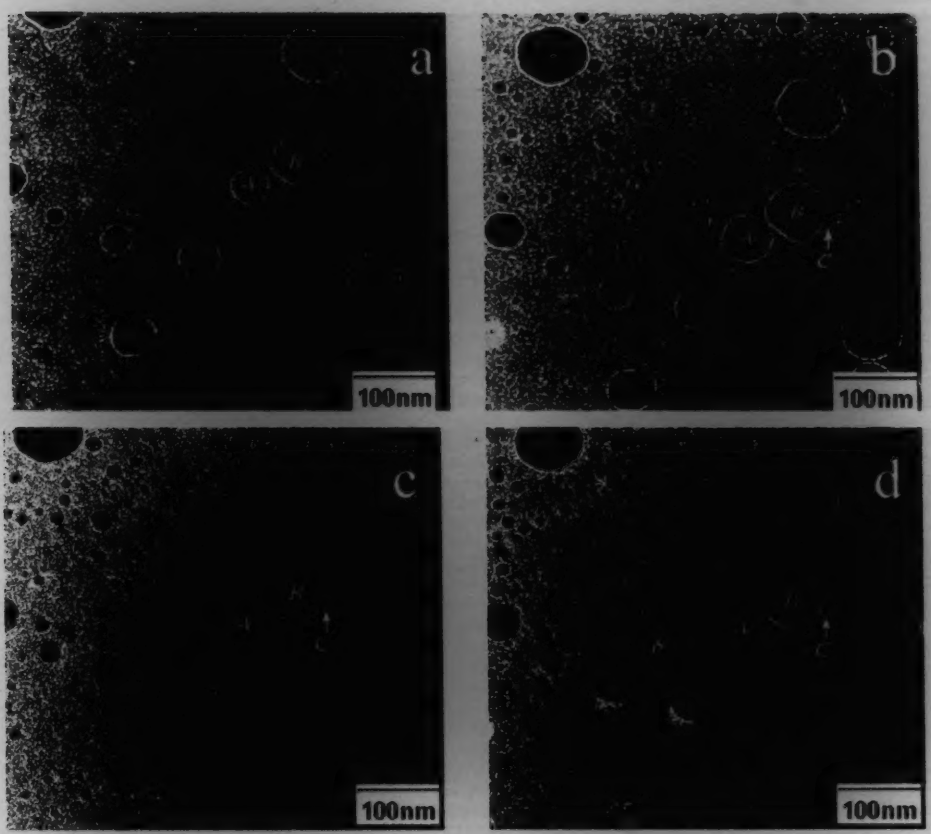

Figure B-2 Bright field TEM images taken during annealing by smart control, by which the sample can be heated to destination temperature within 3 minutes. The images were taken every two minutes, four of them were shown in the figure: (a) 2nd minute (b) 16th minute (c) 30th minute (d) 60th minute.

The driving force for coalescence is the diffusion of atoms on the cluster surface from the regions of high curvature (where they have fewer neighbors and therefore are less strongly bonded) towards the regions of lower curvature. In our experiments, it appears that the particles can grow only by accepting new atoms diffused through the matrix, but could not fuse into big nanoparticles. The matrix SiO_2 must have played a critical role in forming the isolated iron nanoparticles. In one hand, the SiO_2 matrix changes upon annealing, condensation would happen,[4] at high temperature, the particles may assemble into Fe/SiO_2 core-shell nanostructure, SiO_2-shells around individual nanoparticles passivate their surface and prevent coalescence, such a phenomenon has been revealed in gold / carbon core/shell structure recently;[5] on the other hand, oxidation

(as shown in Fig. B-1 (c)) formed on the particle surface may further prevent the coalescence and ripening.

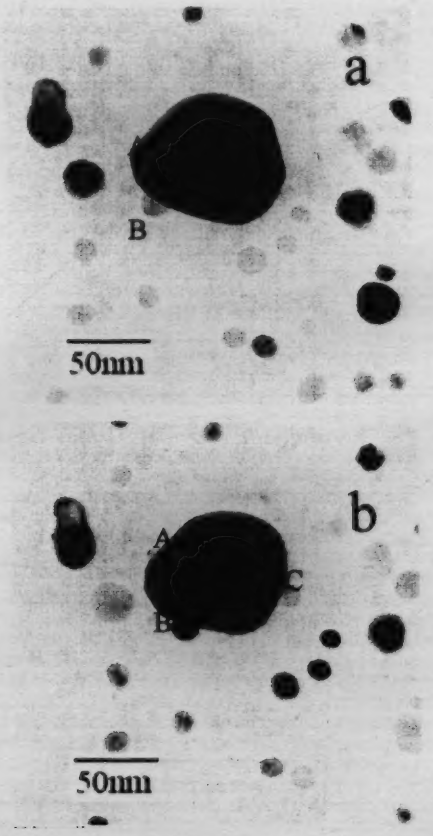

Figure B-3 Bright field TEM images for the iron nanoparticles taken at rotations of 0° and 30°.

Iron nanoparticles were not confined between SiO_2 layers as initially, some big particles were found on the surface of the SiO_2 matrix. Those nanoparticles grew up across the SiO_2 layers by combining the iron atoms (clusters) diffused through the SiO_2 matrix. This is consistent with our previous experiments in the annealing of Fe/SiO_2 mulitilayers in UHV, uniformly distributed iron nanoprticles were formed by the amalgamation of the multilayer, according to cross-sectional TEM images.[1] Figure B-3 (a) shows the bright field TEM images taken from the annealed samples. There are three small nanoparticles labeled as A, B, and C (about 10 nm in diameter) overlapped with a big nanopareticle (around 100 nm in diameter), they were not incorporated into the big nanoparticles. As shown in Figure B-3(b), when the sample was tilted by 30°C, a small

change of the position for particle B can be seen, while particles A and C appear at the edge of the big particles. Meanwhile, there is small change of the relative positions of the three small nanoparticles ABC. This clearly shows that the four nanoparticles are confined at different layers from each other by the SiO_2 matrix.

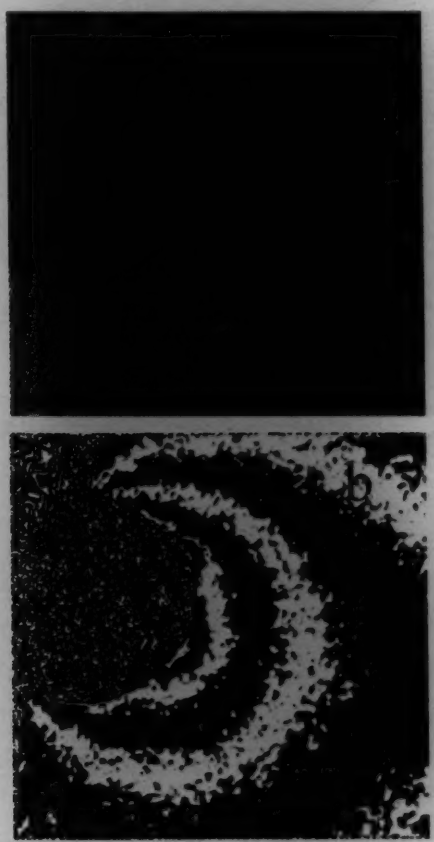

Figure B-4 (a) Hologram and (b) 16x phase amplified contour map of magnetic field for a single nanoparticle obtained in the annealing by smart control.

Two typical particle shapes were observed after in-situ annealing, namely, spherical or cubic, as shown in Figure B-1 (b) and Figure B-2. Big nanoparticles exhibit spherical (or nearly spherical) shape, while smaller nanoparticles can be spherical or octahedral. The most stable structures for medium-sized clusters (i.e., 100-10000 atoms) are bcc rhombic dodecahedron with 12 pseudoclose-packed {110} faces (having the lowest surface energy for bcc structures) according to the calculations.[6, 7] High resolution TEM images has been taken and analyzed by Vystavel et.al., in their in-situ annealing experiments, it was disclosed that the truncation of theoretically envisaged rhombic dodecahedron increases

the spherical shape of the nanoparticles although it also increases the fraction of the energetically less favorable faces.[2]

The equipped biprism in the TEM provides a chance to study the magnetic properties in-situ, as exampled by a hologram taken from one single nanoparticle in Figure B-4 (a). By a digital reconstruction procedure using fast Fourier transform (FFT),[8] the cosine map of the reconstructed phase (amplified 16x) was extracted to show the fringing field associated with the particle. Besides, a highly spatial-resolved field distribution can be used to study domain structures of single nanoparticles, and the interactions between magnetic nanoparticles;[9,10] this would be our further study.
In summary, in-situ annealing in TEM was used to study the diffusion and formation of the iron nanoparticles in a silica matrix. A two-stage growth process was revealed and attributed to the matrix effects, in the real-time observation; annealing temperature and heating rate affect the particle size distribution and morphology. Unfortunately, the iron nanoparticles were seriously oxidized because of the long-time exposure to the air before the annealing; this could be resolved by an on-site sample preparation.

References

[1] F. Wang, M. Malac, R.F. Egerton, A. Meldrum, X. Zhu, Z. Liu, N. Macdonald, P. Li, and M.R. Freeman, J. Appl. Phys. (in revision)

[2] T. Vystavel, G. Palasantzas, S.a. Koch and J. Th. De Hosson, Appl. Phys. Lett. **82** (2003) 197.

[3] M.A. Schofield, M. Beleggia, and Y. Zhu, Microsc. Microanal. **11** (S 2) (2005) 570.

[4] L. Zhang, W. Xie, Y. Wu and H. Xing, Chin. Phys. Lett. **20** (2003) 1366.

[5] E. Sutter, P. Sutter and Y. Zhu, Nano Lett. **5** (2005) 2092.

[6] D. Wolf, Philos. Mag. A. **63** (1991) 337.

[7] M.J.S. Spencer, A. Hung, I.K. Snook and I. Yarovsky, Surf. Sci. **513** (2002) 389.

[8] M. Lehmann, and H. Lichte, Microsc. Microanal. **8** (2002) 447.

[9] M.J. Hytch, R.E. Dunin-Borkowski, M.R. Scheinfein, J. Moulin, C. Duhamel, F. Mazaleyrat, and Y. Champion, Phys. Rev. Lett. **91** (2003) 257207.

[10] T. Uhlig, and J. Zweck, Phys. Rev. Lett., **93** (2004) 47203.

Appendix C Local oxidation of single iron nanoparticles in a SiO_2 matrix

Chapter 4 shows the fabrication and oxidation resistance of iron nanoparticles embedded in a SiO_2 matrix through a multilayer route in an ultra-high vacuum (UHV) system. In order to closely examine the local oxidation of the iron nanoparticles, electron energy-loss spectra and high-resolution transmission electron microscopy (HRTEM) images were recorded from individual nanoparticles.

C.1 STEM-EELS of a single iron nanoparticle

The appearance of a postpeak, a broad post-edge peak above the L_3, is a characteristic of transition metals in an oxidized state (see, in Chapter 3). The postpeak technique has been proved to be convenient and sensitive in identifying the oxidation of the iron nanoparticles embedded in a SiO_2 matrix (Chapters 4 and 5). The previous results were obtained from a TEM equipped a thermal emission gun (JEOL 2010) and surveyed the averaged oxidation of thousands of iron nanoparticles in an area of several micrometers in diameter, because of limitations in spatial resolution and beam intensity.

For a purpose of identifying local oxidation of individual particles, ELNES spectra of Fe-L edge were recently obtained from a single iron nanoparticle (of about 10 nm in diameter) by a STEM-EELS technique in a JEOL2200FS (scanning) transmission electron microscope. Spectra can be acquired at different locations of a particle with a nanometer-sized electron probe. Figure C-1 shows the ELNES of Fe-L edges recorded at the edge and center of a single particle, together with a high-angle annular dark-field (HAADF) image of a collection of iron nanoparticles, the beam positions being illustrated. The signal comes mostly from the surface of the particle when the beam is focused at its edge, and it mainly comes from the interior when the beam is focused at the center. As seen in Fig. C-1(a), a broad postpeak appears in the spectrum recorded from the edge, but not in the spectrum taken from the center (disregarding fluctuations coming from noise). This clearly shows that oxidation produced only a very thin oxide layer at

the particle surface. This result is consistent with our conclusion on oxidation by other techniques in *Chapters 4 and 5*.

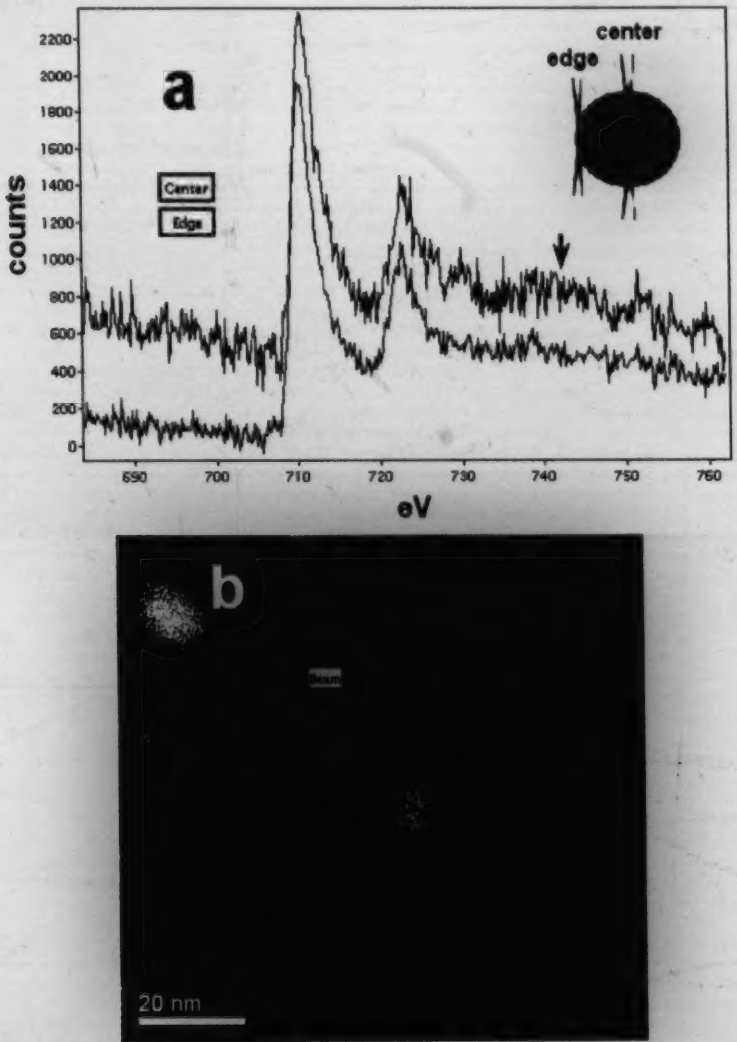

Figure C-1 STEM-EELS results on a single iron nanoparticle of 10 nm in diameter. (a) ELNES of Fe-L_{23} on the edge and center of the particle, with postpeak position labeled by an arrow. The inset illustrates the experimental setup. (b) HAADF image of a collection of iron nanoparticle particles. The beam position on the edge is labeled by "+". (Courtesy of Dr. Yucheng Lan, Michigan state University)

C.2 HRTEM of a single iron nanoparticle

Figure C-2 shows HRTEM images recently recorded on single iron nanoparticles along the [111] zone axis in a Hitachi HD 2300 (S)TEM equipped with a cold field emission

gun (CFEG). The iron crystal lattice can be well resolved from the image, as seen in Figure C-2 (a); it continues to the right edge of the particle. The fast-Fourier transform (FFT) from a selected area in the image of one nanoparticle, as marked by a red square in Fig. C-2 (b), clearly shows the single bcc-phase of the particle.

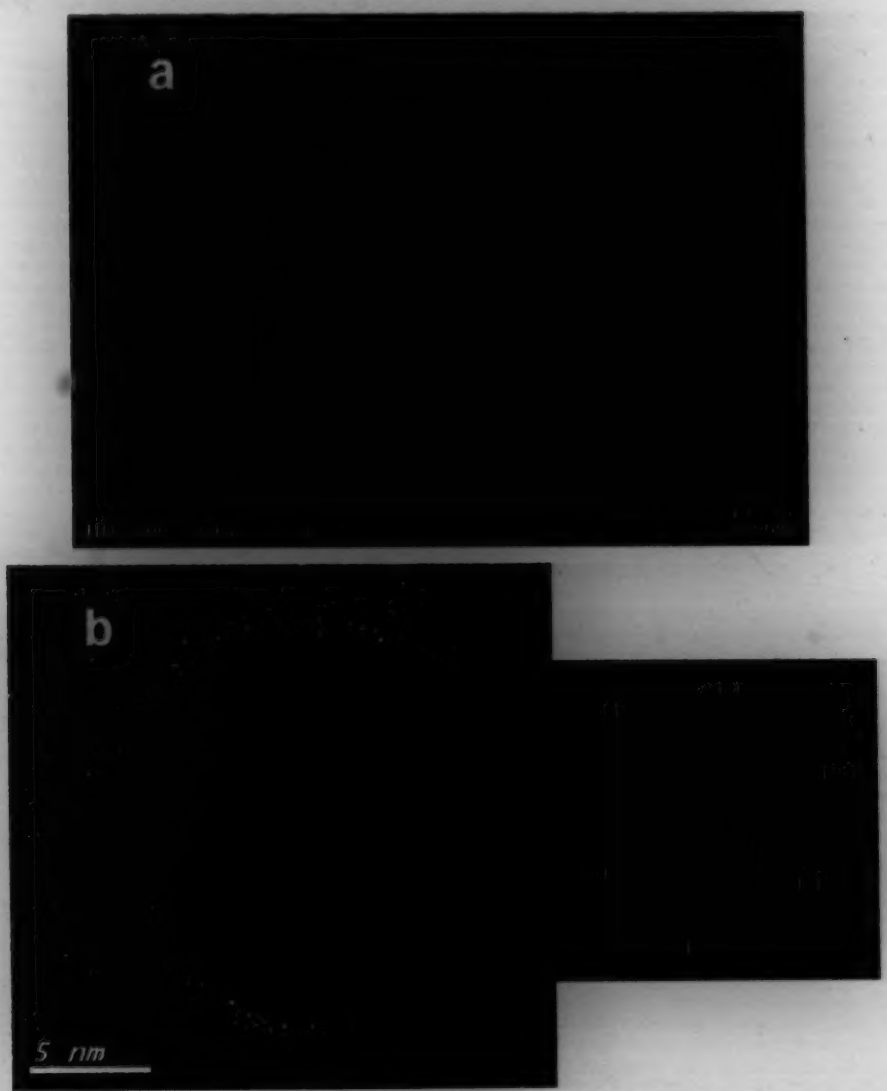

Figure C-2 (a) Crystal lattice of a single iron nanoparticle and (b) HRTEM image and a FFT of the marked square area for one nanoparticle. (Courtesy of Drs. Koji Kimoto (NIMS, Tsukuba) and Kuniyasu Nakamura (Hitachi High Technologies, Naka division)

Appendix D Magnetite nanoparticles

(by Feng Wang, Preston Holloway, Jie Dong, and Prof. Zhenghe Xu in CME)

Recently, much attention has been paid to magnetic carriers, by conferring magnetic properties to a naturally non-magnetic target, such that the target can be separated from non-target entities using magnetic separators.[1] Magnetite nanoparticles are commonly used for this purpose because of their stability and intoxicity; superparamagnetism, i.e. low coercivity (H_c), high magnetic properties (big saturation magnetization, M_s), small size and narrow size distribution are also desirable for this purpose. In this project, a temperature-controlled synthesis was made in a teflon-lined stainless autoclave, with intent to study the temperature effects on the particle size and magnetization.

D.1 Experiments:

Magnetite nanoparticles were synthesized by coprecipitation in Prof. Xu's lab in Chemical and Materials Engineering, by the procedure below:

1. Dissolve $Fe_2(SO_4)_3 \cdot H_2O$ (4.25 g) + $FeSO_4 \cdot 7H_2O$ (2.5 g) into 75ml de-ionized (DI) water (stirred by ultrasound to be uniform).
2. Drop the mixture slowly into the Teflon-lined stainless autoclave.
3. Put 29.35 % NH_4OH into 100 ml DI water and stir to be uniform.
4. Continuously add NH_4OH solution to the mixture solutions until pH reached 10 under vigorous stirring to get black precipitate.
5. Heat the autoclave for 6 hours, kept at a certain temperature.
6. Collect the particles with a magnet and wash about 10 times with DI water.
7. Dry the particles in vacuum for further characterization.

In this experiment, the temperature is controllable in the coprecipitation process by heating the mixture encapsulated in the autoclave; four different temperatures (as listed in Table I) were used for the four samples, A, B, C, D, in order to study the temperature effects on the particle size, morphology and the magnetization.

The samples (powders of magnetite nanoparticles) were dispersed in DI water and then transferred to carbon-film-covered TEM grids for microstructural and phase analysis in a transmission electron microscope (TEM, JEOL 2010) in the Department of Physics. Magnetic measurements on the samples were also done in a PPMS vibrating sample magnetometer (VSM) in the Department of Chemistry, at room temperature. A certain amount of powder, 45 mg in this case, was used for the measurement.

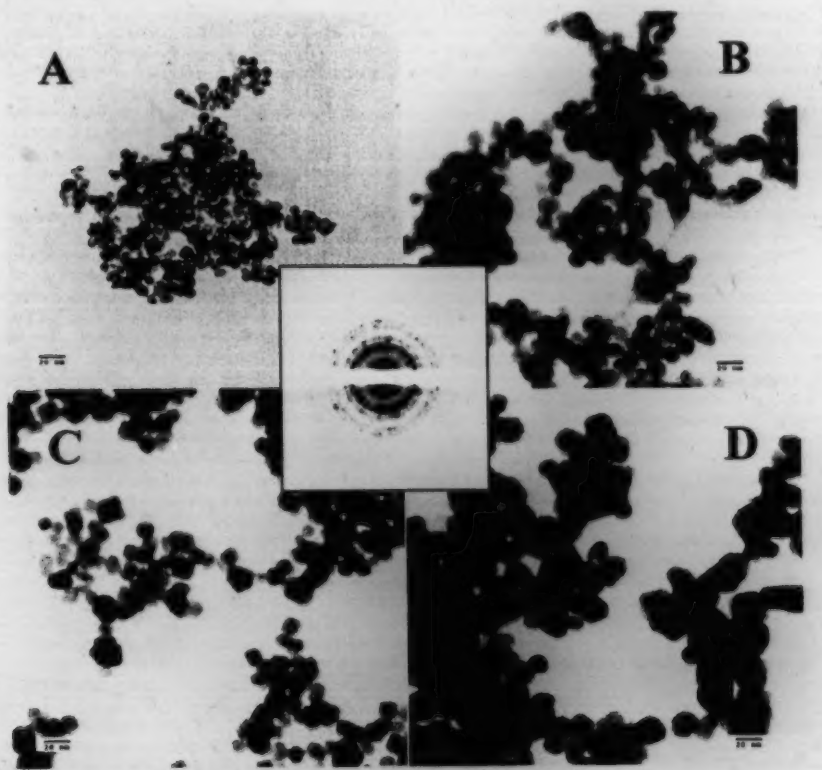

Figure D-1 Bring-field TEM images for four samples, synthesized at different temperatures and electron diffraction patterns (central inset)

D.2 Results

The morphology of the magnetitite nanoparticles synthesized at different temperatures is shown by bright-field TEM images in Figure D-1. The particles are spherical mostly, but can exhibit square or other shapes when particle diameter is bigger than a certain value, such as in sample C and D (giving the smallest free energy). The magnetite nanoparticles are seriously aggregated due to the strong magnetic interactions. Typical selected area

electron diffraction (SAED) pattern is shown in the inset of Fig. D-1; for the four samples, the well-defined rings can be assigned to randomly oriented, crystalline Fe_3O_4 particles. It is obvious that the particle size depends on the synthesis temperature. Individual diameters of the nanoparticles were measured from plan-view TEM images and the results of a size analysis of 100 to 200 particles; the standard deviations and mean nanoparticle diameters are listed in Table I.

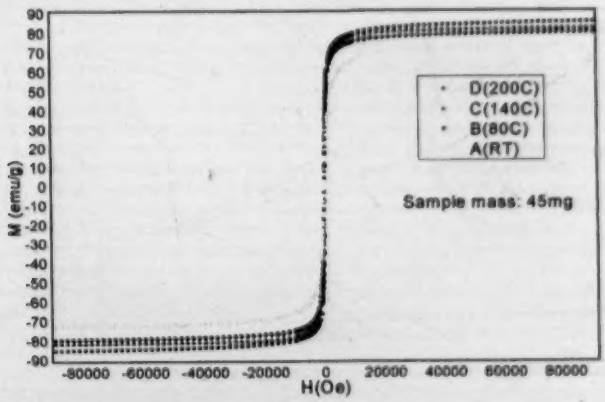

Figure D-2 Room-temperature magnetization of four magnetite samples, synthesized at different temperatures.

The measured room-temperature magnetization hysteresis of the four samples is shown in Figure D-2. Supermagnetism is shown for all the samples; small hysteresis loops were observed, because of the presence of bigger nanoparticles. The saturation magnetization (Ms) and critical magnetic field (Hc) measured from Fig.D-2 are listed in Table 1; magnetization changes greatly with the change of the synthesis temperature. For example, a saturation magnetization of 83 emu/g was obtained in sample D, much higher than that of sample A or reported values for magnetite nanoparticles that were synthesized at room temperature.

D.3 Remarks and conclusion

In this project, magnetite nanoparticles were successfully synthesized by coprecipitation in an autoclave at different temperatures; temperature affects the particle size and magnetization significantly. Synthesized nanoparticles in the autoclave have much bigger

saturation magnetization, due to their good crystallinity and large particle size when grown at elevated temperatures and pressures at the sealed autoclave.

The mechanical instability due to aggregation, because of the strong magnetic interaction, can be a big problem for the application in magnetic carriers; effective coating is required for the application of magnetic carriers, silica coating can be a solution. On the other hand, an LB (Langmuir-Blodgett) nanocomposite film, by capping magnetite nanoparticles with a certain organic material, is promising in magnetic applications.[2]

Table D-1 Synthesis temperature, particle size and magnetization for four different magnetite samples

Particles	*A*	*B*	*C*	*D*
Synthesis temp. (°C)	25	80	160	200
Average particle size (nm)	13±2	20±3	24±3	30±5
Ms (emu/g)	70	78	80	83
Hc (Gs)	20	70	80	200

References

[1] Q.A. Pankhurst, J. Connolly, S.K. Jones, and J. Dobson. Applications of magnetic nanoparticles in biomedicine. J. Phys. D: Appl. Phys, **36** (2003) R167–R181.

[2] Y, Lu, G.L. Liu, and L.P. Lee. Nano Lett. **5** (2005) 5-9.

Appendix E Exclusion of plural scattering

Regarding inelastic scattering as independent events, the probability of n-fold plural inelastic scattering of a transmission electron through a specimen follows Poisson's law

$$P_n = (1/n!)(t/\lambda_i)^n \exp(-t/\lambda_i) \qquad \text{(E-1)}$$

Here P_n represents the collision probability of the transmitted electron being scattered *n* times. The thickness dependent P_n, for cases of being scattering by zero time (P_0), once (P_1), twice (P_2) and three times (P_3) is given in Figure E-1. The thickness for the FeF_2 films used in this experiment $t = (0.10\pm0.01)\lambda_i$ (measured by EELS), This range of *t* is indicated by shadowing in Figure E-1.

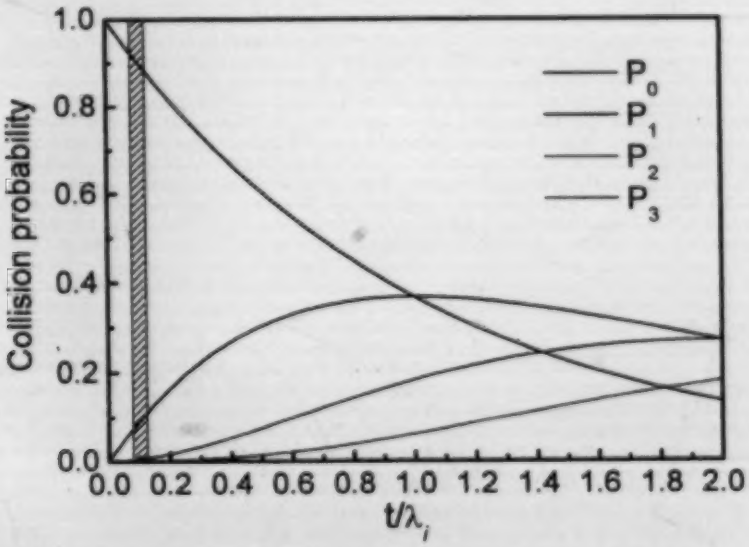

Figure E-1 Dependence of collision probability P_n (n=0, 1, 2, 3) on thickness parameter t/λ_i. The thickness for FeF_2 specimens is around t/λ_i =0.10, as labeled by the shadowed slice.

Figure E-2 shows a low loss spectrum for one of the FeF_2 specimens used in this experiment. Bulk plasmon is hardly seen in the low loss region, suggesting that most of transmission electrons are unscattered (See, P_0) and small part of the electrons are scattered once (see, P_1); the plural scattering is negligible.* We can safely conclude that the postpeak above the Fe-L edges (as shown in Figure 3-2) is accounted for by other mechanism than the plural scattering of the transmitted electrons.

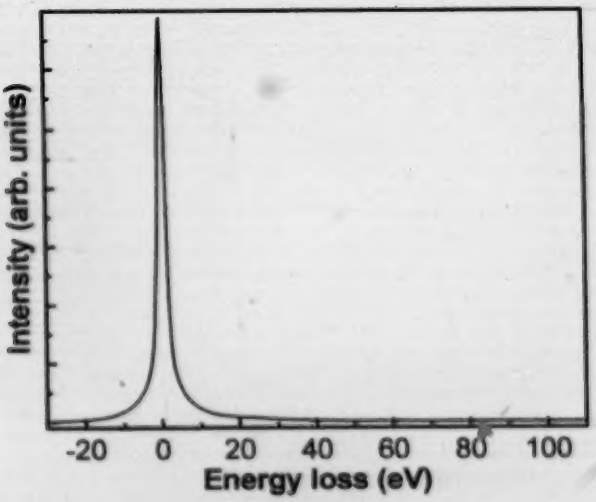

Figure E-2 Low loss spectrum for a FeF_2 film

Figure E_1 provides a guide in choosing TEM specimen thickness suitable for EELS experiments. In general t/λ_i = 0.1-0.3 is a convenient range of thickness, corresponding to 20-50 nm for a 200KV TEM and a medium atomic number sample.

* The probability for surface-mode scattering is so small (< 5%) for normal incidence.

Appendix F Terminology

Explanation of some of the terminologies used in the thesis is given below.

Atomic multiplet effects result from the coupling of the angular momentum of the core hole with that of any particular unfilled shells within the excited atom. The multiplet splitting is basically an atomic effect, but modified by *solid-state effects*, such as the chemical and crystallographic environment of the excited atom. For example, the tetrahedral or octahedral crystal structures are generally formed in transition metal oxides; the L_2 and L_3 peaks of transition metal oxides are each split into two components because of the nonspherical electrostatic field of the oxygen ions surrounding the transition-metal atom (also called the crystal-field splitting).*

Characteristic angle of inelastic scattering is defined by $\theta_E = E / \gamma m_o v^2 \approx E / 2E_o$, where γ is a relativity constant and v the velocity of the incident electron. It is typically a few mrad)

Chemical shift means the shift of the core-loss edge threshold by a few eV due to the charge transfer effects (arising from, i.e. chemical bonding). Chemical shift can be used to identify the valence state of the same element in different compounds.

Coster-Kronig transition is essentially an Auger process that happens between the subshells of a same atomic shell having the same principal quantum number, by which a hole created in one of the subshells shifts to higher subshells before the hole is filled by another transition.

Curved-wave theory When the energy of the photoelectron is sufficiently high (in EXAFS) the outgoing wavefunction can be accurately approximated by a plane wave (i.e.

* R.F. Egerton, Electron Energy-Loss Spectroscopy in the Electron Microscope, 2nd edition, Plenum Press, New York (1996) P237-238.

the curvature of the spherical wave of the photoelectron is neglected). For example, Sayers et al., used the plane wave approximation in getting a standard formula for EXAFS[†] (generally called the plane wave theory). The simplified expression for the EXAFS function is valid at high photoelectron energies and breaks down at lower energies (in XANES). Theory including the curvature feature of the photoelectron is generally called the curved-wave theory, and applied to near-edge region, i.e. XANES.

Density functional theory (DFT) The many-body electron-electron interactions are involved in calculating the electronic structure of solids. The electrons are undistinguishable particles due to the electron exchange and correlation. Put in a simple way, electrons are affected by the presence of other electrons and their behavior is correlated. Given the large number of electrons involved in the calculation, an effective approach employed is the density functional theory (DFT), which uses a simplified assumption called the local density approximation (LDA): approximating all the difficult parts of the potential due to the electron exchange and correlation, as a function of the local charge density. DFT is used in band structure calculations of ground state electronic structure.

Density of states (DOS) is essentially the number of electron states within unit energy increment. A *joint density of states* (JDOS) refers to a convolution of the energy dependence of the initial occupied with the final unoccupied density of states. If the initial state is a deep core state (i.e. ELNES), its energy width approximates to a delta function and the cross-section is proportional to the density of unoccupied states in the conduction band. But in the case of the valence electron energy-loss spectroscopy (VEELS), which measures the energy loss caused by the excitation of outer-shell (or valence) electrons to unoccupied states above the Fermi level, an electron state in an energy band (whether occupied or not) is intrinsic for the whole solid and can neither be attributed to a certain atomic species nor be localized within the solid. So it is primarily

[†] Sayers et al., Phys. Rev. Lett. 27 (1971) 1204.

information about the non-localized, joint density of states, i.e. the band structure of the materials that measured by VEELS.

Double-differential scattering cross-section The fraction of electrons undergoing inelastic scattering may be expressed in terms of a double differential cross-section $d^2\sigma / dEd\Omega$, giving the fraction of incident electrons scattered into the solid angle $d\Omega$ over an energy range dE. The differential cross-section is directly proportional to the intensity measured in EELS analysis in single-scattering case.

Electron gas theory Interacting electrons move in the constant electrostatic potential provided by a fixed positive "background charge" of the same charge density. This gives a simple picture in considering the electron-electron interactions (see, "Hedin-Lundqvist self-energy").

Energy-loss near-edge structure (ELNES) is an electron-beam counterpart of the x-ray absorption near-edge structures (XANES). Both measure the probability of the core-level excitations, as represented by the strong fluctuations within 50 eV of the core-loss edge threshold. The theoretical interpretation of *ELNES* generally follows two major approaches: the band structure model relating *ELNES* to an appropriate density of states, and multiple scattering theory (in an extension to the cluster calculations used in *EXAFS* analysis) describing ELENS as the interference of the outgoing waves of the excited electron with the returning waves reflecting off the surrounding atoms (and thus sometime called scattering resonance).

Extended energy-loss fine structures (EXELFS) is an electron-beam counterpart of the extended x-ray absorption fine structures (EXAFS). It refers to the weak oscillations extending to 50 eV-1000eV above the core-loss edge, and are readily accounted for by the backscattering of the nearest-neighbor atoms. EXFLFS (EXAFS) gives the quantitative information on the nearest neighbor distances and the co-ordination numbers (with an accuracy of $\pm$ 1)

Fermi level The highest occupied level in the outmost band is known as Fermi level E_F (strictly speaking this is only true at a temperature T= 0 K). The position of E_F within the bands conveniently differentiates between conducting and insulating solids. Conducting solids have an E_F that lies within an energy band; thus there are unoccupied states in the band available to receive electrons which are excited by thermal or electrical means. E_F in insulators and semiconductors lies between bands; thus the outmost valence band is full and is separated by a finite energy gap from the unoccupied conducting band.

Final state rule The many body effects (including the interaction of the photoelectron with the core-hole) and the inelastic losses (generally accounted for by an energy dependent self-energyΣE) are also considered in the codes using the independent electron approximation, such as in the RSMS calculations (as in FEFF codes). A good approximation in many cases is to calculate the final state in the presence of the core hole and the initial state with ground state potentials. This approximation is referred to as the final state rule.

Fingerprinting technique is one of the main approaches to understand the near-edge structures (ELNES), to collect "fingerprints" from elements in similar chemical environments of the element of interest, and try to identify common features. More information can be extracted from ELNES by theoretical calculations, such as multiple scattering calculations. The two methods are both valuable and readily complement each other.

Hedin-Lundqvist self-energy Real-space multiple scattering (RSMS) calculation is an excited-state electronic structure calculation based on the final-state rule, in which the final states are calculated in the presence of an appropriately screened core-hole and inelastic losses are represented by using a complex energy-dependent "self-energy" ΣE. The real part of ΣE leads to the shift of edge threshold, and the imaginary part leads to the broadening of the spectrum ($\lambda(E) \sim k/(|Im\Sigma E| + \Gamma/2)$, where Γ is the inverse of core-hole lifetime). Hedin-Lundqvist self-energy is based on uniform *electron-gas theory* and was firstly introduced into the x-ray absorption theory by Lee and Beni. Based on the

approximation, a complex potential is constructed to account for the exchange and correlation effects of electrons in atoms, and added to the electrostatic potential to calculate the complex phase shifts of the photoelectron. This approximation is also used in FEFF calculations (and also other XAFS codes) for solids.

Mean free path (MFP) Mean free path for inelastic scattering (λ_i) represents the average distance that a beam electron will travel inside the sample between scattering events. λ_i is a function of the beam energy and of the specimen. In understanding the MFP for excited electrons, an electron with a small kinetic energy has a long λ_i since it can only excite phonons and can therefore undergo many inelastic scattering process before it loses all the excessive energy. By contrast, an excited electron with a large kinetic energy has short λ_i since it can excite plasmons and other high loss excitations and may only have time for one elastic scattering process before loses its energy in an inelastic scattering. So the EXAFS comes mainly from backscattering of the nearest neighboring atoms, while XANES (ELNES) are attributed to multiple scattering of distant atoms.

Muffin tin potential is an approximation in that a spherical scattering potential is centered on each atom and a constant value in the interstitial region between atoms. Almost all practical x-ray absorption spectrum calculations use this approximation. This approximation is not good for calculating near-edge structure, where the effects of a non-flat interstice and of neglecting charge transfer can be most apparent. The non-flat interstice can be quite important for highly anisotropic materials with strongly directional covalence (that's why multiple scattering is not accurate in calculating this kind of materials at near edge range). The effect of using neutral spheres to construct the muffin tin can be corrected by *self-consistent field* (SCF) calculation. Band-structure calculations (i.e.Wien2K codes) are based on the muffin-tin approximation, but the full shape of the true electronic charge density and potential throughout space is used (and thus called the full-potential method); so that the calculation of XANES is very accurate for highly covalent materials with open structures.

Multiple scattering (MS) is used in discussing the x-ray absorption near-edge structures (XANES) or electron energy-loss near-edge structure (ELNES). This is an extension of the extended x-ray absorption fine structures (EXAFS) theory, by including the multiple scattering of the excited electrons by the surrounding atoms (which is in nanometer range).

One-electron (or independent electron) approximation In this approximation, the other electrons in the atoms are assumed not to be affected by the excitation of one electron in inner-shell. This is the starting point for the interpretation of *ELNES*, both in band structure and *multiple scattering* approaches.

Plural scattering The events that the transmitted electron is inelastically scattered by more than once in a thick specimen is called the *plural scattering*, which is present in the spectrum as both multiple plasmon losses and additional intensity superimposed onto the near-edge structures of the ionization edges (sometimes called post-edge peak). The effect can be removed by deconvolution.

Scattering cross-section (σ) represents the probability of an interaction with each atom, defined as $\sigma = n_s / n_t n_i$, where n_s is the number of scattering events per unit area, n_t is the number of target atoms per unit area and n_i is the number of incident electrons per unit area.

Self-consistent-field (SCF) In a general sense, self-consistent field (SCF) is a method to run iterated calculation on certain correlated quantities until self-consistency is achieved. The FEFF8 program (used in this study) implements a card to calculate the self-consistent potential: starting with the electronic configuration of free atoms at the positions specified in the input file, the electronic potential is calculated using a muffin tin potential modle; the potential, electron densities and the Fermi energy are iterated until they are self-consistent. It is through the self-consistency loop that the charge is redistributed between atoms and among the angular momentum states of each atom.

Solid-state effects The core-loss spectrum for isolated atoms is smooth in the near-edge region except for sharp peaks arising from the Rydberg states.‡ However, the fluctuations arising from solid-sate effects that are superimposed on the basic edge shape cannot be simply accounted for by transitions to the unfilled states of isolated atoms. The additional fine structures (ELNES) originate from the modification of the *density of states (DOS)* of the target atom by interaction with surrounding atoms, and are thus strongly dependent of the bonding, co-ordinations.

Standard deviation The standard deviation shows the possible spread of the individual measurements from the mean value $\bar{x}$, and defined as

$$\sigma = \sqrt{\frac{1}{n-1}\sum_{i=1}^{n}(x_i - \bar{x})^2}$$

Superlattice reflection is present because the material (especially for alloys) is ordered such that the actual real-space unit cell is larger and thus the reciprocal space cell is smaller. Often the structure factor associated with these reflections is proportional to the difference of two atomic scattering factors of binary compounds; therefore the reflection is chemically sensitive. The superlattice reflection is not present in the disordered or partially ordered materials, such as the surface layer of iron nanoparticles (in Chapter 4).

White lines are sharp peaks found near the edge threshold of the transition metals originating from excitations of 2p to vacant narrow 3d orbital. These sharp peaks are known as white lines since they were first observed in x-ray absorption spectra where the high absorption peak results in almost no blackening on a photographic plate. White lines come mainly from atomic effects and its value varies with atomic number. The *white line ratio* (WLR) measures the occupancy of the 3d states, and thus can be used to evaluate the valence state of 3d transition metals.

‡ See, the review in Keast et al., J. Microsc. 203 (2001) 135.